nagra.

Arbeitsbericht NAB 23-12

Diffusion and Retention of Moderately and Strongly Sorbing Tracers in Compacted Illite

July 2023

M. A. Glaus, S. Frick, L. R. Van Loon

National Cooperative
for the Disposal of
Radioactive Waste

Hardstrasse 73
P.O. Box
5430 Wettingen
Switzerland
Tel. +41 56 437 11 11

www.nagra.ch

nagra.

Arbeitsbericht NAB 23-12

Diffusion and Retention of Moderately and Strongly Sorbing Tracers in Compacted Illite

July 2023

M. A. Glaus[1], S. Frick[2], L. R. Van Loon[1]

[1] PSI
[2] Kanton Aargau, Departement für Gesundheit und Soziales

KEYWORDS

Illite, strongly sorbing tracer, radionuclides, diffusion coefficient, ion competition, clays, diffusion database, sorption competition

National Cooperative
for the Disposal of
Radioactive Waste

Hardstrasse 73
P.O. Box
5430 Wettingen
Switzerland
Tel. +41 56 437 11 11

www.nagra.ch

Nagra Arbeitsberichte ("Working Reports") present the results of work in progress that have not necessarily been subject to a comprehensive review. They are intended to provide rapid dissemination of current information.
This report was prepared on behalf of Nagra. The viewpoints presented and conclusions reached are those of the author(s) and do not necessarily represent those of Nagra.

Abstract

The prediction of effective diffusion coefficients adequate for given pore water and clay surface properties, involves on the one hand knowledge of the prevailing geometry factors and on the other hand, knowledge on the speciation of the radioelement in the aqueous phase and at the clay surface, in particular the amounts of mobile surface species.

This report provides a number of experimental investigations in which the validity of the calculated speciation for the prediction of the diffusive properties of the radioelements selected is tested. In addition to parameters already tested in other studies, such as the ionic strength and pH, the present report focuses on various types of competitive actions for diffusion. The competition between $^{57}Co^{2+}$, ^{55}Fe, $^{54}Mn^{2+}$ and $^{152}Eu^{3+}$ tracers and Ca^{2+} or Mn^{2+}, respectively, is investigated under a broad variety of conditions. It is shown that the effective diffusion coefficients of these radiotracers decrease with increasing concentrations of the competing cations. This can be explained by competition of the cations in the electrical double layer at the basal surfaces, which leads to a decrease of the concentrations of mobile radionuclide species and thus to a decrease of the effective diffusion coefficients. The sorption distribution ratios are influenced in an expected manner, corroborating thus the experience that the sorption properties measured in disperse systems are well applicable also in the compacted state of the illite.

The present findings are fully compatible with our current understanding of sorption competition effects and the knowledge on the different site preferences of different types of cations. The prediction of effective and apparent diffusion coefficients in the compilation of diffusion databases for site specific conditions of rock pore water will be broadly supported by the present data.

Table of Contents

List of Tables

List of Figures

1 Introduction

1.1 Scope and aim of the report

The prediction of the migration of radionuclides in the near- and farfield of a deep geological repository of spent fuel and radioactive waste under water-saturated conditions requires a sound understanding of the diffusion processes and the use of robust parameter values for the involved effective diffusion coefficients and sorption distribution coefficients. The definition of the former quantities as the proportionality factor between the mass flux and the concentration gradient of species in the aqueous phase as the driving force for diffusion (other types of driving forces, such as thermal or electric potential gradients, are omitted from the following discussion) leads to intricate functional dependencies of these parameters on various chemical properties of the solution and the surface of the involved porous medium. This applies particularly to the migration of radionuclides in argillaceous porous media, be it in compacted bentonite or clay-rich host rocks, because these materials bear negative lattice charges enabling cation exchange and anion exclusion processes.

In the case of cation exchange, it has been demonstrated in various ways that at least part of the exchange species at the basal clay surfaces exhibit surface diffusion properties and that their surface concentration gradients act as a driving force for diffusion in addition to the concentration gradients in the aqueous phase. A parallel two-flux description involving aqueous phase species and mobile surface-associated species would represent an adequate modelling approach for such a situation. However, if the driving force for diffusion is limited solely by the concentration gradients in the aqueous phase, the influence of mobile surface-associated species will be noticeable by "unexpected" functional dependencies of the effective diffusion coefficients on chemical properties of the aqueous phase or the solid, provided that these parameters have an influence on the species distribution of the mobile surface-associated species. A recent in-depth discussion of such effects can be found in Maes et al. (2021).

In the case of anions, a single-phase diffusion model is applicable for such situations. However, owing to the presence of fixed negative lattice charges in the clay matrix, the concentration gradients of anions in the aqueous phase are directly altered compared to the respective concentrations in bulk water by the presence of these surface charges.

The following report focuses on the diffusive behaviour of trace cation species in compacted illite which is an important argillaceous constituent of natural clay rocks. We demonstrated in previous studies that the model assumption of mobile cationic surface species in the diffuse layer of an electrostatic double layer at the basal surfaces could explain different parameter dependencies of the effective diffusion coefficients of various types of radionuclides on various solution parameters, such as the ionic strength or pH (Glaus et al. 2015a, Glaus et al. 2020, 2021). The so called two-site protolysis non-electrostatic surface complexation and electrical double layer (2SPNE SC/EDL) model was successfully applied to describe the sorption and diffusion properties of a broad variety of cationic species (Glaus et al. 2015a, Glaus et al. 2020, 2021). Similarly, the volume-averaged Donnan approach for the concentration depletion of anionic species in the pore space of porous argillaceous media was also used to explain the diffusion behaviour of negatively charged species (Appelo & Wersin 2007, Birgersson & Karnland 2009, Gimmi & Alt-Epping 2018, Leroy et al. 2006, Wigger et al. 2018). The present approach is thus able to simultaneously explain the diffusion behaviour of positively and negatively charged species, a model feature which is available for only restricted types of diffusion models (e.g. Lehikoinen et al. 1999).

The present report summarises further types of parameter variations with attention focused on the influence of the chemical composition of the aqueous phase in terms of competing cationic species. An appropriate consideration of such influencing factors is important for the bottom-up

type derivation of effective diffusion coefficients in natural clay rocks based on the respective diffusion properties in pure compacted illite systems. The robustness of such predictions has recently been demonstrated for the competitive effects of Ca^{2+} on the diffusion and sorption properties of trace $^{57}Co^{2+}$ (Glaus et al. 2021). While the parametrisation of the pure illite system was restricted to pH 5 and a single ionic strength (0.1 M NaCl), the ranges of parameter variations were extended in the present work. Furthermore, a case example is presented here in which the competition between a representative of the transition metal series (Mn^{2+}) on the diffusion and sorption properties of $^{57}Co^{2+}$ tracer has been investigated. Note that diffusion measurements involving sorbing species inherently provide information on the sorption properties of these test species at high solid-to-liquid ratios. These measurements are thus complementary to sorption measurements performed in dispersed suspensions at low solid-to-liquid ratios ("batch mode") which is the common experimental approach for obtaining such values. The comparison of the present results with existing sorption models based on measurements in the batch mode can thus be considered as a side product of the present investigations.

The diffusion and sorption properties of Mn^{2+} in illite are of particular interest because this cation is frequently used as an analogue for ferrous iron (Fe^{2+}) which is more difficult to handle experimentally because of its tendency to undergo redox reactions not only with external electron acceptors or donors, but also with structural species of the clay lattice (Baeyens & Fernandes 2018). Mn^{2+} has a slightly higher pK_a than Fe^{2+} (Baes & Mesmer 1976), from which it can be expected that its sorption behaviour is somewhat weaker than that of Fe^{2+}. Otherwise, no fundamental differences between these two metal cations are expected regarding the diffusion in and sorption on compacted illite. As a basis for the understanding the competition between Mn^{2+} and $^{57}Co^{2+}$, the sorption and diffusion properties of $^{54}Mn^{2+}$ tracer was investigated as a broad variety of solution parameters, viz. pH ionic strength and the presence of stable isotope Mn^{2+}. It is shown here how a valuable sorption model can be derived solely based on diffusion measurements using compacted samples of a clay mineral.

Further, as rather isolated topics, results are presented for (i) diffusion measurements with $^{57}Co^{2+}$ in compacted illite at a bulk dry density of ~ 2'200 kg m^{-3} and (ii) for assessing the influence of an organic ligand on the diffusion properties of $^{152}Eu^{3+}$. The former measurements can be seen as a bridge between most of the diffusion tests in the present and in previous work which were carried out at lower bulk dry density (1'700 kg m^{-3}) for reasons of practicability and the potential extent of clay compaction in natural clay rock (> 2'100 kg m^{-3}). The purpose of the latter experiment is of rather academic value, namely to identify previously unknown parameter dependencies related to the presence of organic ligands in the aqueous phase. Both experiments, however, serve the general purpose of the present report which lies in a broad experimental support of the validity of deriving diffusion data for complex natural clay media based on measurements of single-mineral systems.

1.2 Summary of the 2SPNE SC/EDL model

The 2SPNE SC/EDL model (Glaus et al. 2015a, Glaus et al. 2020) is an extension of the two-site protolysis non electrostatic surface complexation and cation exchange (2SPNE SC/CE) model originally introduced for smectites (Bradbury & Baeyens 1997) and later also applied for illite (Bradbury & Baeyens, 2009a, 2009b, Marques Fernandes et al. 2015). The cation exchange reaction at the planar surfaces is extended in the former model to the formation of (i) surface complexes in the so-called Stern-layer along with (ii) the formation of an electrostatically attracted diffuse swarm of cations in the so-called diffuse layer. Both models assume the same type of surface complex formation at the edge surfaces, viz. those formed from the weak and strong sites. The extension "EDL" refers to the uptake processes near the basal surfaces where an electrical double layer is assumed to form from surface species in the Stern layer and species in the diffuse layer (Maes et al. 2021). Note that this arrangement is also denoted as a triple layer in

the literature, depending on whether the fixed negative lattice charges are also considered as a charged layer (Tournassat et al. 2009). For the implementation of the 2SPNE SC/EDL model, a Donnan approximation involving a constant potential until a given distance from the planar surfaces (the "Donnan thickness") with a drop to zero-potential for the adjacent free pore water is taken. The pore space is thus subdivided into a Donnan volume and a volume containing free pore water. Compared to the electrolyte concentrations in the free pore water, cations are enriched and anions depleted in the Donnan volume for the purpose of the neutralisation of surface charges. Furthermore it is assumed that the concentrations of cations and anions i in the Donnan volume ($c_{i,DL}$) are in equilibrium with the respective concentrations in free pore water (c_i) according to the Boltzmann condition (Appelo & Wersin 2007):

$$c_{i,DL} = c_i \exp\left(\frac{-z_i F \Psi_D}{RT}\right) \tag{1}$$

where z_i denotes the charge number of species i, F the Faraday constant, Ψ_D the Donnan potential, R the universal gas constant and T the temperature.

The model extension of the 2SPNE SC/EDL comprises the assumption that the species in the diffuse layer are mobile despite their chemical state of 'sorbed' species. This leads to the situation in which the overall diffusive flux of species is a superposition of the flux of species in the free pore water and in the diffuse layer. The superposition can be treated as additive provided that the chemical equilibration between solution and surface occurs much faster than diffusion (Glaus et al. 2021). Under such conditions the effective diffusion coefficient in the clay ($D_{e,c}$) can be expressed for a given species i as:

$$D_{e,c} = \frac{\varepsilon}{G}\left(f_{free} + f_{DL}\frac{c_{DL}}{c} q_\eta\right) D_w \tag{2}$$

ε [–] is the total water accessible porosity, G [–] the geometry factor, f_{free} [–] the porosity fraction containing free pore water, f_{DL} [–] the fraction of Donnan layer porosity, D_w [m^2 s^{-1}] the diffusion coefficient in bulk water and q_η [–] the viscosity factor. The latter factor reflects changes in the surface mobility compared to the mobility in the bulk pore aqueous phase. Note that the concentration ratio c_{DL}/c can readily be converted to an "R_d value of mobile surface species". Such an R_d value should, however, not be confused with the common R_d value used in sorption models, because the latter comprises the sum of all sorbed species including those at the edge sites, whereas the former only comprises the mobile surface-associated species. According to the enrichment/depletion behaviour the model can predict the characteristic transport behaviour of both cationic and anionic species in negatively charged clay minerals (Glaus et al. 2020).

The application of expressions like eq. (2) in a Comsol Multiphysics single-species transport model is limited to situations in which the parameters are independent of concentration c. This can be assumed to be fulfilled for example in experiments in which the external solutions in contact with the clay and the clay pore water are in an equilibrated state. Under such conditions the $D_{e,c}$ and R_d values are independent of concentration. However, there are situations in which a radioactive tracer is provided from a solution reservoir to the clay sample along with a background concentration of its stable-isotope. Depending on the diffusion depth, the test element will thus be present at different concentrations. Under such conditions R_d values (and potentially also $D_{e,c}$ values) are expected to be concentration dependent. In such cases derivative expressions of $D_{e,c}$ and R_d values need to be used in the transport equation for diffusion.

The implementation of the 2SPNE SC/EDL model is normally based on the assumption of a cylindrical pore geometry (cf. Fig. 1-1).

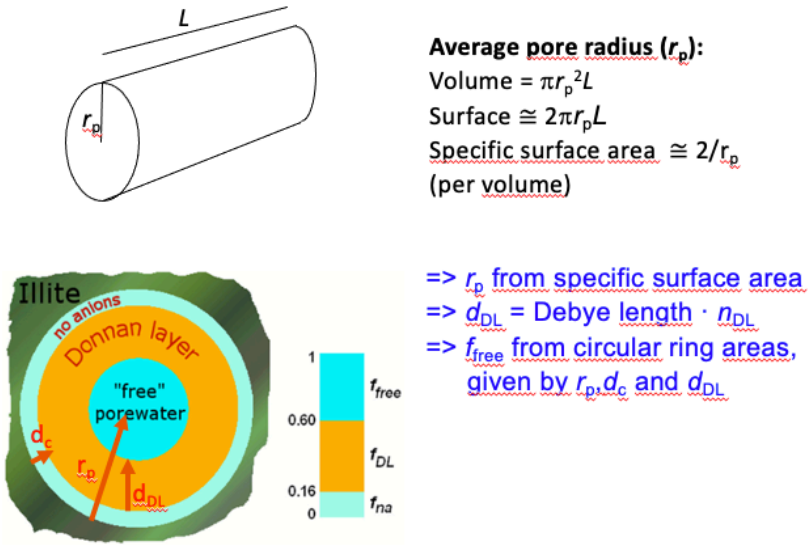

Fig. 1-1: Schematic representation of the cylindrical pore model
Glaus et al. (2015a)

There is actually no clear preference of the cylindrical pore geometry over a planar pore geometry. A few data for anion-accessible porosity in compacted illite were demonstrated to be in better agreement with a cylindrical than with a planar pore geometry (Appelo 2013). However, the uncertainty of these data did not allow for an unambiguous discrimination of these assumptions. As can be taken from Fig. 1-1, the basic input quantities for defining the subdivision of the pore space into the different domains are the specific surface area and the Donnan thickness (d_{DL}). From the specific surface, an approximate[1] pore radius can be calculated, which – in combination with d_{DL} – yields the volume fractions of free and Donnan pore water. A potential refinement of such a model is possible by introducing a volume fraction inaccessible for anions representing approximately the extension of the Stern layer. This volume fraction is commonly defined via its thickness (d_c). The subdivision of the individual pore domains may then occur via the assumptions taken for d_{DL} and d_c. d_{DL} is commonly assumed to be a multiple (n_{DL}) of the Debye length (d_{DL}) which depends on the ionic strength. The assumption of $n_{DL} = 2$ is taken as a workable hypothesis (Parkhurst & Appelo 1999). Ψ_D is iteratively calculated from the composition of the chemical system in order to obtain an optimal agreement for the conditions of charge neutrality and compliance with the Boltzmann equilibrium condition (cf. eq. (1)). A critical input quantity for these calculations is the value of the net surface potential which depends on the fraction of surface charges neutralised directly by the Stern layer complexes. The equilibrium constant for the formation of the Stern layer surface complex of the main cation of the electrolyte is therefore a further important input quantity for these calculations. In the literature, only the equilibrium constant for the formation of Na^+ Stern layer complexes is directly known. It has been determined based on indirect evidence for Opalinus Clay rock (Appelo et al. 2010). The value ($\log k = -0.7$) has been found to be in good agreement with the exclusion behaviour of homo-ionic sodium illite (Appelo 2013). For other cations, the respective anion exclusion behaviour of other homo-ionic illites would principally be an option for the direct measurement of these constants. They may also be derived from the pertinent selectivity coefficients for cation exchange reactions of the homo-ionic sodium illite. The respective definitions and procedures have been described in Glaus et al. (2020) and Glaus et al. (2021). Briefly, the equilibrium constants for the formation of the

[1] Neglecting the contribution of the cylindrical front surfaces to the total surface.

surface complexes in the Stern layer are adjusted in a manner that the overall occupancy of the planar surfaces by the cationic species in the Stern layer and the diffuse layer optimally reflect the fractional occupancy of the respective cation in a pure cation exchange model. It should, however, be noted that the internal consistency between the anion exclusion behaviour of a homo-ionic illite and its respective cation exchange behaviour have not been demonstrated experimentally so far. Finally, q_η is also a fitting parameter in this model.

From this brief outline of the model, it can be taken that a broad variety of model parameters may be adjusted in order to obtain good data fits. The diffusive behaviour of cationic species may also be described using a simpler model approach involving mobile cation exchange species at the planar surfaces (Krejci et al. 2021), for example. Such a model has less adjustable parameters because it does not subdivide the pore space into different water domains. From the fundamental requirement of using a minimum of adjustable parameters, the 2SPNE SC/EDL model is considered as a valuable tool only provided that a single set of geometric model parameters would describe the sorption and transport behaviour of a broad variety of radionuclides under broad ranges of chemical conditions. This has been so far demonstrated by experiment in many cases (Glaus et al. 2015a, Glaus et al. 2020, 2021). The present report will further extend the scope of test systems. If the model validity of the 2SPNE SC/EDL model is equivalent to the cation exchange model, its disadvantage of more adjustable parameters will be counterbalanced by the advantage that it may also describe the uptake and transport behaviour of anionic species within the same model scope. The equivalence of both model approaches has so far been confirmed for Cs^+ (Glaus et al. 2020) and Co^{2+} (Glaus et al. 2021).

1.3 Diffusion data available from literature

Diffusion data of strongly sorbing charged species in compacted illite are scarce. Much more information is available for uncharged, negatively charged or weakly sorbing species.

The diffusion behaviour of uncharged tracers like tritiated water (HTO) were shown (Glaus et al. 2010) to depend on porosity, according to an Archie's type of law:

$$D_{e,c} = A\,\varepsilon^m \tag{3}$$

A and m are empiric parameters which depend on material specific geometric pore characteristics like the connectivity of pores or pore width. The value found for A (1.35×10^{-9} m^2 s^{-1}, Glaus et al. 2010) is rather close to the bulk diffusion coefficient (D_w) of 2.3×10^{-9} m^2 s^{-1} (Li & Gregory 1974). This indicates that the diffusion in the pore space of compacted illite is close to the diffusion in bulk water, which is in contrast to the respective behaviour in compacted smectite, for which the value of A was significantly smaller (Bestel et al. 2018).

The work of Glaus et al. (2010) also demonstrated that the order of $D_{e,c}$ values decreased in the series of $^{22}Na^+ > HTO > {}^{36}Cl^-$, which is in agreement with the conceptual explanation that cations are enriched near the negatively charged planar surfaces and anions are depleted therefrom (cf. Fig. 1-1). Similar observations were also made for the diffusion of Cs^+ (Glaus et al. 2020, Ishidera et al. 2016). It was further demonstrated that the surface diffusion effects were not only restricted to cations predominantly undergoing cation exchange at the planar surfaces (Aertsens et al. 2017), but also to representatives of the transition elements and lanthanides (Glaus et al. 2015a, Glaus et al. 2020, Montoya et al. 2018), which additionally form strong surface complexes at the edge surfaces. It was also demonstrated that the diffusion rates of anionic species may decrease below the limits of detection in situations in which the pore space gets filled with sparingly soluble mineral compounds, such as $SrSO_4$ (Chagneau et al. 2015, Fukatsu et al. 2016), while the diffusion of neutral species was still measurable. It was concluded from these observations that pore spaces exist in compacted illite in which anions are almost excluded.

2 Materials and methods

The present section contains generic information about experimental and numerical procedures. More detailed information is given in the subsequent sections where necessary.

2.1 Source materials

High purity reagents were obtained from Sigma Aldrich (Buchs, Switzerland) and Merck (Dietikon, Switzerland). Ultrapure water (Milli-Q® water) was used throughout for the preparation of aqueous solutions. The $^{54}Mn^{2+}$ tracer was obtained from Perkin Elmer (Boston, MA, USA). The specific activity was between 21 and 11 GBq per gram of total Mn at the time of the experiments. The dilute tracer stock solution contained 1.25 mM HCl. The $^{57}Co^{2+}$ tracer was obtained from the same source, but carrier-free. It was diluted in 0.15 mM HCl. The $^{152}Eu^{3+}$ tracer was obtained from Eckert & Ziegler and contained ~ 670 GBq per gram of total Eu at the time of the experiments. It was diluted in 10 mM HCl. Radiochemical assays of these radionuclides were carried out with a γ-counter (Minaxi-c, Autogamma 5000 series, Canberra-Packard), with the exception of ^{55}Fe which was analysed by liquid scintillation counting.

High-performance cation exchange chromatography (HPCEC) measurements were done using a Dionex DX-600 or ICS-5000$^+$ system (Dionex, Switzerland) equipped with a 2 or 4 mm × 50 mm Ionpac CG-12A guard column and a 2 or 4 mm × 250 mm Ionpac CS12A analytical column and operated with an 18 mM methanesulfonic acid eluent at a flow rate of 1 cm^3 min^{-1}. Analyte quantification was performed using conductivity detection after electrochemical suppression of the eluent ions in the autosuppression mode.

The preparation of a Na-exchanged and weakly acid-washed illite (originating from Le Puy, France, further denoted to as IdP) has been described elsewhere (Glaus et al. 2015a). This procedure was extended by a rigorous washing of the clay with a formic acid buffer at pH 3.5 during the conditioning with 1 M NaCl until no significant amounts of Ca^{2+} and phosphate could be extracted. The clay materials were conditioned before use in the diffusion experiments in a dilute aqueous suspension to the desired pH using dilute HCl or NaOH, respectively, in order to avoid pH gradients during the diffusion experiments. After this conditioning step, the clay samples were freeze-dried for further preparation of compacted diffusion test samples. For dedicated cases, the clay was also converted to mixed metal forms in order to be equilibrated with electrolyte solutions containing different types of cations.

2.2 Diffusion experiments

Diffusion experiments were carried out at a temperature of 22 ± 2 °C in a nitrogen filled glove box ($p_{O2} < 0.1$ ppm) mostly for the purpose of keeping solutions free of CO_2. So-called membrane-confined diffusion cells (MCDC) were used (Glaus et al. 2015a) which are entirely made from polyether ether ketone (PEEK) avoiding any components made from steel. The conditioned clay samples were compacted to a target bulk-dry density of 1'700 kg m^{-3}. The dimensions of the cylindrical clay samples were 0.51 cm in diameter and ~ 1 cm in length. Two layers of PVDF membrane (Durapore®, Merck Millipore, 125 µm thickness) were used to separate the compacted clay sample from the contacting electrolyte solution. The samples were conditioned with the appropriate electrolyte solution for ~ 4 weeks before starting the diffusion. In-diffusion was started by addition of an appropriate amount of tracer stock solution along with an equivalent of NaOH to neutralise the HCl contained in the dilute tracer solution. Otherwise, the procedures to carry out the in-diffusion experiment and slicing the clay sample into segments after in-diffusion were identical to those described in Glaus et al. (2020). After in-diffusion, the clay plugs were cut into small segments with thicknesses between 0.1 and 1.0 mm using a razor

blade. Normally these segments were suspended in dilute acid (e.g. 0.1 M HCl) for the measurement of γ-activities in the samples. The purpose of acid addition was to extract the tracer from the clay and distribute it homogeneously in solution for obtaining a defined geometry for the γ-measurement. In single cases the clay segments were treated with appropriate amounts of Cs^+ in order to extract the exchangeable cations from the clay. In all cases, the individual parts of the diffusion cells and the containers used for in-diffusion were finally extracted with dilute acid in order to retrieve tracer amounts from these parts and to achieve a complete mass balance for the radiotracers, demonstrating whether the tracer loss from solution was satisfyingly compensated by the amounts retrieved from the clay samples.

In the subsequent representations of diffusion data, the specified concentrations refer to the concentrations of the sum of all isotopes (stable and radioactive) unless a specific mass number of the isotope has been indicated. In such cases, a carrier-free isotope preparation has been used and no stable isotope has been added. Note that the stock solutions of some radioisotopes already contain a background of stable isotopes. In a couple of experiments, stable isotopes were extra added in order to achieve a desired total isotope concentration. The total isotope concentrations in unknown samples were calculated by multiplication of the measured activities of the radioactive isotope with proportionality factors based on the known ratio between the stable isotopes and the radioactive isotope in the initial preparation of the solution. Further, the charge numbers shown indicate the sum of aqueous species in the solution phase. As an example, Mn^{2+} denotes in this context the sum concentration of bivalent manganese isotopes (radioactive ^{54}Mn, stable isotope ^{55}Mn) including the aquaion Mn^{2+} plus all other inorganic species, like hydroxo- or chloro complexes. The acronym $^{57}Co^{2+}$, on the contrary, represents the concentrations of all aqueous species of the ^{57}Co radioisotope and indicates that a carrier-free isotope preparation was used.

2.3 Simulation of the experimental data of the diffusion experiments

Numerical transport simulations were both carried out according to the methods described in Glaus et al. (2020) using a two-dimensional (2D) axisymmetric single-species diffusion model involving linear or non-linear sorption nodes in Comsol Multiphysics® or using the transport capabilities of Phreeqc (Parkhurst & Appelo 2013), whereby the geometry was reduced to 1D for simplicity. The built-in database phreeqc.dat was basically used for the latter purpose. Changes from this database are documented in the following or in the Appendix (Tab. A-1 and A-2). The Davies equation was used for the calculation of activity coefficients (Davies 1962).

Briefly, both numerical approaches are not ideally matching the particular circumstances encountered in the experiments. While the Phreeqc simulations appropriately represent the electrostatically controlled equilibrium distribution of cations at the negatively charged surface and potential surface mobility of species sorbed at the planar surfaces, the simulations do not fully take into account the different radial extensions of the membrane and clay because of its reduction to the 1D geometry. The Comsol model, on the other hand, does not take into account the chemical speciation of the EDL model, it simply uses effective diffusion coefficients representing the resulting flux based on the concentration gradients of aqueous phase species, only. The information from chemical speciation can, however, be implemented in the Comsol model using sorption isotherms and the pertinent concentration dependence of effective diffusion coefficients of the clay sample ($D_{e,c}$), such as the one used in eq. (2) (Glaus et al. 2015a, 2020).

All simulations were carried out using the assumption of a homogeneous distribution of clay mass across the clay plug. The gravimetric measurement of water loss in the individual clay segments obtained upon profiling the samples indicated the presence of inhomogeneities exhibiting slightly lower bulk-dry densities in the direction of the contact surface with the solution. However, owing to the very low masses involved in these measurements (only a few milligrams), it could not

unambiguously be decided whether this was an artefact or a real phenomenon. Similarly, the shape of the slightly bulbed clay specimen at the interface between clay and solution (related to the swelling pressure of the illite sample, which was not perfectly resisted by the membrane) was not taken into account in the geometry of the numerical models. Instead, a perfectly planar interface was used for simplicity.

2.3.1 Single species modelling using Comsol Multiphysics®

Optimum parameter values of $D_{e,c}$ and R_d can readily be derived by simultaneously fitting the source reservoir depletion curves and the tracer concentration profiles in the clay samples obtained after in-diffusion using a 2-dimensional axisymmetric Comsol Multiphysics (Versions 5.2 to 5.6) single-species diffusion model (Glaus et al. 2015a). Note that the impact of these parameters on the two data sets are anti-correlated: While the extent of tracer depletion increases both with increasing values of $D_{e,c}$ and R_d, the profile depth only increases with increasing $D_{e,c}$, whereas it decreases with increasing R_d. This situation allows for an unambiguous determination of the fitting parameters in many situations. However, the exact boundary concentration conditions at the interface between the confining membrane and the clay sample are uncertain to some extent, because the effective diffusive coefficients of the confining membrane ($D_{e,f}$) are not exactly known. Although respective measurements of representative tracers, such as tritiated water, are available, it has to be assumed that such $D_{e,f}$ values are biased owing to the swelling and concomitant deformation of the membrane in the in-situ situation of the diffusion experiment. The bias can be assessed from the initial phase of the source reservoir depletion curve, and $D_{e,f}$ values for the in-situ situation of the diffusion experiment are accordingly assessed for each diffusion experiment individually by treating this parameter as a fitting parameter, too (Glaus et al. 2015a, 2015b).

For tracer diffusion experiments, $D_{e,c}$ and R_d can normally be treated as constants. Sorption is formally implemented in Comsol Multiphysics by single-species Langmuir (or other types) of isotherms. Sorption behaviour involving more than a single site may also be realised applying user-defined isotherms. Note that these equations are required to be defined at a derivative form. The single-site Langmuir isotherm is available in fixed defined form according to:

$$C_{sorb} = \frac{cp_{max} K_L c}{1 + K_L c} \tag{4}$$

Where C_{sorb} and c denote the concentrations of sorbed species [mol kg^{-1}] and species in the aqueous phase [mol m^{-3}], respectively. K_L is the affinity constant [m^3 mol^{-1}] and cp_{max} the sorption capacity [mol kg^{-1}]. Linear sorption behaviour was attained by adequately choosing K_L (normally $K_L = 1$) relative to the experimental concentrations c. For $K_L c << 1$, the right-hand term in the denominator can be neglected and eq. (4) reduces to

$$C_{sorb} = cp_{max} K_L c = R_d c, \text{ with } R_d = cp_{max} K_L \tag{5}$$

K_L and cp_{max} have therefore no physical meaning under such conditions and only R_d is specified as an experimental result.

2.3.2 Multicomponent modelling using Phreeqc

The details for speciation calculations performed in Phreeqc are described in Glaus et al. (2020). The thermodynamic data used for speciation calculations are given in the Appendix (cf. Tab. A-1 and Tab. A-2). The Davies equation was used for the calculation of activity coefficients (Davies 1962). Two illustrative template input files are given in the Appendix.

3 Sorption and diffusion properties of Mn(II) in compacted illite

3.1 Overview of experimental conditions

The in-diffusion of $^{54}Mn^{2+}$ was measured as a function of pH and at a constant ionic strength of 0.1 M ("K-series") and as a function of ionic strength at a constant pH of 5 ("S-series"). Further the concentration of stable isotope Mn was varied under the conditions of pH 5 and an ionic strength of 0.1 M ("I-series"). A detailed overview of the experiments can be taken from Tab. 3-1 and Tab. 3-2.

Tab. 3-1: Overview of the experimental conditions for the in-diffusion experiments of Mn tracer in IdP in experiment 18008.TON

The initial activity of the ^{54}Mn tracer was ~ 100 Bq/ml. The volume of the tracer source solution was ~ 60 ml.

Experiment	ρ_{bd} [a] [kg m^{-3}]	**pH** [b]	**Background electrolyte** [c]	**Stable Mn** [M]	**Duration of in-diffusion** [d]
K4	1'701	4.0	0.1 M NaCl	2.5×10^{-6} [d]	60
K5	1'706	5.0	0.1 M NaCl	2.5×10^{-6} [d]	51
K6	1'700	6.0	0.1 M NaCl	2.5×10^{-6} [d]	92
K7	1'701	7.0	0.1 M NaCl	2.5×10^{-6} [d]	92
K8	1'704	8.0	0.1 M NaCl	2.5×10^{-6} [d]	92
S001	1'701	5.0	0.01 M NaCl	2.5×10^{-6} [d]	60
S003	1'700	5.0	0.03 M NaCl	2.5×10^{-6} [d]	60
S006	1'705	5.0	0.06 M NaCl	2.5×10^{-6} [d]	60
S01	1'701	5.0	0.1 M NaCl	2.5×10^{-6} [d]	60
S03	1'708	5.0	0.3 M NaCl	2.5×10^{-6} [d]	60
I5	1'708	5.0	0.1 M NaCl	1.0×10^{-3} [e]	51
I5b	1'702	5.0	0.1 M NaCl	1.0×10^{-3} [e]	14
I5c	1'706	5.0	0.1 M NaCl	1.0×10^{-4} [e]	14

[a] Bulk-dry density
[b] Target values. The effective values were monitored twice during1he course of 1he in-diffusion phase. They were in agreement withthe target values wi1hin less than 0.1 pH unit.
[c] Apart from the main electrolyte, the solutions were amended with 2 mM of buffer (acetate for pH 4, MES for pH 5 and 6, MOPS for pH 7, TRIS for pH 8) and 0.1 mM KCl.
[d] Resulting from the background of stable Mn in the ^{54}Mn tracer stock solution.
[e] Resulting from additional addition of stable $MnCl_2$ to the experimental solution.

Tab. 3-2: Overview of the experimental conditions for the in-diffusion experiments of Mn tracer in IdP in experiment 20001.TON

The initial activity of the ^{54}Mn tracer was ~ 100 Bq/ml. The volume of the tracer source solution was ~ 80 ml.

Experiment	ρ_{bd} [a] [kg m^{-3}]	**pH** [b]	**Background electrolyte** [c]	**Stable Mn** [M]	**Stable Ni** [M]	**Duration of in-diffusion** [d]
1.7A1	1'701	7.3	0.1 M NaCl	6.5×10^{-6} [d]	None	20
1.7A2	1'706	7.3	0.1 M NaCl	1.0×10^{-4} [e]	None	20
1.7B1	1'700	7.3	0.1 M NaCl	2.5×10^{-6} [d]	Yes [f]	20
1.7B2	1'706	7.3	0.1 M NaCl	1.0×10^{-4} [e]	Yes [f]	20

[a] Bulk-dry density

[b] Target values. The effective values were monitored twice during the course of the in-diffusion phase. They were in agreement with the target values within less than 0.1 pH unit.

[c] Apart from the main electrolyte, the solutions were amended with 2 mM of MOPS buffer and 0.1 mM KCl.

[d] Resulting from the background of stable Mn in the ^{54}Mn tracer stock solution.

[e] Resulting from additional addition of stable $MnCl_2$ to the experimental solution.

[f] For these experiments, the illite was pre-conditioned with an appropriate amount of Ni^{2+} to saturate the so-called strong edge sites. Owing to the long saturation phase of these experiments ("Corona caused"), it has to be assumed that this inventory of Ni^{2+} was already exempted to large extents during the saturation phase of the experiments, resulting in similar starting conditions as for the experiments 1.7A1 and 1.7A2.

3.2 Results and single-species modelling

In contrast to diffusion experiments with Eu^{3+} for example, no significant amounts (less than 2%) of the total tracer mass were recovered by acid extraction from the equipment. A mass balance comparing the loss of tracer mass from the source reservoir solution and the amounts recovered from the clay after in-diffusion (and from the equipment) was fulfilled to less than 5% of the total tracer mass. These findings support the integrity of the numerical evaluation of results.

Tab. 3-3 shows an overview of the best-fit parameter values and their uncertainties (expressed as confidence intervals on a 95% level) of the experiments carried out with trace Mn concentrations.

Fig. 3-1 shows the dependence of the $D_{e,c}$ and R_d values as a function of the ionic strength. The observed $D_{e,c}$ values are larger than the expected values for a simple pore diffusion model. This indicates that surface diffusion effects are present. The right-hand plot of Fig. 3-1 shows that R_d values are less impacted than $D_{e,c}$ values. Fig. 3-2 shows that no direct proportionality exists between $D_{e,c}$ and R_d values . This suggests that different surface species with different surface mobilities are responsible for the uptake of Mn^{2+} at the illite surface. These observations are fully in agreement with previously observed behaviour of illite towards Co^{2+} and Zn^{2+} (Glaus et al. 2015a).

Tab. 3-3: Summary of the best-fit parameter values and their uncertainties on a 95% confidence level as obtained from single-species diffusion simulations in Comsol Multiphysics®

Shown are the results of the experiments carried out at trace Mn concentrations.

Experiment	pH	I [a]	$D_{e,c}$ [m^2 s^{-1}]	R_d [dm^3 kg^{-1}]	$D_{e,f}$ [m^2 s^{-1}]
K4	4.0	0.1	$(6.5^{+8.9}_{-4.0}) \times 10^{-10}$	$(3.4^{+7.1}_{-2.4}) \times 10^{2}$	$(3.0^{+0.3}_{-0.3}) \times 10^{-10}$
K5	5.0	0.1	$(6.0^{+1.5}_{-1.1}) \times 10^{-10}$	$(7.0^{+2.0}_{-1.5}) \times 10^{2}$	$(4.8^{+0.9}_{-0.8}) \times 10^{-10}$
K6	6.0	0.1	$(8.9^{+3.4}_{-2.3}) \times 10^{-10}$	$(1.8^{+0.7}_{-0.5}) \times 10^{3}$	$(2.8^{+0.5}_{-0.4}) \times 10^{-10}$
K7	7.0	0.1	$(1.6^{+1.0}_{-0.5}) \times 10^{-9}$	$(4.0^{+2.6}_{-1.4}) \times 10^{3}$	$(2.8^{+0.5}_{-0.4}) \times 10^{-10}$
K8	8.0	0.1	$(1.2^{+0.5}_{-0.3}) \times 10^{-9}$	$(3.6^{+1.5}_{-1.0}) \times 10^{3}$	$(4.0^{+0.8}_{-0.7}) \times 10^{-10}$
S001	5.0	0.01	$(1.9^{+1.1}_{-1.1}) \times 10^{-8}$	$(7.0^{+3.7}_{-3.7}) \times 10^{3}$	$(4.8^{+0.9}_{-0.8}) \times 10^{-10}$
S003	5.0	0.03	$(5.9^{+11}_{-3.4}) \times 10^{-9}$	$(2.1^{+4.7}_{-1.2}) \times 10^{3}$	$(3.3^{+0.7}_{-0.5}) \times 10^{-10}$
S006	5.0	0.06	$(2.9^{+4.4}_{-1.5}) \times 10^{-9}$	$(1.5^{+2.4}_{-0.8}) \times 10^{3}$	$(2.3^{+0.5}_{-0.4}) \times 10^{-10}$
S01	5.0	0.1	$(6.5^{+2.2}_{-1.5}) \times 10^{-10}$	$(6.8^{+2.5}_{-1.7}) \times 10^{2}$	$(3.7^{+0.7}_{-0.6}) \times 10^{-10}$
S03	5.0	0.3	$(1.8^{+0.4}_{-0.3}) \times 10^{-10}$	$(3.7^{+1.0}_{-0.7}) \times 10^{2}$	$(4.4^{+0.9}_{-0.7}) \times 10^{-10}$
1.7A1	7.3	0.1	$(1.0^{+0.4}_{-0.4}) \times 10^{-9}$	$(2.6^{+0.9}_{-0.9}) \times 10^{3}$	$(3.2^{+0.1}_{-0.9}) \times 10^{-10}$
1.7B1	7.3	0.1	$(8.0^{+63}_{-6.6}) \times 10^{-10}$	$(1.6^{+11}_{-1.5}) \times 10^{3}$	$(2.8^{+0.5}_{-0.4}) \times 10^{-10}$

[a] Approximate ionic strength [M], when only taking into account the presence of NaCl as electrolyte.

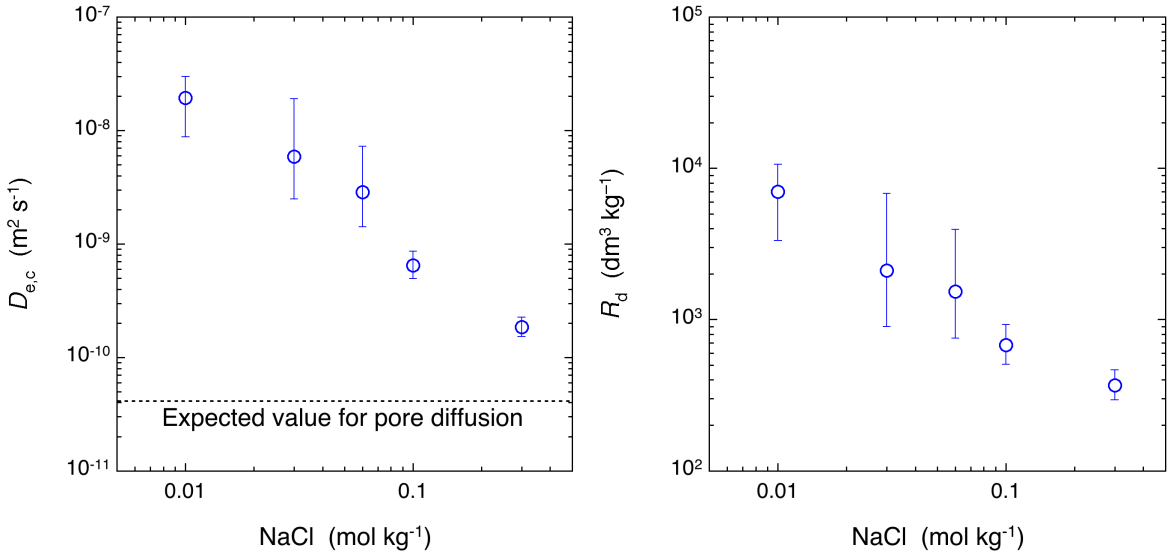

Fig. 3-1: Dependence on the ionic strength of the best-fit parameter values $D_{e,c}$ and R_d values at trace Mn concentrations, pH 5 and ρ_{bd} 1'700 kg m^{-3} ("S-Series")

The expected value for pore diffusion is derived from the bulk diffusion coefficient of Mn^{2+} and the effective diffusion coefficient of tritiated water in illite at a bulk-dry density of 1'700 kg m^{-3}.

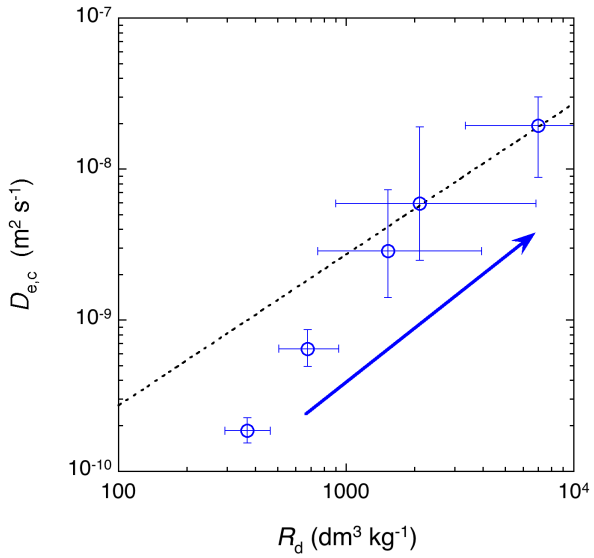

Fig. 3-2: Relationship between $D_{e,c}$ and R_d values shown in Fig. 3-1

The blue arrow indicates the ionic strength decreasing in the data from left to right. The black dotted line is a linear correlation with intercept set to zero. It shows that $D_{e,c}$ and R_d values are not linearly correlated.

Fig. 3-3 shows the respective parameter dependence on pH. The R_d values exhibit the typically expected pH dependence for species forming surface complexes at the so-called edge sites, because the protonation state of these sites is pH dependent. $D_{e,c}$ values, however, do only show a weak dependence on pH. This behaviour is again in line with the observations made with Co^{2+} and Zn^{2+} and suggests that the surface mobility is related to species bound at the planar sites, because the charge density of those sites is independent of pH.

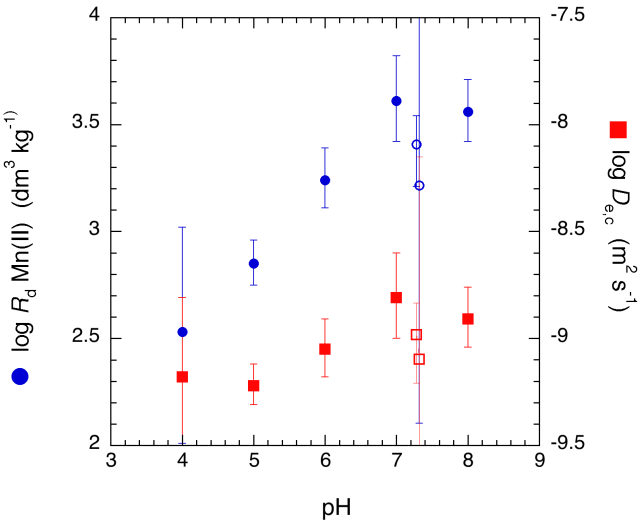

Fig. 3-3: $D_{e,c}$ and R_d values as a function of pH (trace Mn conditions, ionic strength 0.1 M, ρ_{bd} 1'700 kg m^{-3}, "K-series")

The in-diffusion times for the data shown as closed symbols was longer than those shown as open symbols. The respective uncertainties of the latter data tend thus to be larger.

3.3 Interpretation of the results in terms of an EDL sorption and diffusion model

The parametrisation of the 2SPNE SC/EDL model for Mn(II) was implemented in a sequential manner. In a first step, the $D_{e,c}$ and R_d data of the experiments carried out at trace Mn concentrations (cf. Tab. 3-3) are considered only. This step is rather straightforward, because $D_{e,c}$ and R_d values can be treated as constants under these conditions. The sets of thermodynamic data obtained thereby are then tested in a second step to the experimental data obtained at larger Mn concentrations. Note that the Mn concentration profiles in the clay measured after in-diffusion can be interpreted in terms of sorption isotherms. Although these profile data only provide the total concentration of Mn in the clay sample, they implicitly contain the information of the solution concentration as the result of the conformity of the total clay concentrations with the diffusion equation (Fick's first and second laws): The depth of the diffusion profile and thus also the solution concentrations in the clay pores are governed by the effective diffusion coefficients involved. The solution concentrations and the isotherm behaviour can thus be derived from the total clay concentrations and the respective diffusion properties used to simulate these values. For this reason, the isotherms obtained thereby do not exhibit the same independent character as sorption isotherms measured in batch type experiments; they are indirectly depending on the assumptions taken for diffusion. In view of the inadequacies mentioned in Section 2.3 regarding both the Comsol Multiphysics and Phreeqc models, the interpretation of the experimental diffusion data in terms of sorption isotherms is inaccurate to some degree. However, this

uncertainty is of similar order of magnitude as the experimental uncertainties of the tracer profile data and can thus be tolerated for a basic discrimination of different thermodynamic scenarios related to the experimental data.

Except from these restrictions, the information provided from the diffusion experiments in the section on Mn(II) allows thus for a comprehensive comparison of the sorption properties of the illite system both in terms of experiments carried out in dilute suspensions and densely compacted clay samples.

3.3.1 Data fitting with respect to pH edge data

Tab. 3-4 provides a compilation of thermodynamic interaction constants for the illite surface which show a valuable agreement with the diffusion data measured as a function of pH at trace concentrations of Mn. Note that all values with the exception of those for Mn^{2+} are fixed (literature values), while only those of Mn^{2+} were fitted (by eye) to the experimental data given in Tab. 3-3. For simplicity, the viscosity factor, q_η, was chosen as 1. Note that in previous work (Glaus et al. 2015a), optimum values for this factor for bivalent cations were found to be 0.4. The observed changes in the fitted curves for these values fall within the range of experimental uncertainties. Consequently, this study refrained from further refining this parameter for the given data.

Tab. 3-4: Thermodynamic data used for modelling the in-diffusion data of Mn(II) in illite compacted to bulk-dry density of 1'700 kg m^{-3}

The values of the interaction constants of Mn^{2+} with the strong sites and the Stern layer sites were optimised to the experimental data measured as a function of pH. All other constants are literature values (Appelo & Wersin 2007, Bradbury & Baeyens 2009a, Glaus et al. 2015a, Marques Fernandes et al. 2015, Montoya et al. 2018).

Site types	**Strong sites**	**Weak sites (#1)**	**Stern layer sites**
Site capacities (equiv kg^{-1})	2×10^{-3}	4×10^{-2}	1.9×10^{-1}
Formation constants [a] for the addition of	${}^{s}\beta$	${}^{w\#1}\beta$	${}^{Su}K$
H^+	6.2 / 4.0 [b]	6.2 / 4.0 [b]	-0.8
Na^+	-	-	-0.7
K^+	-	-	0.654
Mg^{2+}	-	-	0.107
Ca^{2+}	-	-	0.104
Al^{3+}	-	-	0.3
Mn^{2+}	0.55 [c]	-2.5 [d]	1.3

[a] ^{10}log values

[b] Stepwise protonation of strong and weak sites ($\equiv SO^-$), viz. $\equiv SO^- + H^+ = \equiv SOH$ and $\equiv SOH + H^+ = \equiv SOH_2^+$

[c] $\equiv S^SOH + Me^{2+} = \equiv S^SOMe(OH)_{j-1}^{2-j} + jH^+$; j = 1,2,3, where $\equiv S^SOH$ is the mono-protonated strong surface site and Me a divalent metal cation.

[d] $\equiv S^WOH + Me^{2+} = \equiv S^WOMe(OH)_{j-1}^{2-j} + jH^+$; j = 1,2, where $\equiv S^WOH$ is the mono-protonated weak surface sites.

Fig. 3-4 shows a comparison of the experimental results with the Phreeqc simulations using the thermodynamic data of Tab. 3-4. At ionic strength of 0.1 M, sorption is dominated by the planar surfaces at pH values less than ~ 5, while at higher pH values, sorption is dominated by the strong edge sites. The weak edge sites have ancillary importance for all experiments carried out at trace Mn concentrations. This underlines the uncritical choice of the value chosen in Tab. 3-4 which has been estimated from analogy considerations with the respective interaction constant published for Co^{2+} (Marques Fernandes et al. 2015, Montoya et al. 2018). Further, the surface complexation constant for the Stern layer sites produces a rather large selectivity for the exchange of Na^{+} for Mn^{2+}. With lower values, it would not be possible to reproduce the R_d values at pH ~ 4. Increasing the surface complexation constants of the strong sites cannot control this situation, because such an option would lead to a dramatic overestimation of the R_d values at higher pH values. The thermodynamic data set is thus in some contradiction with the commonly known cation exchange behaviour of illite.

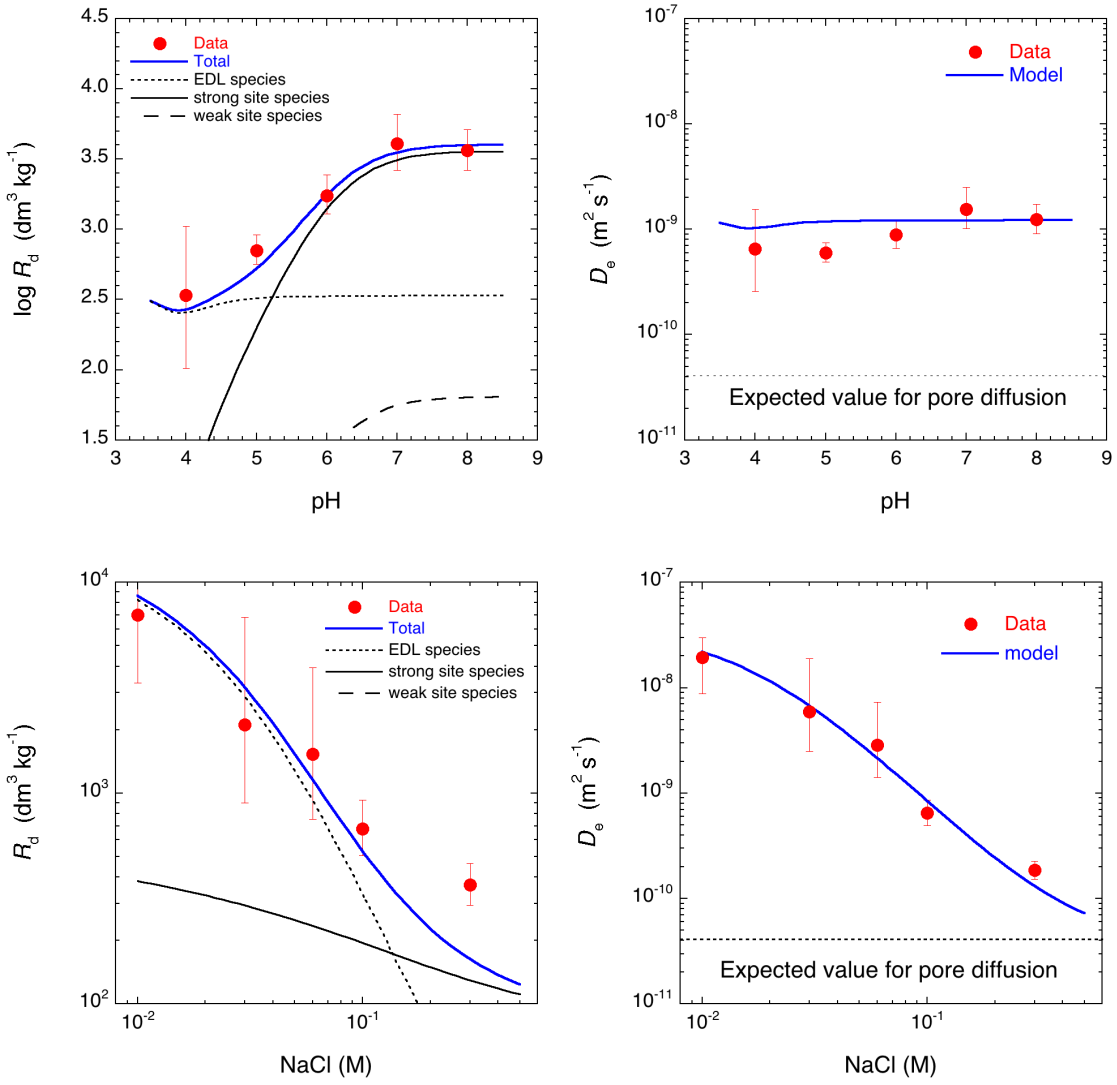

Fig. 3-4: $D_{e,c}$ and R_d values as a function of pH and ionic strength and thermodynamic simulations based on the data set given in Tab. 3-4 for the experiments carried out at trace Mn conditions (ρ_{bd} 1'700 kg m^{-3})

Note that the term EDL species comprises both Stern and diffuse layer species.

3.3.2 Optimisation with respect to the 'salinity data'

Tab. 3-5 shows a compilation of thermodynamic interaction constants for the illite surface which produce a valuable agreement with the diffusion data measured as a function of ionic strength. Note that all values with exception of those for Mn^{2+} are fixed from the literature, while only those of Mn^{2+} were fitted (by eye) to the experimental data given in Tab. 3-3. In agreement with the previous scenario, q_η was chosen to be 1.

Tab. 3-5: Thermodynamic data used for modelling the in-diffusion data of Mn(II) in illite compacted to bulk-dry density of 1'700 kg m^{-3}

The values of the interaction constants of Mn^{2+} were optimised to the experimental data measured as a function of the ionic strength. All other constants are literature values (Appelo & Wersin 2007, Bradbury & Baeyens 2009a, Glaus et al. 2015a, Montoya et al. 2018).

Site types	**Strong sites**	**Weak sites (#1)**	**Stern layer sites**
Site capacities (equiv kg^{-1})	2×10^{-3}	4×10^{-2}	1.9×10^{-1}
Formation constants [a] for the addition of	${}^{s}\beta$	${}^{w\#1}\beta$	${}^{Su}K$
H^+	6.2 / 4.0 [b]	6.2 / 4.0 [b]	-0.8
Na^+	-	-	-0.7
K^+	-	-	0.654
Mg^{2+}	-	-	0.107
Ca^{2+}	-	-	0.104
Al^{3+}	-	-	0.3
Mn^{2+}	1.1 [c]	-2.5 [d]	1.0

[a] ^{10}log values

[b] Stepwise protonation of strong and weak sites ($\equiv SO^-$), viz. $\equiv SO^- + H^+ = \equiv SOH$ and $\equiv SOH + H^+ = \equiv SOH_2^+$

[c] $\equiv S^SOH + Me^{2+} = \equiv S^SOMe(OH)_{j-1}^{2-j} + jH^+$; j = 1,2,3, where $\equiv S^SOH$ is the mono-protonated strong surface site and Me a divalent metal cation.

[d] $\equiv S^WOH + Me^{2+} = \equiv S^WOMe(OH)_{j-1}^{2-j} + jH^+$; j = 1,2, where $\equiv S^WOH$ is the mono-protonated weak surface sites.

Fig. 3-5 shows a comparison of the experimental results with the Phreeqc simulations using the thermodynamic data of Tab. 3-5. The agreement with the experimental data with the present set of thermodynamic data is markedly less for the data at pH > 6. This agrees with the previous discussion of reducing the selectivity of the cation exchange and concomitantly increasing the surface complexation constants for the strong sites which is provided by the difference of the data shown in Tab. 3-4 and Tab. 3-5. Regarding the reduced agreement of the fit curves with the experimental data at higher pH values, only the thermodynamic data from Tab. 3-4 are further considered for the following discussion of diffusion data measured at higher Mn concentrations.

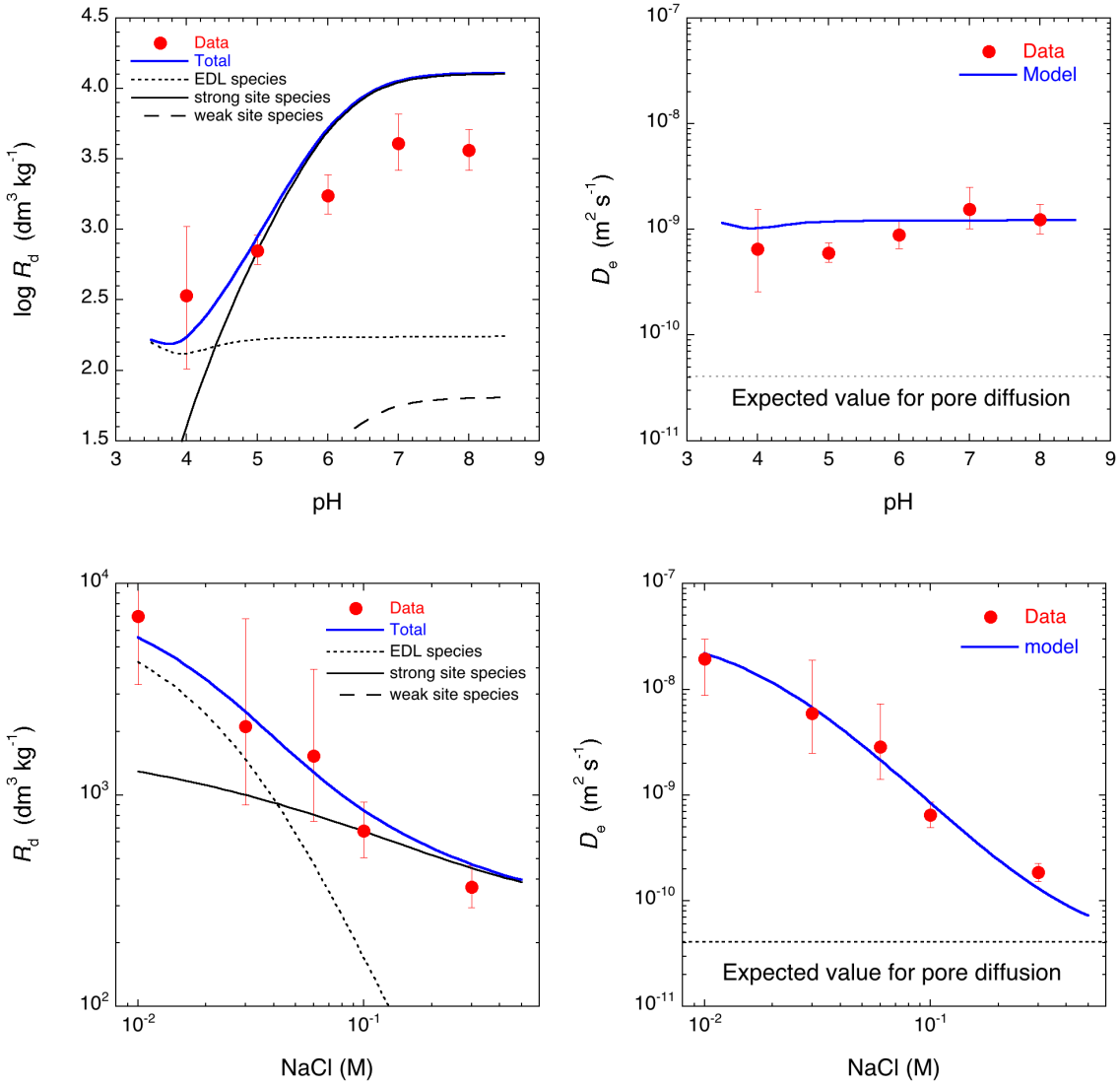

Fig. 3-5: $D_{e,c}$ and R_d values as a function of pH and ionic strength and thermodynamic simulations based on the data set given in Tab. 3-5 for the experiments carried out at trace Mn conditions (ρ_{bd} 1'700 kg m^{-3})

Note that the term EDL species comprises both Stern and diffuse layer species.

3.3.3 Optimisation with respect to the 'isotherm data'

Fig. 3-6 shows the sorption isotherm for pH 5 and ionic strength of 0.1 M calculated using the thermodynamic data set given in Tab. 3-4.

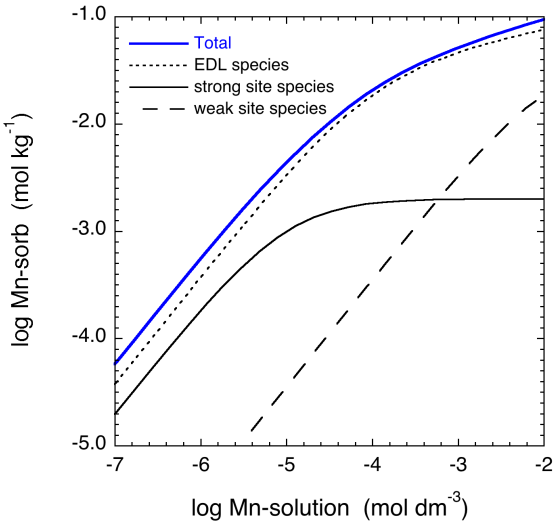

Fig. 3-6: Sorption isotherm calculated for pH 5 and an ionic strength of 0.1 M using the thermodynamic data set given in Tab. 3-4

Note that the term EDL species comprises both Stern and diffuse layer species.

For obtaining a qualitative comparison with diffusion data carried out using larger concentrations of Mn, the isotherm shown in Fig. 3-6 can be directly compared with the diffusion data of experiment I5b (cf. Tab. 3-1). The results of this experiment are shown in Fig. 3-7.

The profile data in Fig. 3-7 shows a good fit when using a constant R_d sorption model with R_d = 22 dm^3 kg^{-1}. The R_d values read out from Fig. 3-7 in the relevant concentration range between 0.1 and 1 mM vary between approximately 50 and 200 dm^3 kg^{-1}. This shows that the sorption model based on the data set given in Tab. 3-4 may be applicable for Mn concentrations in the concentration range below 1 µM. At higher Mn concentrations, however, it overestimates sorption. This discrepancy cannot be readily fixed because the diffusion depth observed in the experiments which is related to the involved $D_{e,c}$ values, is also required to be in agreement with the thermodynamic speciation model. If sorption has to be reduced for the conditions shown in Fig. 3-7, modification of the thermodynamic data for surface species bound to the planar surfaces is required. Such a step may also have an impact on the diffusion behaviour, because the mobile surface species are assumed to be those in the diffuse layer at the planar surfaces.

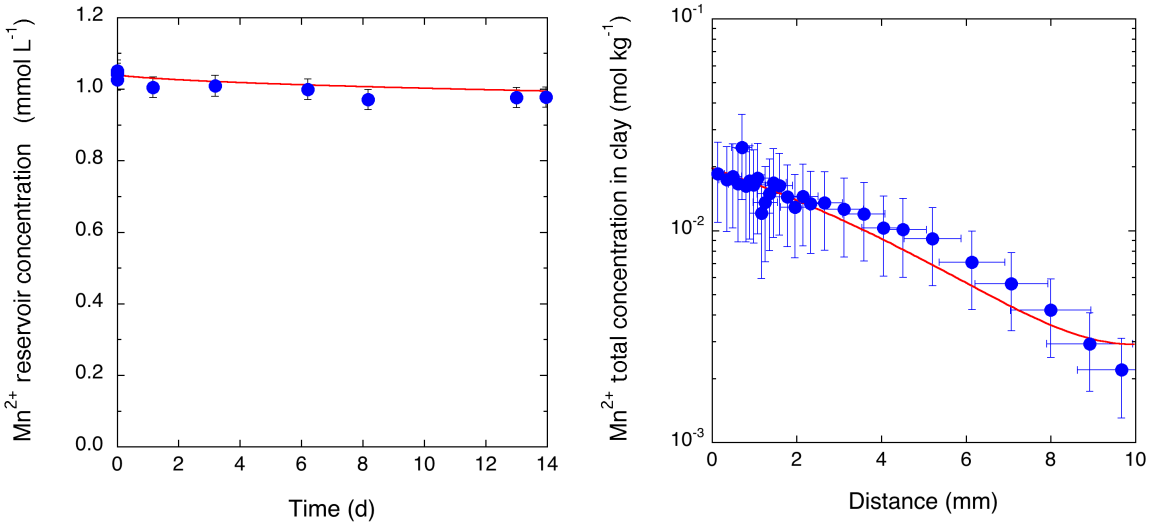

Fig. 3-7: Evolution of upstream reservoir solution concentration of Mn^{2+} (left plot) and total Mn^{2+} concentration (per dry clay) in the clay segments (right plot) in experiment I5b

Best-fit curves obtained from a Comsol Multiphysics simulation involving single-species, constant-R_d diffusion are shown as red lines.

One possibility to correct for this conflict is decreasing the surface complexation properties of the Stern layer sites because these surface species are assumed to be immobile. However, this leads to a reduction of sorption at lower pH values which cannot be compensated by increasing the sorption strength of other existing sorption sites (cf. the discussion in Section 3.3.1). Consequently, additional sites would have to be introduced. Although such a step is regarded as a pure fitting exercise and does not contribute to a better system understanding, the situation can be taxed as comparable to the data situation encountered for published data for the uptake of Co^{2+} and Zn^{2+} by illite. In the latter case, it was hypothesized that additional binding sites may be present which could explain the rather strong uptake of Zn^{2+} at trace conditions and low pH values (Montoya et al. 2018). In the case of Co^{2+} the modelled sorption edge clearly underestimated the experimental data at low pH (Bradbury & Baeyens 2009a). The introduction of an additional binding site would also have led to an improvement of the data fit in such a case.

For the present case of Mn^{2+} sorption on illite, an auxiliary binding site was introduced (denoted as *wx* sites in the following) with a site density of 5×10^{-4} equiv kg^{-1}. It is necessary to use a low value for site density, as otherwise the data at rather high concentrations of Mn^{2+} cannot be represented appropriately. The (de)protonation properties of these binding sites were also adapted in order that these sites are predominantly active at rather low pH values. Introducing auxiliary binding sites provides allows to decrease the surface complexation constants for the Stern layer sites leading to cation exchange selectivity closer to measured values (B. Baeyens, M. Marques Fernandez, personal communication). A tentative set of thermodynamic data which produced valuable fits of the diffusion data measured at trace and higher Mn concentrations is given in Tab. 3-6.

Tab. 3-6: Thermodynamic data used for modelling the in-diffusion data of Mn(II) in illite compacted to a bulk-dry density of 1'700 kg m^{-3}

For the optimisation of the surface complexation constants of Mn^{2+}, also the experiments carried out at higher background concentrations of stable Mn^{2+} were taken into account. All other constants are literature values (Appelo & Wersin 2007, Bradbury & Baeyens 2009a, Glaus et al. 2015a, Marques Fernandes et al. 2015, Montoya et al. 2018). Further, the protonation properties of the auxiliary sites were adapted in order that these sites are active predominantly at rather low pH values.

Site types	**Strong sites**	**Weak sites (#1)**	**Auxiliary sites**	**Stern layer sites**
Site capacities (mol kg^{-1})	2×10^{-3}	4×10^{-2}	5×10^{-4}	1.9×10^{-1}
Formation constants [a] *for the addition of*	$^{s}\beta$	$^{w\#1}\beta$	$^{wx}\beta$	^{Su}K
H^+	6.2 / 4.0 [b]	6.2 / 4.0 [b]	4.2 / (2.5) [b]	-0.8
Na^+	-	-	-	-0.7
K^+	-	-	-	0.654
Mg^{2+}	-	-	-	0.107
Ca^{2+}	-	-	-	0.104
Al^{3+}	-	-	-	0.3
Mn^{2+}	0.55 [c]	-2.5 [d]	2.3 [d]	0.3

[a] ^{10}log values

[b] Stepwise protonation of strong and weak sites ($\equiv SO^-$), viz. $\equiv SO^- + H^+ = \equiv SOH$ and $\equiv SOH + H^+ = \equiv SOH_2^+$

[c] $\equiv S^SOH + Me^{2+} = \equiv S^SOMe(OH)_{j-1}^{2-j} + jH^+$; j = 1,2,3, where $\equiv S^SOH$ is the mono-protonated strong surface site and Me a divalent metal cation.

[d] $\equiv S^WOH + Me^{2+} = \equiv S^WOMe(OH)_{j-1}^{2-j} + jH^+$; j = 1,2, where $\equiv S^WOH$ is the mono-protonated weak surface sites.

The comparison of the experimental results with the Phreeqc simulations using the thermodynamic data of Tab. 3-6 is illustrated in Fig. 3-8. The agreement with the experimental data represents a compromise between the scenarios shown in Fig. 3-4 and Fig. 3-5. In addition, the simulations are expected to be in better agreement with the experiments carried out at higher background concentrations of stable Mn^{2+} (shown in the following) and the cation exchange selectivity for Mn^{2+} is in better agreement with literature values. In all these respects, the data set presented in Tab. 3-6 can be regarded as a valuable description of Mn^{2+} sorption and diffusion data under most of the experimental conditions applied in the present work.

A comparison of Fig. 3-4 and Fig. 3-8 shows that the significance of the Stern layer species is strongly reduced at lower pH values and is compensated by the (formal) uptake of Mn^{2+} by the auxiliary sites. It is unclear whether this scenario can be successfully applied to all marginal conditions encountered in the present work due to the available data material being not fully comprehensive in that respect. The significant discrepancy between model curves and experimental R_d data at the lowest ionic strength suggests potential limitations.

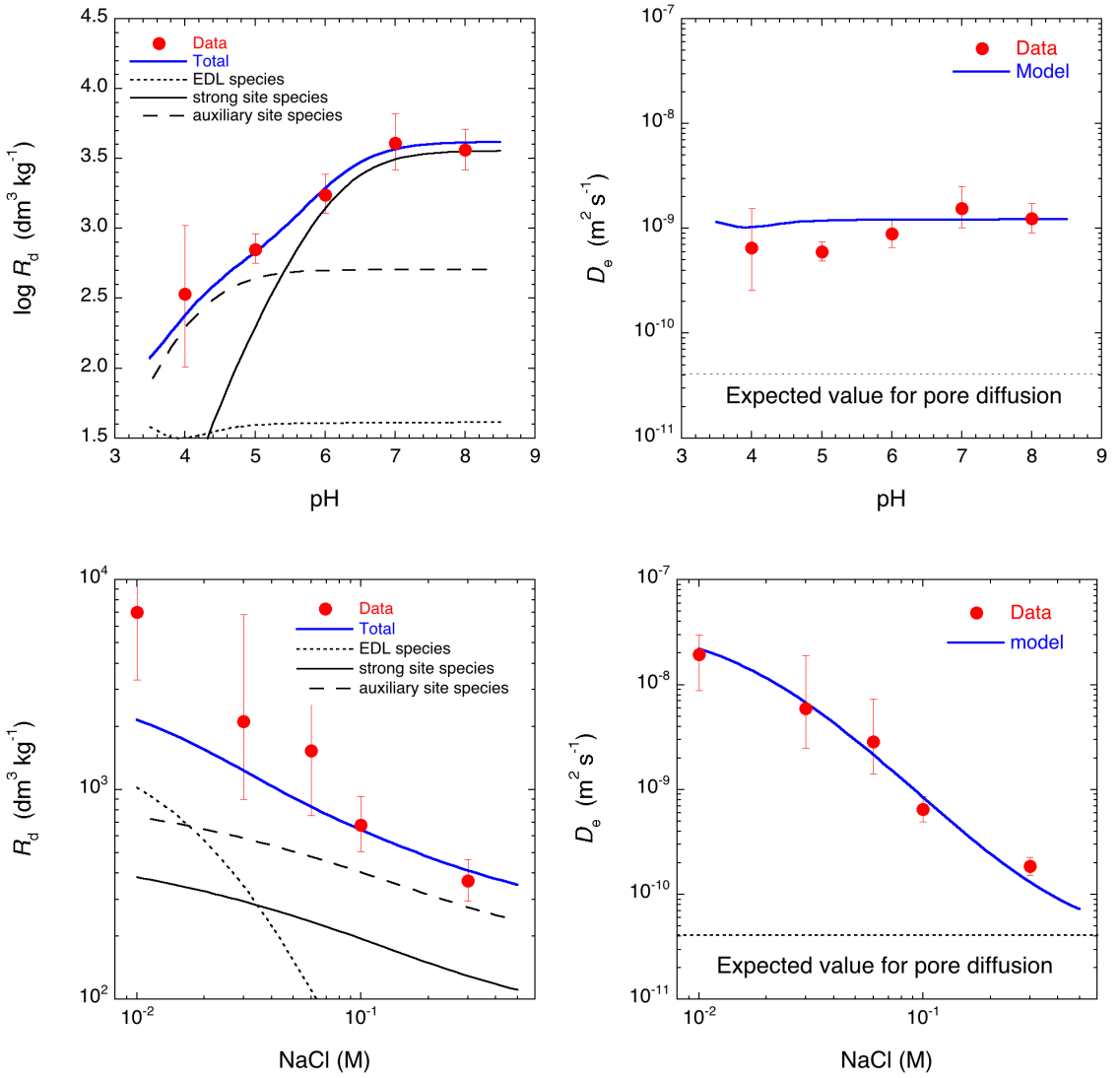

Fig. 3-8: $D_{e,c}$ and R_d values as a function of pH and ionic strength and thermodynamic simulations based on the data set given in Tab. 3-6 for the experiments carried out at trace Mn conditions (ρ_{bd} 1'700 kg m^{-3})

Note that the term EDL species comprises both Stern and diffuse layer species.

Fig. 3-9 shows the approximate model curves generated in Phreeqc based on the thermodynamic data set presented in Tab. 3-6 for experiment I5c using an initial background concentration of 0.1 mM of stable isotope Mn^{2+}. Although differences can be seen between the different model scenarios of Fig. 3-9, their importance is taxed as rather subordinated in view of the experimental uncertainties of the data and the inherent modelling uncertainties. In view of the fact that sorption tends to be overestimated in the Mn profile of Fig. 3-9, it would be possible to further optimise the surface complexation constant for the formation of the Stern layer species or the viscosity factor. However, the involved ranges of possible values are within ~ 0.2 units of the proposed values and result only in minor differences of the model curves. In view of the involved uncertainties of the experimental data and the modelling (discretisation in time and space, reduction to 1D geometry), all these attempts must be regarded as variations which do not produce a better system understanding. Rather it is proposed to treat these margins as parameter uncertainties.

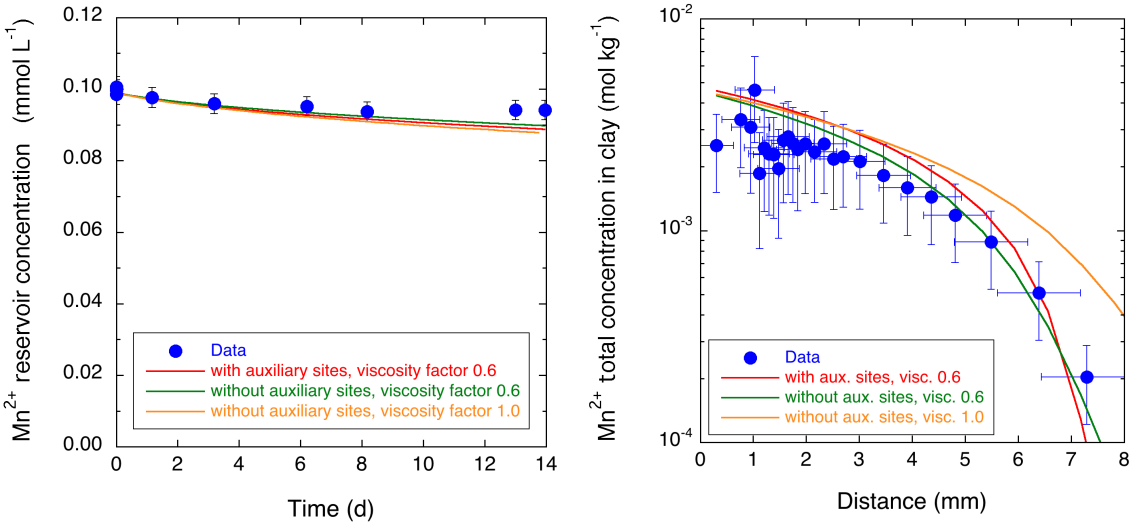

Fig. 3-9: Evolution of upstream reservoir solution concentration of Mn^{2+} (left-hand plot) and total Mn^{2+} concentration (per dry clay) in the clay segments (right-hand plot) in experiment I5c

The solid lines were obtained by numerical transport modelling using a 1-D Phreeqc transport model for the different model scenarios according to the legend.

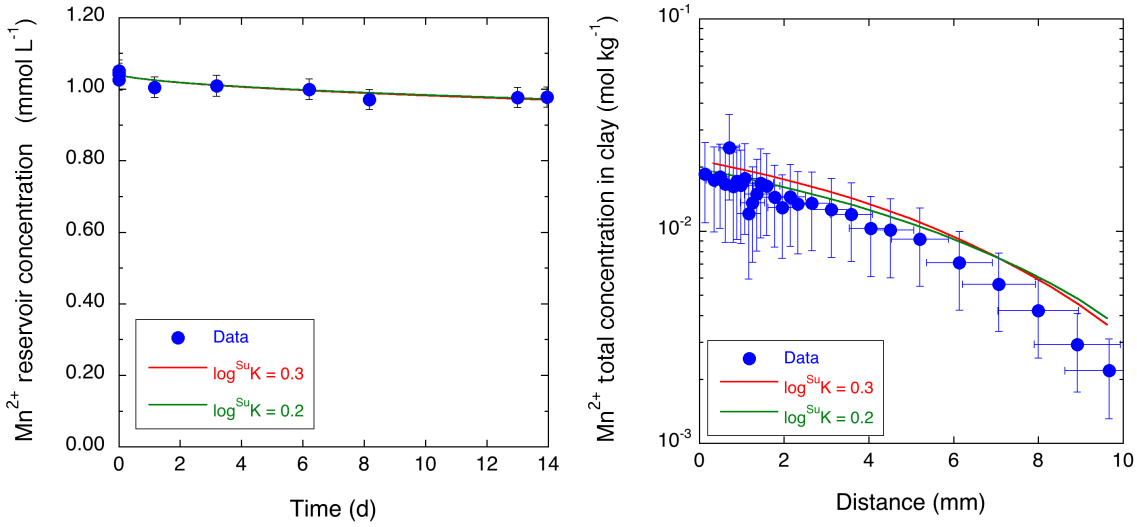

Fig. 3-10: Evolution of upstream reservoir solution concentration of Mn^{2+} (left-hand plot) and total Mn^{2+} concentration (per dry clay) in the clay segments (right-hand plot) in experiment I5b.

Best-fit curves obtained using a 1-D Phreeqc transport model are shown as solid lines

Fig. 3-10 shows a sensitivity analysis for the variation of the Stern layer surface complexation constant for experiment I5b. The disparities observed in the model are insignificant in relation to the uncertainties of the experiment.

The variations in the modelling curves between Fig. 3-7 and Fig. 3-10 illustrate to some degree the inaccuracies of both modelling approaches. They can, however, mainly be ascribed to the fact that the diffusion properties ($D_{e,c}$) in the Comsol Multiphysics model were particularly optimised with respect to the experimental data of experiment I5b, while they are the result of the global data set given in Tab. 3-6 for the Phreeqc simulation. These differences produce slightly different diffusion depths in the simulations shown in Fig. 3-7 and Fig. 3-10. The differences in sorption properties are rather subordinate for the resulting modelling curves.

Fig. 3-11 shows the isotherm at pH 5 and ionic strength of 0.1 M based on the thermodynamic data set of Tab. 3-6. The comparison to the isotherm shown in Fig. 3-6 demonstrates that the objective of reducing the effect of the sorption strength at elevated concentrations of Mn^{2+} has been accomplished using the data set of Tab. 3-6. For Mn^{2+} concentrations less than 1 µM, the disparities between the two sorption isotherms are almost negligible. Therefore, both underlying thermodynamic data sets can be utilisied for conducting experiments involving trace concentrations of Mn.

The majority of the profile data in experiment I5b comprises a pseudo-linear range of sorption around 10^{-2} mol kg^{-1} involving sorption at the planar surfaces, mostly. This is the reason why these data may rather appropriately be modelled using a single-species, constant R_d diffusion model, which is less applicable for the data of experiment I5c exhibiting profile data around 10^{-3} mol kg^{-1}. In this latter concentration range, sorption is dominated by almost all type of sorption sites involving EDL, strong edge and the auxiliary sites.

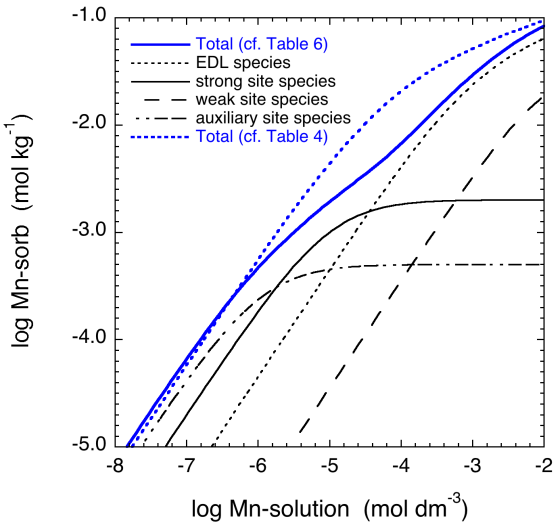

Fig. 3-11: Sorption isotherm for pH 5 and ionic strength of 0.1 M using the thermodynamic data set given in Tab. 3-6 (solid line)

The dotted line represents the sorption isotherm based on the data given in Tab. 3-4 and shown in Fig. 3-6.

The sole experimental cases that have not yet been addressed for far are experiments 1.7A2 and 1.7B2 which were carried out at pH 7.3 and ionic strength of 0.1 M using an initial concentration of 0.1 mM Mn^{2+}. Only the data of experiment 1.7A2 are discussed in the following because both data sets are practically indistinguishable. Under the conditions of higher pH values and higher concentrations of stable Mn^{2+}, it is expected that the weak sites (w#1) play a more important role. Fig. 3-12 shows the results of experiment 1.7A2 along with a blind prediction of the simulation using the thermodynamic data set of Tab. 3-6 and an optimised scenario using an adapted value for $^{w\#1}\beta$.

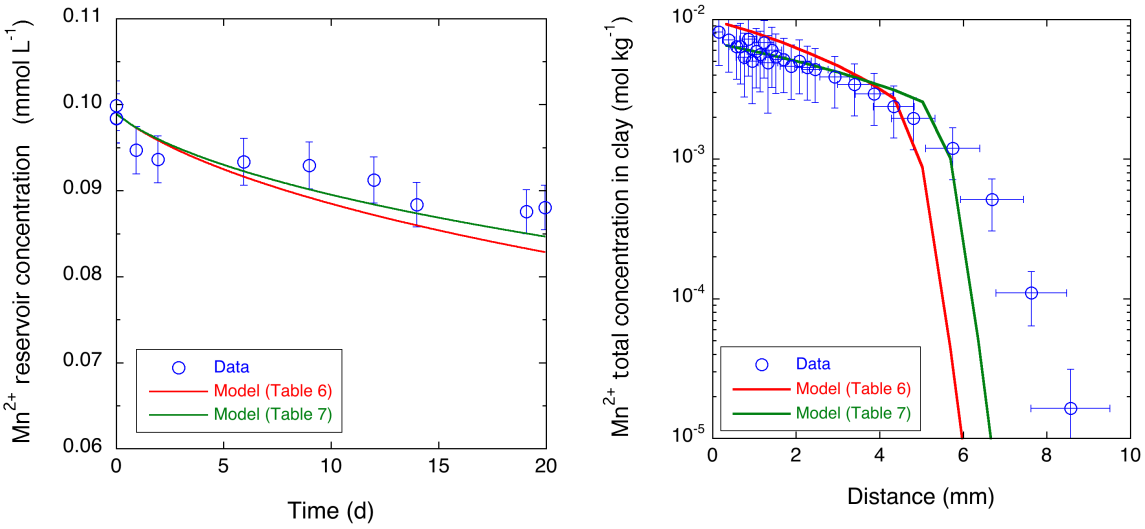

Fig. 3-12: Evolution of the upstream reservoir solution concentration of Mn^{2+} (left-hand plot) and the total Mn^{2+} concentration (per dry clay) in the clay segments (right-hand plot) in experiment 1.7A2

Model curves obtained using a 1-D Phreeqc transport model are shown as solid lines. The adaptation of the interaction constant of the weak sites lead to a slightly better fit.

The optimal value for $^{w\#1}\beta$ can readily be applied to all prior simulations because under those conditions, the weak sites only played a subordinate role for sorption. Tab. 3-7 provides an overview of the final optimum parameter values proposed to be used for the description of sorption and diffusion of Mn^{2+} in compacted illite.

Fig. 3-13 shows the respective sorption isotherm for pH 7.3 and an ionic strength of 0.1 M based on the thermodynamic data set given in Tab. 3-7. Final thermodynamic data proposed for modelling the in-diffusion data of Mn(II) in illite compacted to bulk-dry density of 1'700 kg m^{-3}The various site contributions show that the experimental data of experiment 1.7A2 are controlled by the *w#1* and the EDL sites at higher concentrations of stable Mn^{2+} and by the strong edge sites at lower concentrations. This is in strong contrast to the data at pH 5, where the surface species at the planar surfaces play a dominant role. The consistency between the results and the underlying modelling parameters under those conditions corroborates the validity of the latter and the broad applicability of the model.

Tab. 3-7: Final thermodynamic data proposed for modelling the in-diffusion data of Mn(II) in illite compacted to bulk-dry density of 1'700 kg m^{-3}

For the optimisation of the surface complexation constants of Mn^{2+}, also the experiments carried out at higher background concentrations of stable Mn^{2+} were taken into account. All other constants are literature values (Appelo & Wersin, 2007, Bradbury & Baeyens 2009a, Glaus et al. 2015a, Marques Fernandes et al. 2015, Montoya et al. 2018). A viscosity factor (q_η) of 0.6 was assumed for the characterisation of surface diffusion properties.

Site types	**Strong sites**	**Weak sites (#1)**	**Auxiliary sites**	**Stern layer sites**
Site capacities (mol kg^{-1})	2×10^{-3}	4×10^{-2}	5×10^{-4}	1.9×10^{-1}
Formation constants [a] *for the addition of*	${}^{s}\beta$	${}^{w\#1}\beta$	${}^{wx}\beta$	${}^{Su}K$
H^+	6.2 / 4.0 [b]	6.2 / 4.0 [b]	4.2 / (2.5) [b]	-0.8
Na^+	-	-	-	-0.7
K^+	-	-	-	0.654
Mg^{2+}	-	-	-	0.107
Ca^{2+}	-	-	-	0.104
Al^{3+}	-	-	-	0.3
Mn^{2+}	0.55 [c]	-2.8 [d]	2.3 [d]	0.3

[a] ^{10}log values

[b] Stepwise protonation of strong and weak sites ($\equiv SO^-$), viz. $\equiv SO^- + H^+ = \equiv SOH$ and $\equiv SOH + H^+ = \equiv SOH_2^+$

[c] $\equiv S^SOH + Me^{2+} = \equiv S^SOMe(OH)_{j-1}^{2-j} + jH^+$; j = 1,2,3, where $\equiv S^SOH$ is the mono-protonated strong surface site and Me a divalent metal cation.

[d] $\equiv S^WOH + Me^{2+} = \equiv S^WOMe(OH)_{j-1}^{2-j} + jH^+$; j = 1,2, where $\equiv S^WOH$ is the mono-protonated weak surface sites.

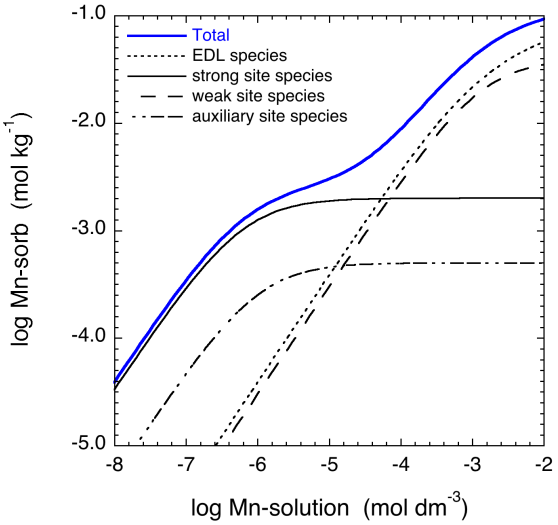

Fig. 3-13: Sorption isotherm for pH 7.3 and ionic strength 0.1 M using the thermodynamic data set given in Tab. 3-7 (solid line)

3.4 Conclusions

The section on Mn(II) diffusion proposes a set of thermodynamic data for the sorption of Mn^{2+} on illite, along with the relevant diffusion parameters. These model parameters were determined iteratively by subjectively comparing experimental data with the resulting model curves. A fundamental evaluation of true best-fit parameters and their uncertainties based on pure statistical methods is not possible for two reasons.

Firstly, the extent of parameter variations and the resulting number of experimental data is not sufficient to provide a comprehensive data basis considering the number of potentially adjustable parameters. Compared to common sorption experiments carried out in batch mode using dilute clay suspensions in which parameters like pH, ionic strength, presence of competing or complexing species are typically varied, the interpretation of the present diffusion experiments involves additional parameters, like the specific surface area of the clay, the thickness of the Donnan layer (via n_{DL}) and all diffusion related parameters involving the speciation of cations between the aqueous and the EDL phase and diffusion related mobility factors. Despite the rather complex coaction of different binding entities during the different experimental conditions, a rather unambiguous determination of parameter values is possible. Additionally, the estimation of uncertainties in these parameters is relatively tolerable.

Secondly, the computational tools used for the simulations exhibit certain minor deficiencies, and the effects on the results are difficult to quantify exactly. Although fully coupled computational tools like *i*Phreeqc (Nardi et al. 2014, Wissmeier & Barry 2011) or FEniCS–Reaktoro (Hax et al. 2020, Rolle et al. 2018) may be available, these tools are not directly applicable to the present case of EDL diffusion. Furthermore, the computational times involved in such calculations are presently long, which complicates a full statistical evaluation of diffusion results.

From these considerations, it becomes clear that the present case is rather fortuitous. It is not guaranteed that the full range of parameters needed for an unambiguous interpretation can be covered with just a few experiments.

4 Effects of the presence of competing metal cations on diffusion in compacted illite

4.1 Competition effects: Ca^{2+} on the diffusion of Co^{2+} tracer

The results of a series of experiments carried out at pH 5 and an ionic strength of 0.1 M NaCl are described in Glaus et al. (2021). They showed that the presence of Ca^{2+} in a NaCl electrolyte had a significant effect on the diffusion of $^{57}Co^{2+}$ at concentration levels larger than ~ 1 mM, while the effect on R_d was rather weaker. This was explained because of the competition between Ca^{2+} with $^{57}Co^{2+}$ in the EDL, leading to a decrease of mobile $^{57}Co^{2+}$ surface species. The competition between these two cations for sorption was less because under the experimental conditions, sorption is rather dominated by the strong edge surface complexes of $^{57}Co^{2+}$, for which the competition with Ca^{2+} is rather insignificant.

4.1.1 Overview of experimental conditions

Additional experiments were carried out at variable pH values (4, 5, 6, 7), two different ionic strengths (0.01 and 0.1 M) and two different conditions regarding the concentration of Ca^{2+}, viz. at 0.01 M and 10 mM. The former concentration is representative of the Ca^{2+} impurities of the clay after conditioning to the Na^+ form. The latter concentration can be regarded as a representative average for the Ca^{2+} concentration found in natural pore waters of clay rocks. This entire experimental test series is labelled as 21001.TON.

Regrettably, the outcomes of most experiments conducted at pH values of 6 and 7 were unsuccessful, and the underlying causes of these failures remain unknown. Instead of a continuously decreasing tracer profile, extended areas with a constant concentration of $^{57}Co^{2+}$ in the clays were found. Obvious reasons related to the solution composition could not be identified. A representative test in which the surface cations in the clay segments were measured by substitution with Cs^+ did not produce any irregularities compared to those at lower pH.

4.1.2 Results of in-diffusion tests and single-species modelling

The results of the experiments are shown in Fig. 4-1 to Fig. 4-4 along with the results of the single-species inverse modelling. Each plot shows the results summarised for a single pH value. The best-fit parameter values are given in Tab. 4-1. This table also provides the results of the analytical measurements performed after the last sampling of the reservoir solution during the in-diffusion phase. The provided values indicate that there are no exceptional outcomes that could account for the anomalous pattern observed in certain profiles. All results are within the ranges of expected values within the normal scope of uncertainties.

Tab. 4-1: Summary of the experimental conditions and the best-fit parameter values and their uncertainties on a 95% confidence level as obtained from single-species diffusion simulations in Comsol Multiphysics® for the experimental series 21001.TON

The table also shows the results of the analytical measurements by IC in the reservoir solutions after the in-diffusion phase.

Exp.	ρ_{bd} [kg m^{-3}]	pH [a]	[Na^+] [mM] [a]	[K^+] [mM] [a]	[Ca^{2+}] [mM] [a]	[Mg^{2+}] [mM] [a]	$D_{e,c}$ [m^2 s^{-1}]	R_d [dm^3 kg^{-1}]	$D_{e,f}$ [m^2 s^{-1}]
4A	1'706	4.1	12.9	0.25	0.009	0.014	$(1.9^{+1.1}_{-1.1}) \times 10^{-8}$	$(27^{+17}_{-17}) \times 10^{3}$	$(3.4^{+0.7}_{-0.5}) \times 10^{-10}$
4B	1'697	4.1	12.9	0.27	10.8	0.049	$(3.6^{+0.4}_{-0.4}) \times 10^{-10}$	$(1.9^{+0.24}_{-0.20}) \times 10^{3}$	$(2.4^{+0.6}_{-0.5}) \times 10^{-10}$
4C	1'701	4.1	109	0.25	0.051	0.052	$(7.1^{+0.7}_{-0.7}) \times 10^{-10}$	$(1.2^{+0.1}_{-0.1}) \times 10^{3}$	$(2.8^{+0.5}_{-0.4}) \times 10^{-10}$
4D	1'708	4.0	111	0.27	11.0	0.056	$(2.3^{+0.3}_{-0.3}) \times 10^{-10}$	$(6.9^{+1.0}_{-0.9}) \times 10^{2}$	$(2.8^{+0.5}_{-0.4}) \times 10^{-10}$
5A	1'706	5.0	13.6	0.25	0.009	0.004	$(4.6^{+3.7}_{-3.7}) \times 10^{-8}$	$(53^{+41}_{-41}) \times 10^{3}$	$(2.8^{+0.5}_{-0.4}) \times 10^{-10}$
5B	1'703	5.0	12.8	0.30	10.4	0.048	$(2.4^{+0.3}_{-0.3}) \times 10^{-10}$	$(5.7^{+0.7}_{-0.7}) \times 10^{2}$	$(2.8^{+0.6}_{-0.5}) \times 10^{-10}$
5C	1'700	5.1	106	0.18	0.044	0.030	$(7.8^{+1.4}_{-1.3}) \times 10^{-10}$	$(1.6^{+0.3}_{-0.2}) \times 10^{3}$	$(2.5^{+0.8}_{-0.2}) \times 10^{-10}$
5D	1'704	5.0	109	0.24	10.0	0.035	$(2.5^{+0.3}_{-0.4}) \times 10^{-10}$	$(1.1^{+0.2}_{-0.2}) \times 10^{3}$	$(2.5^{+0.5}_{-0.4}) \times 10^{-10}$
6A	1'707	6.3	12.4	0.18	0.014	0.003	2.3×10^{-7}	162×10^{3}	3.2×10^{-10}
6B	1'708	6.1	12.5	0.17	10.0	0.021	2.2×10^{-10}	7.8×10^{2}	3.2×10^{-10}
6C	1'706	6.2	105	0.18	0.038	0.032	n.a.	n.a.	n.a.
6D	1'704	6.1	106	0.20	10.2	n.a.	n.a.	n.a.	n.a.
7A	1'703	7.1	11.4	0.19	0.003	0.002	$(1.6^{+1.4}_{-1.4}) \times 10^{-7}$	$(202^{+176}_{-176}) \times 10^{3}$	$(3.7^{+0.3}_{-0.3}) \times 10^{-10}$
7B	1'703	7.2	11.5	0.21	10.1	0.017	$(2.7^{+0.4}_{-0.3}) \times 10^{-10}$	$(1.1^{+0.16}_{-0.15}) \times 10^{2}$	$(2.8^{+0.5}_{-0.4}) \times 10^{-10}$
7C	1'705	7.3	98	0.27	0.026	0.018	$(6.4^{+1.4}_{-1.1}) \times 10^{-10}$	$(1.7^{+0.4}_{-0.3}) \times 10^{3}$	$(2.8^{+0.5}_{-0.4}) \times 10^{-10}$
7D	1'702	7.3	103	0.22	10.1	0.017	2.1×10^{-10}	7.2×10^{2}	2.8×10^{-10}

[a] Measured in the reservoir solution after the last sampling

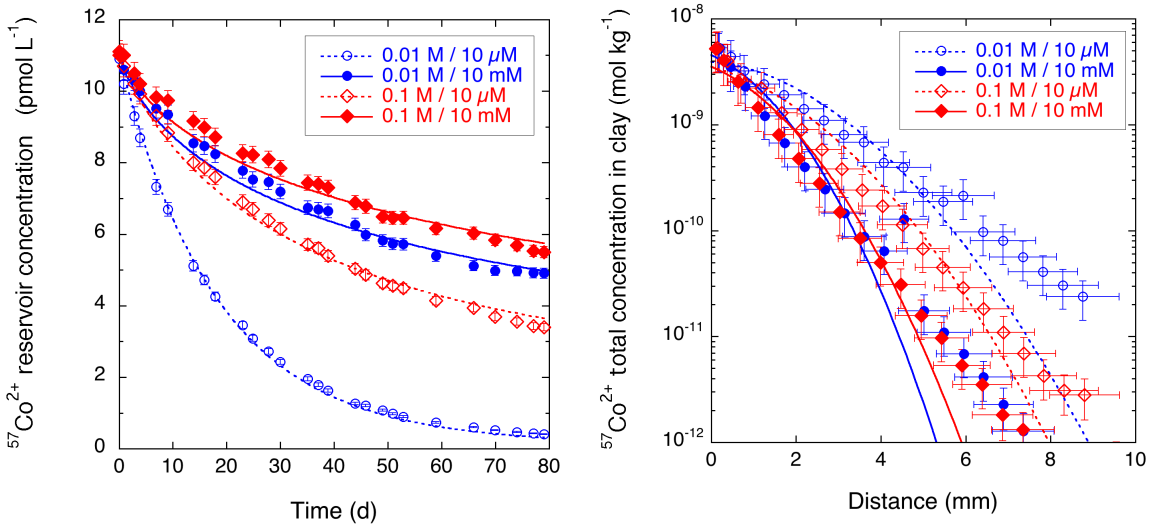

Fig. 4-1: Evolution of the upstream reservoir solution concentration of $^{57}Co^{2+}$ (left-hand plot) and the total $^{57}Co^{2+}$ concentration (per dry clay) in the clay segments (right-hand plot) in the experimental series 21001.TON at pH 4

The first number in the legend indicates the concentration of NaCl, the second the one of $CaCl_2$.

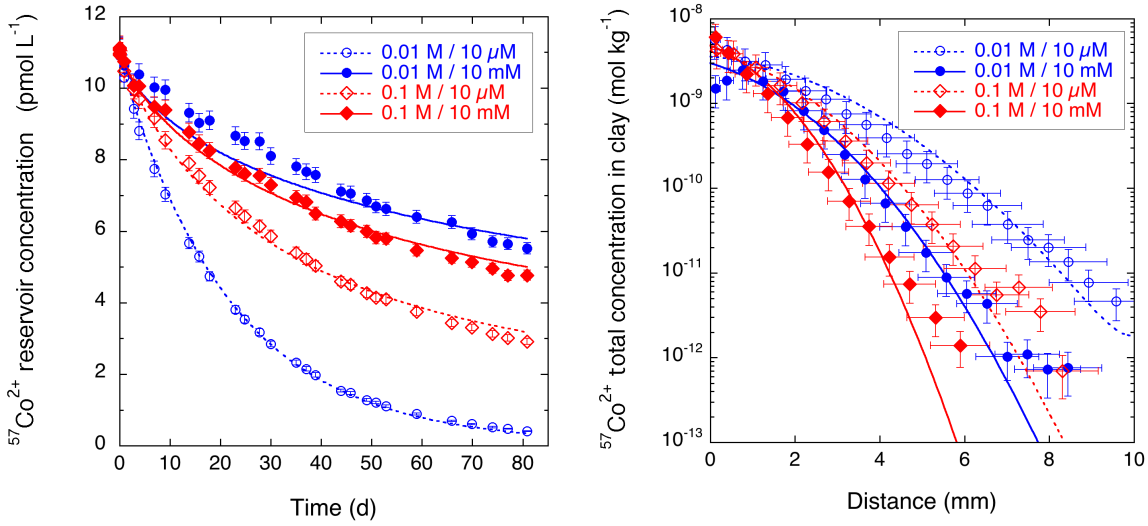

Fig. 4-2: Evolution of the upstream reservoir solution concentration of $^{57}Co^{2+}$ (left-hand plot) and the total $^{57}Co^{2+}$ concentration (per dry clay) in the clay segments (right-hand plot) in the experimental series 21001.TON at pH 5

The first number in the legend indicates the concentration of NaCl, the second the one of $CaCl_2$.

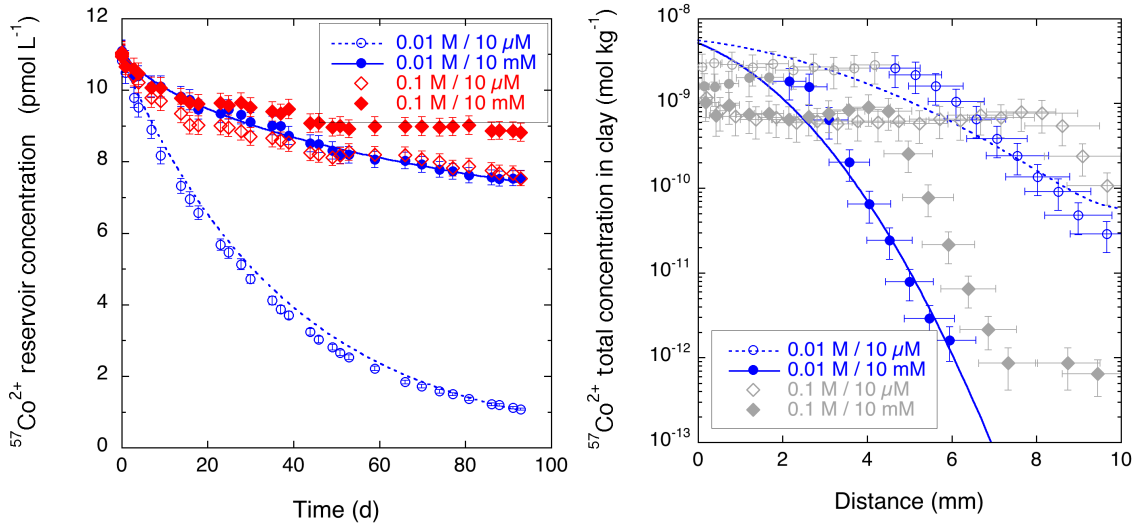

Fig. 4-3: Evolution of the upstream reservoir solution concentration of $^{57}Co^{2+}$ (left-hand plot) and the total $^{57}Co^{2+}$ concentration (per dry clay) in the clay segments (right-hand plot) in the experimental series 21001.TON at pH 6

No fit curves were calculated for the data at 0.1 M ionic strength because the profile data were obviously biased by unknown artefacts (grey data) The first number in the legend indicates the concentration of NaCl, the second the one of $CaCl_2$.

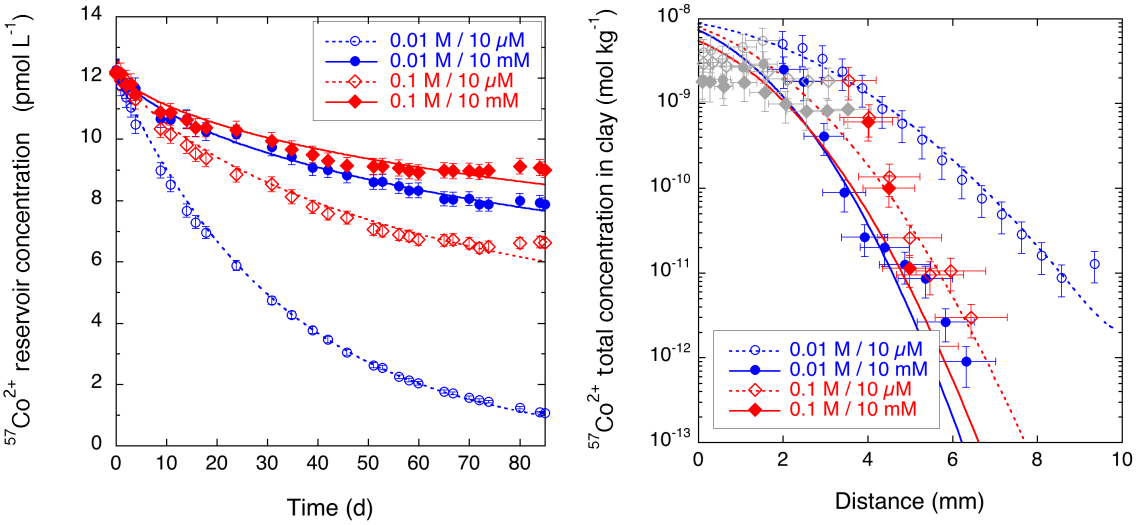

Fig. 4-4: Evolution of the upstream reservoir solution concentration of $^{57}Co^{2+}$ (left-hand plot) and the total $^{57}Co^{2+}$ concentration (per dry clay) in the clay segments (right-hand plot) in the experimental series 21001.TON at pH 7

Data not used for parameter fitting are depicted in grey. The first number in the legend indicates the concentration of NaCl, the second the one of $CaCl_2$.

4.1.3 Interpretation of the results in terms of an EDL sorption and diffusion model

The diffusion data described in section 4.1.2 are modelled using the 2SPNE SC/EDL model and the related parameters applied in Glaus et al. (2021), see also Tab. A-1 and Tab. A-2 in the Appendix. The results are shown in Fig. 4-5 to Fig. 4-8.

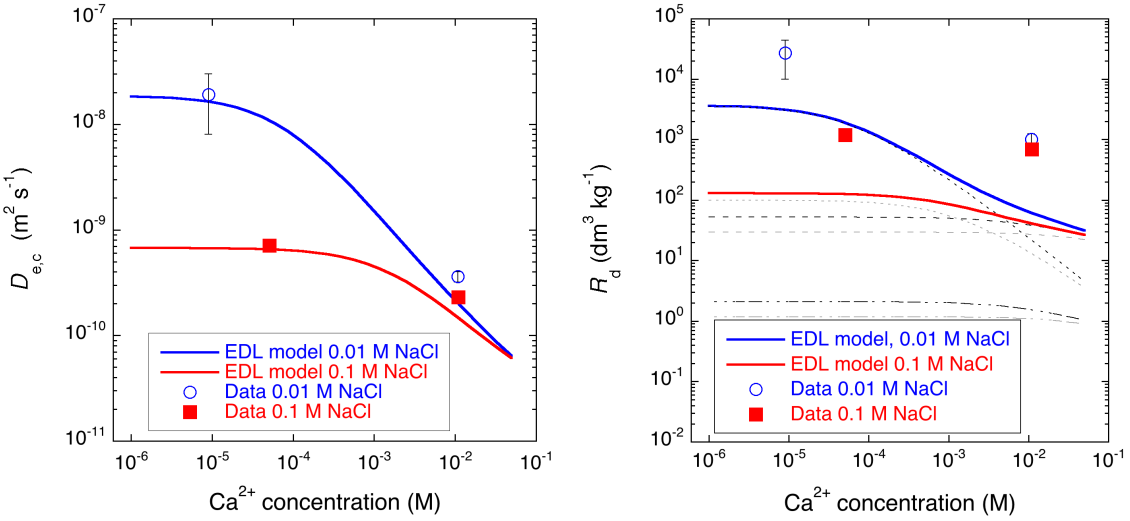

Fig. 4-5: Comparison between the best-fit parameter values obtained in experimental series 21001.TON at pH 4 with the simulations using the 2SPNE SC/EDL model

The black (0.01 M NaCl) and grey (0.1 M NaCl) lines in the right-hand plot show the contributions of EDL species (dotted), strong sites (dashed) and weak sites (dash-dotted) to the overall R_d value.

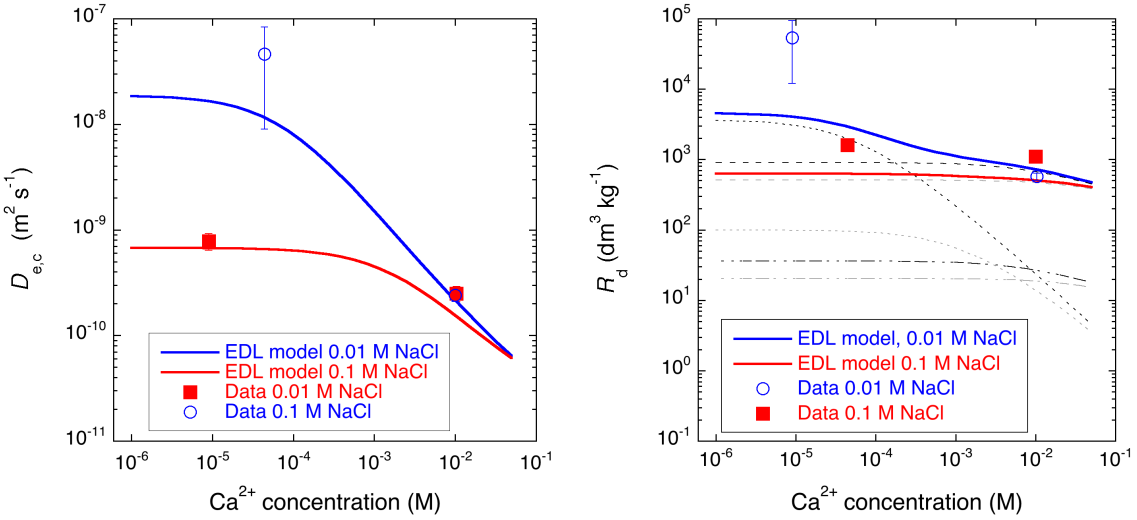

Fig. 4-6: Comparison between the best-fit parameter values obtained in experimental series 21001.TON at pH 5 with the simulations using the 2SPNE SC/EDL model

The black (0.01 M NaCl) and grey (0.1 M NaCl) lines in the right-hand plot show the contributions of EDL species (dotted), strong sites (dashed) and weak sites (dash-dotted) to the overall R_d value.

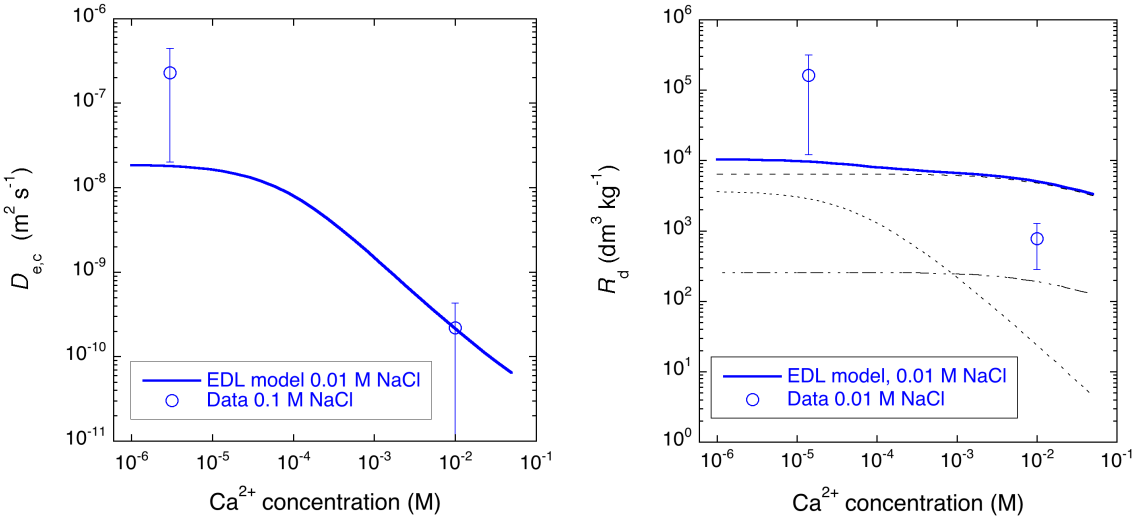

Fig. 4-7: Comparison between the best-fit parameter values obtained in experimental series 21001.TON at pH 6 with the simulations using the 2SPNE SC/EDL model

The black (0.01 M NaCl) and grey (0.1 M NaCl) lines in the right-hand plot show the contributions of EDL species (dotted), strong sites (dashed) and weak sites (dash-dotted) to the overall R_d value. Only results for 0.01 M NaCl are tentatively available, their uncertainties are only estimated. The discrepancy between model and data can therefore not be used to test the validity of the model, the purpose of these graphs is only illustrative.

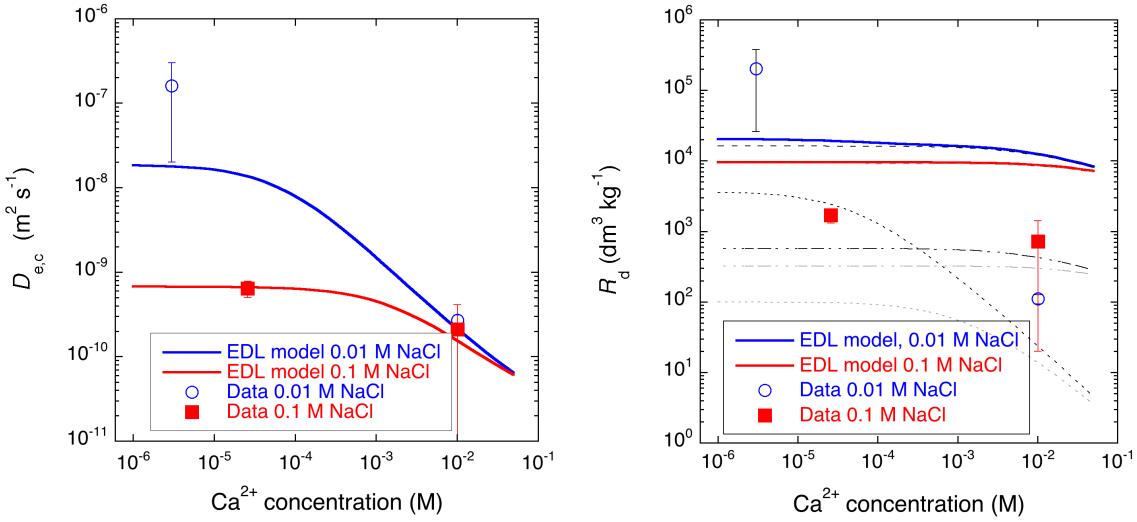

Fig. 4-8: Comparison between the best-fit parameter values obtained in experimental series 21001.TON at pH 7 with the simulations using the 2SPNE SC/EDL model

The black (0.01 M NaCl) and grey (0.1 M NaCl) lines in the right-hand plot show the contributions of EDL species (dotted), strong sites (dashed) and weak sites (dash-dotted) to the overall R_d value.

As can be seen from these plots, a satisfactory level of agreement was attained between the experimental data and the simulations, mostly in qualitative respect. A significant influence of the presence of Ca^{2+} on $D_{e,c}$ and R_d can be noted particularly for the lower ionic strength. The influence of R_d is not in contradiction to the conclusions of the experiments at 0.1 M (Glaus et al. 2021) because the importance of $^{57}Co^{2+}$ species at the planar surfaces increases with decreasing ionic strength. This can be seen from the black lines shown in the right-hand plots in which the EDL species (dotted lines) dominate sorption at low pH and low ionic strength, while the strong-site surface complexes (dashed lines) take over at higher pH values. Despite some discrepancies that persist in cases, and taking into account the experimental uncertainties and the partial failure of the experiments at pH 6 and 7, the general observations drawn from these experiments are consistent with the anticipated distribution of the various surface species with respect to pH and ionic strength.

4.2 Competition effects: Ca^{2+} on the diffusion of Eu^{3+} tracer

Competition effects between Ca^{2+} and Eu^{3+} regarding diffusion have not been explored in experiments, so far. Only effects regarding sorption are known. According to Marques Fernandes & Baeyens (2020), competition at the edge site surfaces between Eu^{3+} and Ca^{2+} is not expected to take place because of the different valence numbers and the different chemical behaviour of these cations, whereas for the planar surfaces, competition between the two metal cations was confirmed by time-resolved fluorescence measurements on montmorillonite (Rabung et al. 2005).

4.2.1 Overview of experimental conditions

All experiments were conducted as a function of the solution concentration of Ca^{2+} at a fixed concentration of Na^{+} at 0.1 M at pH 5 (experimental series 20004.TON) and pH 6 (experimental series 20005.TON) using $^{152}Eu^{3+}$ in a given background concentration of stable isotope Eu^{3+}. In contrast to the experiments with Co^{2+}, measurements were also performed using a pure Ca^{2+} system (only homoionic Ca-IdP, pure $CaCl_2$ solution).

Prior experience (Glaus et al. 2020) has already revealed that diffusion experiments with $^{152}Eu^{3+}$ tracer may be problematic at pH values larger or equal to 6. Presumably these problems are related to the formation of colloidal Eu^{3+} species upon release of phosphate from illite. For the present experiments, the illite underwent a more intensive acid pre-treatment than in earlier experiments and the amount of phosphate released from illite during the acid treatment was analytically monitored until levelling-off of the phosphate concentrations in the washing solutions. In the present experiments, no issues related to the formation of Eu^{3+} colloids could be spotted. A valuable indication of the involvement of colloidal species can be obtained from mass balances of concentration depletion in the upstream concentration reservoir solution and the tracer profile measured after diffusion. If colloids form, the solution concentrations measured by γ–counting decrease with time in centrifuged samples. However, owing to the formation of the colloids the solution concentration of mono-nuclear Eu^{3+} species strongly decreases leading to unexpected low amounts of Eu^{3+} in the clay. The mass balance for Eu^{3+} in the two phases is strongly disturbed in such cases. However, no such effects were observed in the present experiments. The results can thus be considered as fully valuable.

No comprehensive tests were performed to measure the equivalent fractional occupancy in these experiments since similar measurements were already carried out in previous experiments with $^{57}Co^{2+}$ tracer (Glaus et al. 2021). Only for the pure Ca^{2+} systems, such tests were performed. The results showed that the CEC was occupied at ≥ 95% by Ca^{2+} and to ~ 1% by Na^{+}. The results also showed that the CEC for Ca^{2+} was identical to the one for Na^{+} within the scope of analytical uncertainty. Extended extractions with $CsNO_3$ were made for the experiments carried out at pH 6. The results are shown in Fig. 4-9. These results appear consistent with the previous tests for the samples at pH 5 (Glaus et al. 2021) without any significant discrepancies.

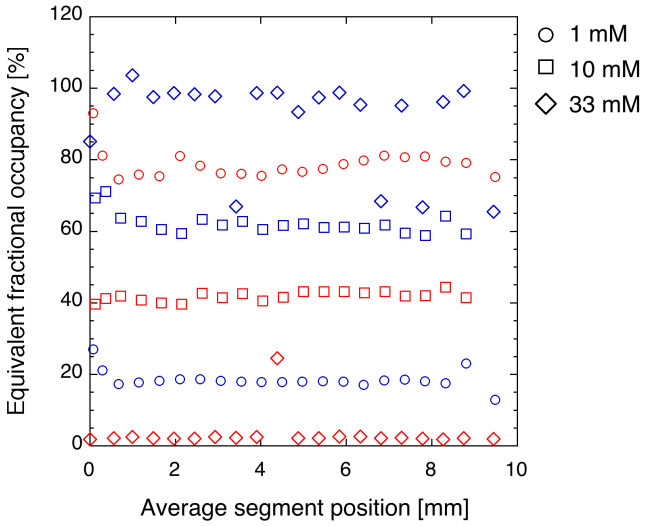

Fig. 4-9: Equivalent fractional occupancy of the illite planar surfaces with Na^{+} (red) and Ca^{2+} (blue) measured in the clay segments of experimental series 20005.TON (pH 6) by extraction with Cs^{+}

The legend indicates the target concentration of Ca^{2+} in the contacting electrolyte solutions used for in-diffusion of $^{152}Eu^{3+}$. For the two largest concentration levels of Ca^{2+}, an incomplete recovery of Ca^{2+} was considered (92% for 10 mM and 90% for 33 mM Ca^{2+}) from the Cs^{+} extraction.

4.2.2 Results of in-diffusion tests and single-species modelling of experiments at pH 5

The results of the experiments are shown in Fig. 4-10 along with the results of the single-species inverse modelling. The best-fit parameter values are given in Tab. 4-2. As can be seen from the plots, the sorption behaviour in the pure Ca^{2+} system derives clearly from linear sorption (model curves assume linear sorption). The reason for this behaviour could not be clarified. Additional experiments would have to be carried out using lower concentrations of stable Eu^{3+} to test whether the non-linear behaviour might be explained by different surface sites. Alternatively, the sharp fronting in the tracer profiles might also be explained by a change of aqueous speciation at low solution concentrations.

Tab. 4-2: Summary of experimental conditions and the best-fit parameter values and their uncertainties on a 95% confidence level as obtained from single-species diffusion simulations in Comsol Multiphysics® for the experimental series 20004.TON

Exp.	ρ_{bd} [a] [kg m^{-3}]	pH	Solution [a]		Solid [b]		$D_{e,c}$ [m^2 s^{-1}]	R_d [c] [m^3 kg^{-1}]	$D_{e,f}$ [m^2 s^{-1}]
			Na^+	Ca^{2+}	Na^+	Ca^{2+}			
1A	1'706	5	0.1	10^{-4}	0.95	0.05	$(1.7 \pm 0.4) \times 10^{-9}$	1.33 ± 0.3	2.5×10^{-10}
1B	1'705	5	0.1	10^{-4}	0.95	0.05	$(1.9 \pm 0.6) \times 10^{-9}$	1.54 ± 0.5	2.5×10^{-10}
2A	1'707	5	0.1	10^{-3}	0.74	0.26	$(1.5 \pm 0.3) \times 10^{-9}$	1.05 ± 0.2	2.5×10^{-10}
2B	1'703	5	0.1	10^{-3}	0.74	0.26	$(1.6 \pm 0.4) \times 10^{-9}$	1.04 ± 0.2	2.5×10^{-10}
3A	1'701	5	0.1	10^{-2}	0.38	0.62	$(6.2 \pm 0.5) \times 10^{-10}$	0.55 ± 0.06	2.5×10^{-10}
3B	1'700	5	0.1	10^{-2}	0.38	0.62	$(4.5 \pm 0.5) \times 10^{-10}$	0.40 ± 0.05	2.6×10^{-10}
4A	1'700	5	0	3.3×10^{-2}	0	1.0	$(2.8 \pm 0.4) \times 10^{-10}$	0.62 ± 0.1	2.8×10^{-10}
4B	1'704	5	0	3.3×10^{-2}	0	1.0	$(2.5 \pm 0.4) \times 10^{-10}$	0.67 ± 0.1	2.8×10^{-10}

[a] Solution concentrations in mol dm^{-3} (target values). The results of analytical measurements showed that the true values did not deviate substantially (± 10% on the average) from these values.

[b] Mass fractions of Na^+ and Ca^{2+} at the planar surfaces, as set by the mass fractions of Na-IdP and Ca-IdP initially added in the preparation of the clay samples. Post mortem Cs^+ extraction of the clay samples from experiment 20003.TON showed that these mass fractions remained rather constant during the experiment and that a reasonable homogenisation of the samples were reached during the saturation and diffusion phase.

[c] Assumption of linear sorption which was fully applicable for the measurements 1A to 3B. However, 4A and 4B showed substantial deviation from linear sorption.

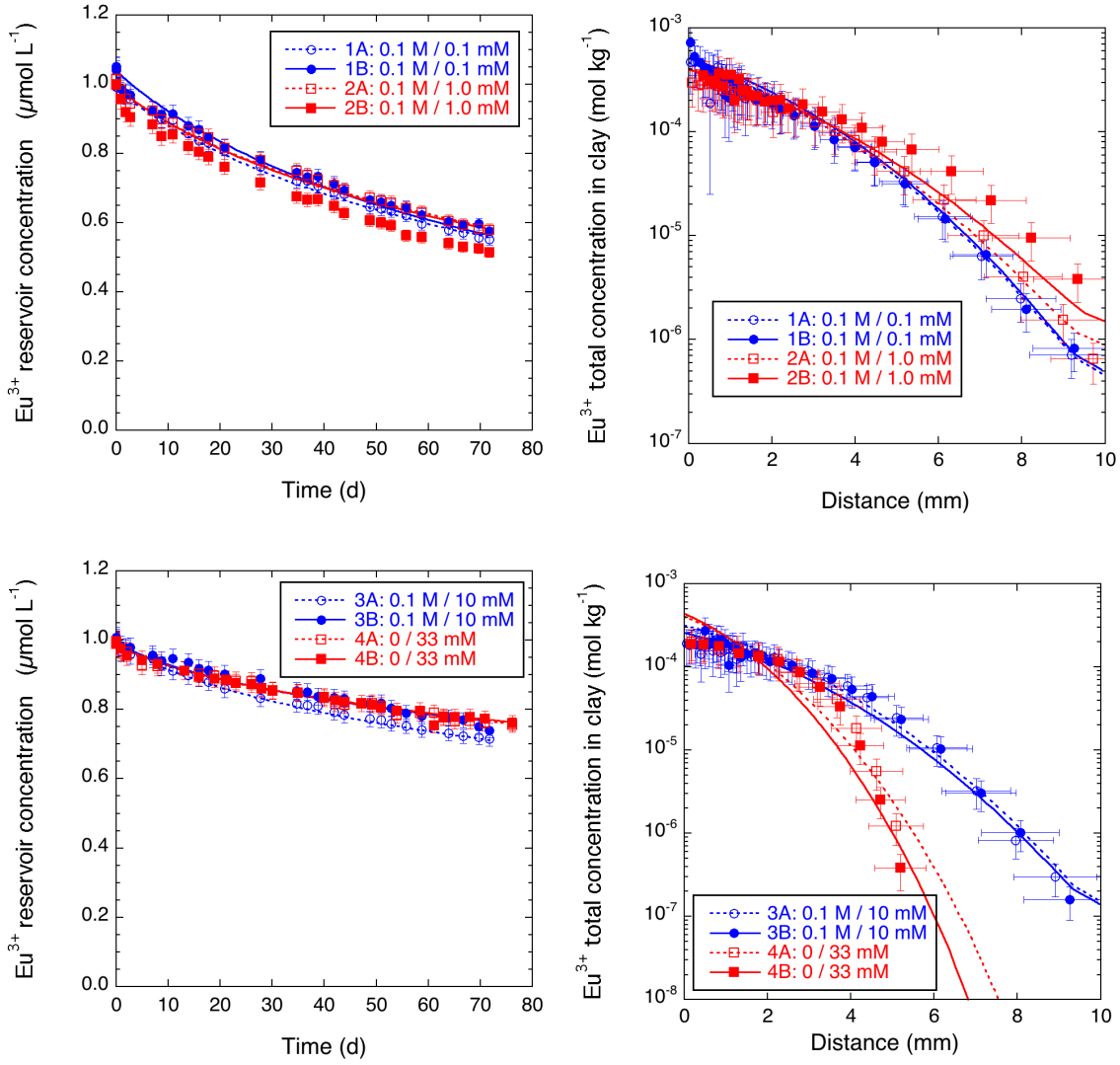

Fig. 4-10: Evolution of the upstream reservoir solution concentration of Eu^{3+} (left-hand plots) and the total Eu^{3+} concentration (per dry clay) in the clay segments (right-hand plots) in the experimental series 20004.TON at pH 5

The first number in the legend indicates the concentration of NaCl, the second the one of $CaCl_2$.

4.2.3 Results of in-diffusion tests and single-species modelling of experiments pH 6

The results of the experiments are shown in Fig. 4-11 along with the results of the single-species inverse modelling. The best-fit parameter values are given in Tab. 4-3. As for the results obtained for pH 5, the sorption behaviour in the pure Ca^{2+} system derives from linear sorption (model curves assume linear sorption), but the discrepancy is slightly less. Two experiments in this series (1A and B) failed because of a rupture of the membrane. However, this was not a serious issue because these experiments were at the lowest concentrations of Ca^{2+} where almost no effect on $D_{e,c}$ and R_d was expected.

Tab. 4-3: Summary of experimental conditions and the best-fit parameter values and their uncertainties on a 95% confidence level as obtained from single-species diffusion simulations in Comsol Multiphysics® for the experimental series 20005.TON

Exp.	ρ_{bd} [a] [kg m^{-3}]	pH	Solution [a]		Solid [b]		$D_{e,c}$ [m^2 s^{-1}]	R_d [c] [m^3 kg^{-1}]	$D_{e,f}$ [m^2 s^{-1}]
			Na^+	Ca^{2+}	Na^+	Ca^{2+}			
2A	1'700	6	0.1	10^{-3}	0.74	0.26	$(1.9^{+2.3}_{-0.6}) \times 10^{-9}$	$3.3^{+3.6}_{-1.0}$	2.5×10^{-10}
2B	1'704	6	0.1	10^{-3}	0.74	0.26	$(2.7^{+1.4}_{-1.0}) \times 10^{-9}$	$4.7^{+2.4}_{-1.7}$	2.5×10^{-10}
3A	1'703	6	0.1	10^{-2}	0.38	0.62	$(7.8 \pm 1.2) \times 10^{-10}$	2.6 ± 0.5	2.5×10^{-10}
3B	1'705	6	0.1	10^{-2}	0.38	0.62	$(7.1 \pm 1.5) \times 10^{-10}$	2.7 ± 0.5	2.6×10^{-10}
4A	1'706	6	0	3.3×10^{-2}	0	1.0	$(3.5 \pm 0.5) \times 10^{-10}$	2.4 ± 0.4	2.8×10^{-10}
4B	1'703	6	0	3.3×10^{-2}	0	1.0	$(2.8 \pm 0.4) \times 10^{-10}$	2.3 ± 0.3	2.8×10^{-10}

[a] Solution concentrations in mol dm^{-3} (target values). The results of analytical measurements showed that the true values did not deviate substantially (± 10% on the average) from these values.

[b] Mass fractions of Na^+ and Ca^{2+} at the planar surfaces, as set by the mass fractions of Na-IdP and Ca-IdP initially added in the preparation of the clay samples. Post mortem Cs^+ extraction of the clay samples from experiment 20003.TON showed that these mass fractions remained rather constant during the experiment and that a reasonable homogenisation of the samples were reached during the saturation and diffusion phase.

[c] Assumption of linear sorption which was fully applicable for the measurements 2A to 3B. However, 4A and 4B showed substantial deviation from linear sorption.

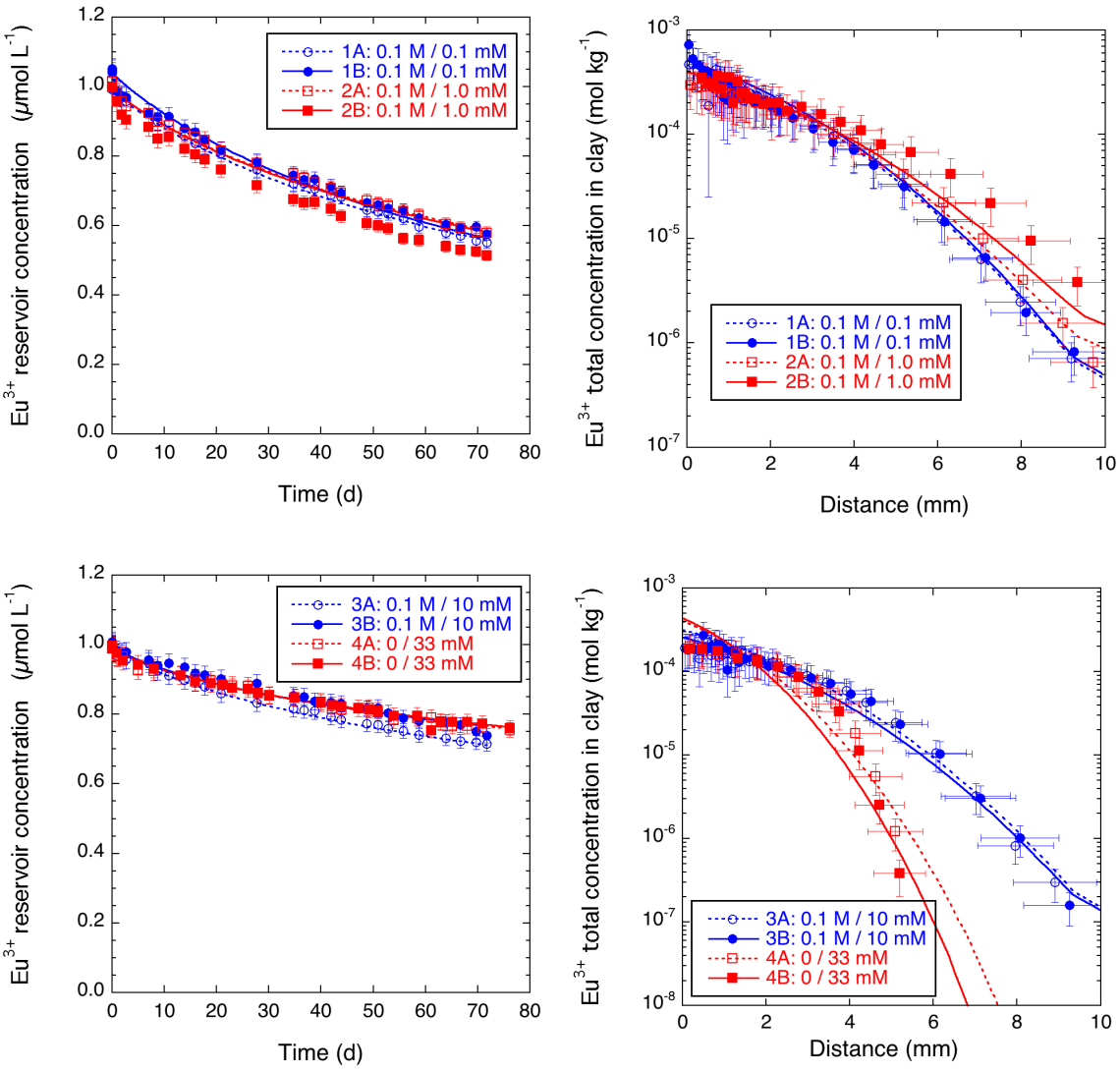

Fig. 4-11: Evolution of the upstream reservoir solution concentration of $^{152}Eu^{3+}$ (left-hand plots) and total $^{152}Eu^{3+}$ concentration (per dry clay) in the clay segments (right-hand plots) in the experimental series 20005.TON at pH 6

The first number in the legend indicates the concentration of NaCl, the second the one of $CaCl_2$.

4.2.4 Interpretation of the results in terms of an EDL sorption and diffusion model

The diffusion data described are modelled using the 2SPNE SC/EDL model and the related thermodynamic parameters applied in Glaus et al. (2020), see also Tab. A-1 and Tab. A-2 in the Appendix. The results are shown in Fig. Fig. 4-12 and Fig. 4-13. The Phreeqc specific input parameters are given in Tab. 4-4. They are identical for pH 5 and 6. Except for the value for q_η which was increased from 0.2 to 0.4 to better match the experimental data, all other parameters were left at their default values. In that sense, the model curves in Fig. 4-12 and Fig. 4-13 can be regarded as a 'near-blind' prediction. The model calculations are done for a constant background concentration of 0.1 M Na^+ throughout which is not fully applicable for the systems with the pure Ca form of illite (experiments 4A and 4B). However, the resulting changes in the model curves are rather minor: The $D_{e,c}$ for a calculation without Na^+ is 1.6×10^{-10} $m^2\,s^{-1}$ (instead of 1.1×10^{-10} $m^2\,s^{-1}$) and the R_d 1'300 $dm^3\,kg^{-1}$ (instead of 920 $dm^3\,kg^{-1}$).

The right-hand plots of Fig. 4-12 and Fig. 4-13 illustrate why Ca^{2+} has a stronger impact on $D_{e,c}$ than on R_d. Sorption is dominated by planar surface species at low Ca^{2+} concentrations at pH 5. With increasing Ca^{2+} concentration, the strong sites take over because they are not affected by competition effects with Ca^{2+}. Sorption changes thus only moderately according to the respective slight decrease of R_d values. In contrast, diffusion is dominated by Eu^{3+} species in the diffuse layer, which are subject to competition with Ca^{2+}. For this reason, $D_{e,c}$ values decrease with increasing Ca^{2+} concentration. The situation at pH 6 is similar, with the difference that weak site species dominate sorption across the entire range of Ca^{2+} concentrations. The changes of R_d values with varying Ca^{2+} concentration is thus even less than at pH 5.

Tab. 4-4: Overview of parameter values used for the calculation of $D_{e,c}$ and R_d using the 2SPNE SC/EDL model for the diffusion for the diffusion experiments with $^{152}Eu^{3+}$ at pH 5 and 6

Variable	Value	Units	Explanation
por_clay	0.392	-	Total water-accessible porosity (ρ_{bd} 1'703 kg m^{-3})
rho_b_eps	4.347	kg L^{-1}	Clay mass per pore volume
f_free	0.346	-	Fraction of free pore water (cf eq. 3)
f_DL	0.654	-	Fraction of water in the Donnan layer (cf eq. 3)
pore_r	4.60	nm	Radius of cylindrical pore
I	0.103	mol L^{-1}	Ionic strength
d_DL	1.51	nm	Thickness of Donnan layer
A_por	4.35E+05	m^2 L^{-1}	Specific external clay surface
Asu_	0.825	equiv	Amount of planar sites per clay cell
Sill_wa	0.174	equiv	Amount of type II sites per clay cell
Sill_s	8.68E-03	equiv	Amount of FES sites per clay cell
V_water	1.0	L	Volume of total water per clay cell
V_free	0.346	L	Volume of free pore water per clay cell
V_DL	0.654	L	Volume of Donnan layer per clay cell
$D_{w\text{-}Eu}$	6.1E-10	$m^2\,s^{-1}$	Diffusion of Eu^{3+} in bulk solution
q_η	0.4	-	Viscosity factor
tort_n	-2.239	-	Tortuosity exp. (corresponds $D_{e,c}$ 1.08e-10 $m^2\,s^{-1}$)
G_clay	8.149	-	Geometry factor G

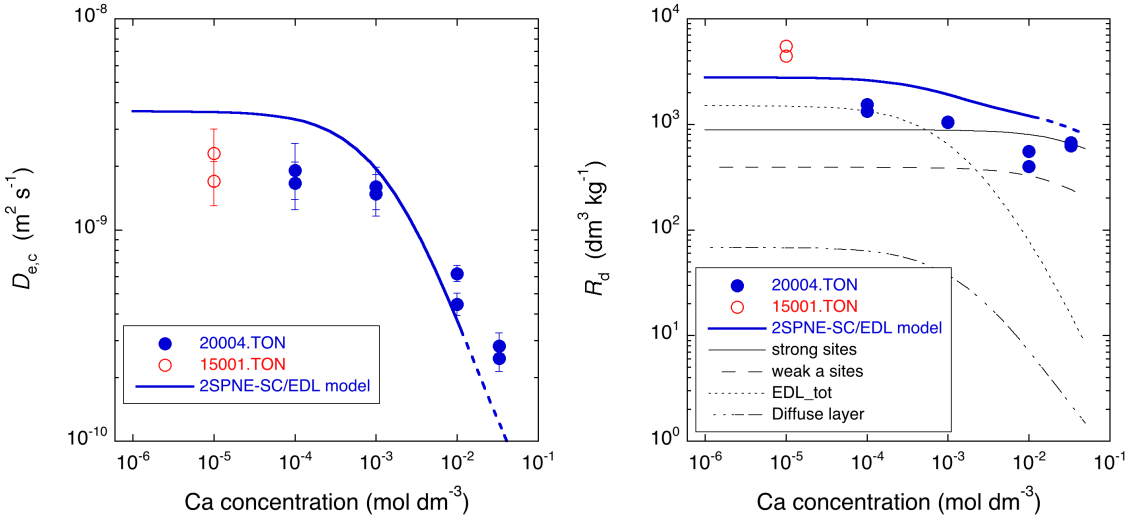

Fig. 4-12: Dependence of $D_{e,c}$ (left-hand plot) and R_d (right-hand plot) on the concentration of Ca^{2+} in the contacting electrolyte solution for the experiments at pH 5

The right-hand plot shows the total R_d value (blue line) along with the contribution of the individual surface sites (black lines). The results from experiment 15001.TON were published in Glaus et al. (2020). The dashed blue line indicates that the model calculations are only approximately comparable to the experimental conditions (see the additional explanations in the main text).

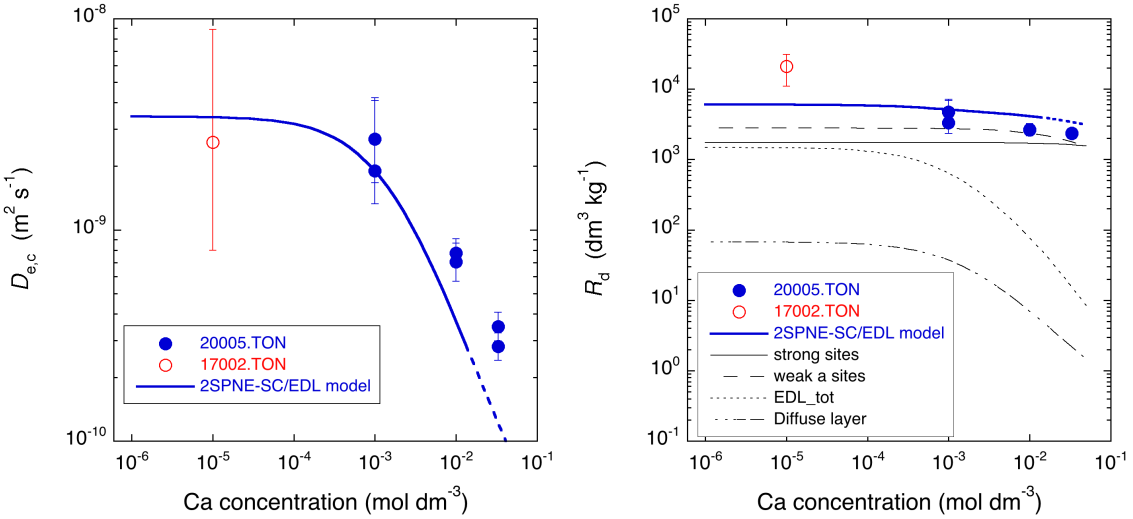

Fig. 4-13: Dependence of $D_{e,c}$ (left-hand plot) and R_d (right-hand plot) on the concentration of Ca^{2+} in the contacting electrolyte solution for the experiments at pH 6

The right-hand plot shows the total R_d value (blue line) along with the contribution of the individual surface sites (black lines). The results from experiment 17002.TON were published in Glaus et al. (2020). The dashed blue line indicates that the model calculations are only approximately comparable to the experimental conditions (see the additional explanations in the main text).

4.3 Competition effects: Ca^{2+} on the diffusion of Mn^{2+} tracer

4.3.1 Overview of experimental conditions

The experiments with $^{54}Mn^{2+}$ tracer were carried out in analogy to those with $^{57}Co^{2+}$ tracer at pH 5 and a salinity of 0.1 M NaCl. The solution concentration of Ca^{2+} was varied between 0.1 mM and 33.3 mM whereby the illite form in the latter case was a pure Ca-IdP. For all other cases a pre-equilibrated fractional loading of mixed Na^+- and Ca^{2+}-IdP was used according to the solution concentrations of these cations before starting in-diffusion of the $^{54}Mn^{2+}$ tracer. The experimental conditions were thus analogous to those shown in Tab. 4-2.

4.3.2 Results of in-diffusion tests and single-species modelling

The results of the experiments are shown in Fig. 4-14 along with the results of the single-species inverse modelling. The best-fit parameter values are given in Tab. 4-5. Linear sorption was assumed in all cases. One experiment in this series (3B) failed because of a rupture of the membrane.

Tab. 4-5: Summary of experimental conditions and the best-fit parameter values and their uncertainties on a 95% confidence level as obtained from single-species diffusion simulations in Comsol Multiphysics® for the experimental series 20006.TON

Exp.	ρ_{bd} [a] [kg m^{-3}]	pH	Solution [a]		Solid [b]		$D_{e,c}$ [m^2 s^{-1}]	R_d [c] [m^3 kg^{-1}]	$D_{e,f}$ [m^2 s^{-1}]
			Na^+	Ca^{2+}	Na^+	Ca^{2+}			
1A	1'709	5.1	0.1	10^{-4}	0.95	0.05	$(6.4^{+1.1}_{-0.9}) \times 10^{-10}$	$0.64^{+0.11}_{-0.09}$	2.8×10^{-10}
1B	1'701	5.1	0.1	10^{-4}	0.95	0.05	$(5.8^{+0.8}_{-0.7}) \times 10^{-10}$	$0.57^{+0.07}_{-0.06}$	2.8×10^{-10}
2A	1'705	5.0	0.1	10^{-3}	0.74	0.26	$(4.9^{+0.7}_{-0.6}) \times 10^{-10}$	$0.67^{+0.09}_{-0.08}$	2.8×10^{-10}
2B	1'701	5.0	0.1	10^{-3}	0.74	0.26	$(4.6^{+0.5}_{-0.5}) \times 10^{-10}$	$0.55^{+0.06}_{-0.05}$	2.8×10^{-10}
3A	1'704	5.1	0.1	10^{-2}	0.38	0.62	$(2.3^{+0.3}_{-0.2}) \times 10^{-10}$	$0.45^{+0.06}_{-0.05}$	2.8×10^{-10}
4A	1'704	5.1	0	3.3×10^{-2}	0	1.0	$(1.3^{+0.1}_{-0.1}) \times 10^{-10}$	$0.43^{+0.05}_{-0.04}$	2.8×10^{-10}
4B	1'704	5.0	0	3.3×10^{-2}	0	1.0	$(1.1^{+0.09}_{-0.08}) \times 10^{-10}$	$0.44^{+0.04}_{-0.03}$	2.8×10^{-10}

[a] Solution concentrations in mol dm^{-3} (target values). The results of analytical measurements showed that the true values did not deviate substantially (± 10% on the average) from these values.

[b] Mass fractions of Na^+ and Ca^{2+} at the planar surfaces, as set by the mass fractions of Na-IdP and Ca-IdP initially added in the preparation of the clay samples. Post mortem Cs^+ extraction of the clay samples from experiment 20003.TON showed that these mass fractions remained rather constant during the experiment and that a reasonable homogenisation of the samples were reached during the saturation and diffusion phase.

[c] Assumption of linear sorption which was applicable for all measurements.

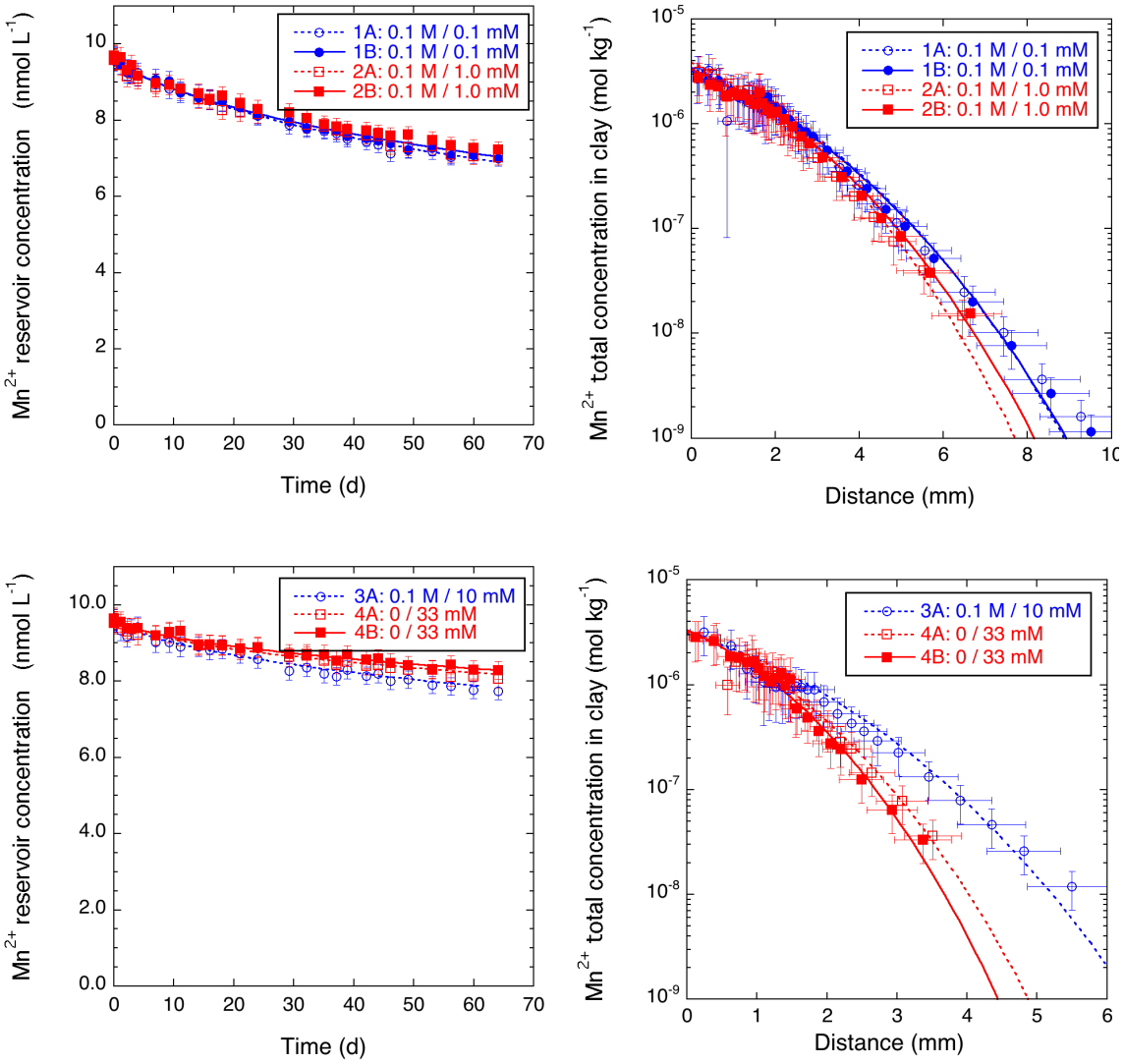

Fig. 4-14: Evolution of the upstream reservoir solution concentration of Mn^{2+} (left-hand plots) and total Mn^{2+} concentration (per dry clay) in the clay segments (right-hand plots) in the experimental series 20006.TON at pH 5

The first number in the legend indicates the concentration of NaCl, the second the one of $CaCl_2$.

4.3.3 Interpretation of the results in terms of an EDL sorption and diffusion model

The diffusion data are modelled using the 2SPNE SC/EDL model and the related thermodynamic parameters provided in Tab. 4-3 (Section 4.2.3), see also Tab. A-1 and Tab. A-2 in the Appendix. The results are shown in Fig. 4-15. The Phreeqc specific input parameters are given in Tab. 4-6. Except for the value for q_η which was increased from 0.4 to 0.8 to better match the experimental data, all other parameters were left at their default values. In that sense, the model curves in Fig. 4-15 can be regarded as a "near-blind" prediction. The model calculations are done for a constant background concentration of 0.1 M Na^+ throughout which is not fully applicable for the systems with the pure Ca form of illite (experiments 4A and 4B). Similar to the case of Eu^{3+}, the resulting changes in the model curves are rather minor.

Also, in the case of Mn^{2+} tracer diffusion, Ca^{2+} has a stronger impact on $D_{e,c}$ than on R_d. One may note a factor of ~ 5 between the $D_{e,c}$ values for the highest and the lowest Ca^{2+} concentration, while this factor is only ~ 1.4 for the respective R_d values. Sorption is dominated by edge site surface complexes at all Ca^{2+} concentrations. Although the weak sites of type *x* must be regarded as a rather operational property of the clay in order to be able to fit sorption data at pH 5, the contribution of the planar sites is also much less compared to the strong sites. The contribution of planar surface species decreases with increasing Ca^{2+} concentration. This explains the decrease of $D_{e,c}$ values at Ca^{2+} concentrations > 0.1 mM.

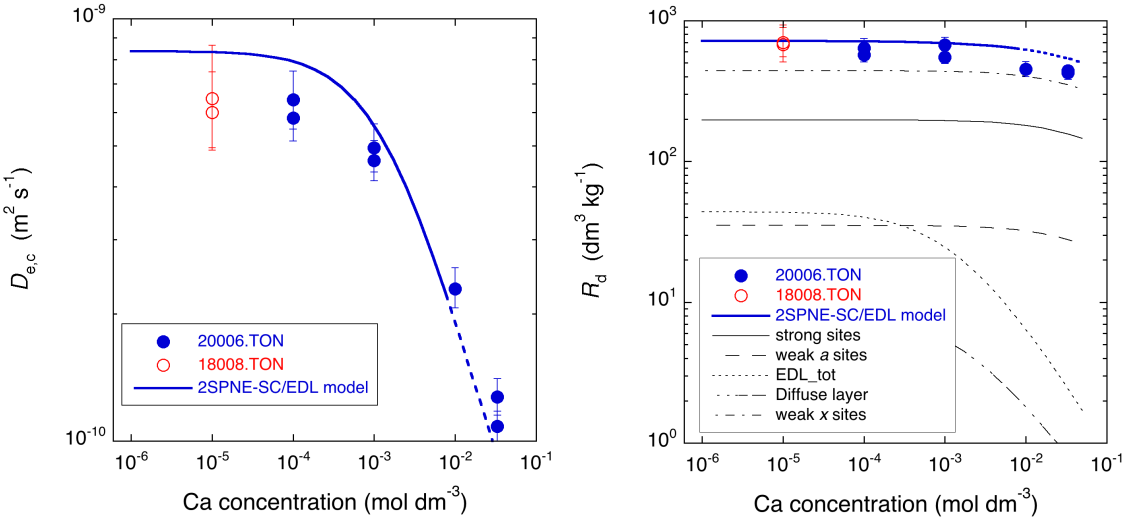

Fig. 4-15: Dependence of $D_{e,c}$ (left-hand plot) and R_d (right-hand plot) on the concentration of Ca^{2+} in the contacting electrolyte solution for the experiments with $^{54}Mn^{2+}$ tracer

The right-hand plot shows the total R_d value (blue line) along with the contribution of the individual surface sites (black lines). The results from experiment 18008.TON are available in Section 4.2. The dashed blue line indicates that the model calculations are only approximately comparable to the experimental conditions (see the additional explanations in the main text).

Tab. 4-6: Overview of parameter values used for the calculation of $D_{e,c}$ and R_d using the 2SPNE SC/EDL model for the diffusion for the diffusion experiments with $^{54}Mn^{2+}$ at pH 5

Variable	**Value**	**Units**	**Explanation**
por_clay	0.391	-	Total water-accessible porosity (ρ_{bd} 1'704 kg m^{-3})
rho_b_eps	4.353	kg L^{-1}	Clay mass per pore volume
f_free	0.338	-	Fraction of free pore water (cf eq. 3)
f_DL	0.662	-	Fraction of water in the Donnan layer (cf eq. 2)
pore_r	4.59	nm	Radius of cylindrical pore
I	0.100	mol L^{-1}	Ionic strength
d_DL	1.52	nm	Thickness of Donnan layer
A_por	4.35E+05	m^2 L^{-1}	Volumetric external clay surface
Asu_	0.827	equiv	Amount of planar sites
Sill_wa	0.174	Equiv	Amount of weak sites type *a*
Still_wx	2.18E-03		Amount of weak sites type *x*
Sill_s	8.68E-03	equiv	Amount of strong sites
V_water	1.0	L	Volume of total water
V_free	0.338	L	Volume of free pore water
V_DL	0.662	L	Volume of Donnan layer
$D_{w\text{-}Eu}$	6.8E-10	m^2 s^{-1}	Diffusion of Mn^{2+} in bulk solution
q_η	0.8	-	Viscosity factor
tort_n	-2.364	-	Tortuosity exponent
G_clay	9.53	-	Geometry factor *G*
D*w_HTO*	9.5E-11	m^2 s^{-1}	Effective diffusivity of water

4.4 Competition effects: Mn^{2+} on the diffusion of Co^{2+} tracer

4.4.1 Overview of experimental conditions

In this experiment, the cation competing with the trace $^{57}Co^{2+}$ is a representative of the transition metal series which is different from the previous experiments where alkaline earth cations were used as competitors. The sorption properties of $^{57}Co^{2+}$ tracer are thus expected to be much stronger affected than in the case of competition with Ca^{2+}. For this reason, the focus of parameter variation in these series was different compared to the experiments described in Sections 4.1 to 4.3. In the present experiments, pH was varied between 4 and 7, and the Mn^{2+} concentrations were chosen such as to produce two different loadings of the clay edge surfaces: (i) saturation of the strong sites only and (ii) saturation of both weak and strong sites.

To this end, the conditioning of the illite necessitated the production of different clay forms involving various ratios of a mixed Na^+/Mn^{2+} form of the clay surface at the desired pH values in batch equilibration experiments. After equilibrating the clay with appropriate electrolytes containing Na^+ and Mn^{2+}, the clay was separated from the electrolyte solution by centrifugation and then freeze-dried. The concentrations of Mn^{2+} in the equilibrated solutions were measured by high-performance cation exchange chromatography on an Ionpac CS5a column. Detection of the analytes was performed using colorimetry with a UV-VIS detector after post-column derivatisation by the addition of a 4-(2-pyridylazo)resorcinol (PAR) containing reagent (details are given in section 9.4.1 of the Appendix). Tab. 4-7 gives an overview of the experimental conditions to produce such clays for the experimental series 21003.TON. The preparation was repeated twice with the same results.

Tab. 4-7: Preparation of mixed forms of Na^+/Mn^{2+}-IdP for experimental series 21003.TON

All concentrations refer to a solid:liquid ratio of 2 g of dry clay to 35 ml of electrolyte solution. 0.1 M NaCl was present in all solutions.

Exp.	pH	Buffer [a]	Sites saturation	$[Mn^{2+}]_{in}$ [b] [M]	$[Mn^{2+}]_{eq\text{-}calc}$ [c] [M]	$[Mn^{2+}]_{eq\text{-}meas}$ [d] [M]
4H	4.0	Acetate	Weak + strong	0.104	0.100	0.099
5H	5.0	MES	Weak + strong	0.013	0.010	0.011
6H	6.0	MES	Weak + strong	4.3×10^{-3}	2.3×10^{-3}	2.3×10^{-3}
7H	7.0	MOPS	Weak + strong	3.6×10^{-3}	1.6×10^{-3}	2.5×10^{-3}
4L	4.0	Acetate	Strong	1.6×10^{-3}	1.0×10^{-3}	8.6×10^{-4}
5L	5.0	MES	Strong	4.4×10^{-4}	1.9×10^{-4}	1.7×10^{-4}
6L	6.0	MES	Strong	4.3×10^{-4}	1.3×10^{-4}	1.2×10^{-4}
7L	7.0	MOPS	Strong	3.9×10^{-4}	8.0×10^{-5}	9.7×10^{-5}

[a] Added at a concentration of 2 mM
[b] Added concentration (target value)
[c] Equilibrium concentration expected from equilibrium sorption calculations
[d] Equilibrium concentration measured

In all steps of clay preparation and analytics, working in a N_2-glove box (clay preparation) prevented the contact with oxygen. The respective precautions are described in the first paragraphs of Section A.4 of the Appendix. Fig. 4-16 illustrates the effect of air-borne oxygen on the stability of Mn^{2+} in homogeneous solutions buffered to the target values of the present experiments (4 – 7). As can be expected the oxidation of Mn^{2+} proceeds much faster at higher pH, illustrating thus the necessity to avoid the presence of oxygen in the experiments.

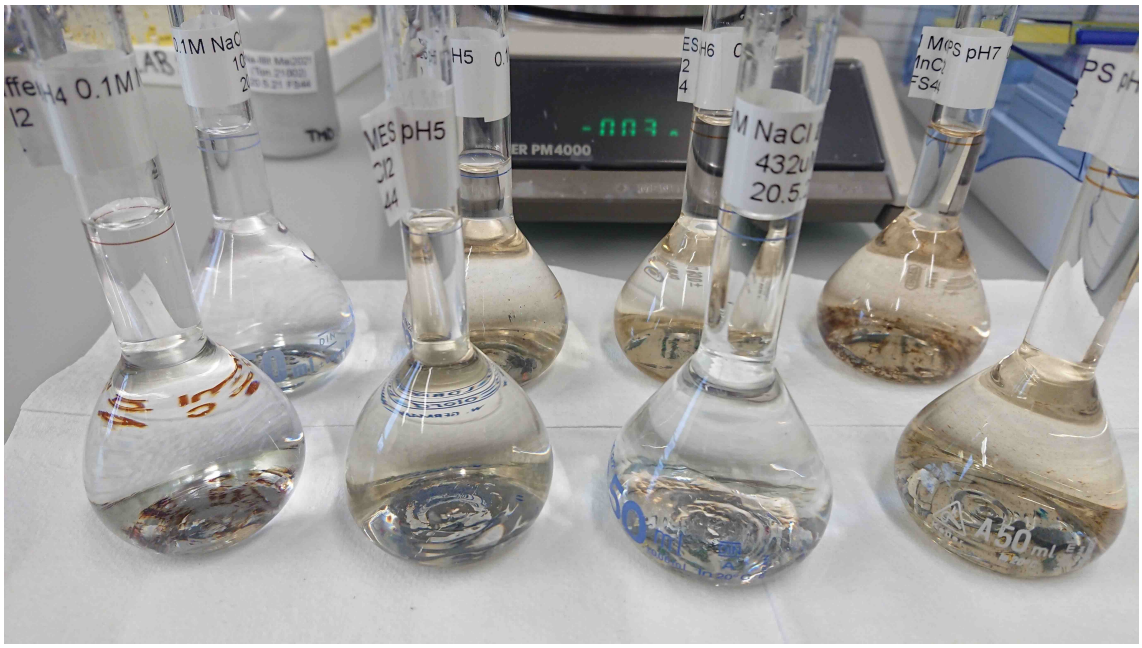

Fig. 4-16: Influence of pH on the oxidation of Mn^{2+} by air-borne oxygen, ~ 5 days after preparation of the solutions

pH varied from left to right from pH 4 to 7. The formation of a brown precipitate indicates the oxidation of Mn^{2+} to sparingly soluble Mn(IV) phases.

Subsequently, the freeze-dried clay samples were compacted in the membrane-confined diffusion cells and equilibrated with electrolyte solutions containing appropriate equilibrium concentrations of Mn^{2+} in a constant background concentration of 0.1 M NaCl. Because this step was also performed in the N_2 glove box, the exact geometry of the clay samples is less well defined compared to samples prepared outside the glove box.

For the saturation of the clay samples at pH 4 and pH 5 no solution exchange was performed while solutions were exchanged three times in the case of pH 6 and 7 to better obtain the desired surface loading with Mn^{2+}. Tab. 4-8 provides an overview of the solution exchanges and the analytical results for Mn^{2+} measured during the saturation phase and after the in-diffusion of $^{57}Co^{2+}$. The results indicate a certain uptake of Mn^{2+} by the clay samples at pH 6 and 7. This is, however, restricted to the samples in which the strong sites were preferentially loaded with Mn^{2+}. The overall picture suggests that the systems were well equilibrated.

Tab. 4-8: Concentrations[a] of Mn^{2+} measured by ion chromatography in the solutions during the saturation phase of the clay samples and after the in-diffusion of $^{57}Co^{2+}$

Exp.	pH	1st week	2nd week	4th week	After diffusion [b]
4H	4.0	-	-	0.090/0.099	0.092 (5 d)
5H	5.0	-	-	9.0 / 9.7 × 10^{-3}	1.0 × 10^{-2} (9 d)
6H	6.0	1.4 / 1.4 × 10^{-3}	1.4 / 1.4 × 10^{-3}	- [c]	- [c]
7H	7.0	9.5 / 10.0 × 10^{-4}	9.7 / 10 × 10^{-4}	9.7 / 9.5 × 10^{-4}	9.5 × 10^{-4} (24 d)
4L	4.0	-	-	9.1 / 9.8 × 10^{-4}	1.0 × 10^{-3} (24 d)
5L	5.0	-	-	1.0 / 1.0 × 10^{-4}	1.0 × 10^{-4} (24 d)
6L	6.0	2.6 / 2.4 × 10^{-5}	2.5 / 3.1 × 10^{-5}	2.5 / 1.9 × 10^{-5}	2.2 × 10^{-5} (27 d)
7L	7.0	7.1 / 16 × 10^{-6}	1.6 / 2.1 × 10^{-5}	1.1 / 0.9 × 10^{-5}	1.1 × 10^{-5} (46 d)

[a] The figure before the slash indicates the initial concentration, the figure after the slash the concentration measured after equilibration. In the last column, only the final concentration of Mn^{2+} after the in-diffusion phase is given. The initial concentration was chosen to be the target equilibrium concentration (cf. Tab. 4-7).

[b] Duration for in-diffusion of $^{57}Co^{2+}$ tracer given in parentheses.

[c] Experiment failure because of membrane rupture

4.4.2 Results of in-diffusion tests and single-species modelling

The results of the experiments are shown in Fig. 4-17 along with the results of the single-species inverse modelling. One experiment in this series (6H) failed because of a rupture of the membrane. The data shown in Fig. 4-17 produce a rather complex picture in which both $D_{e,c}$ and R_d show a distinct dependence on the variation of pH and the site loading with Mn^{2+}. A straightforward qualitative discussion of the parameter dependencies is almost impossible except for the comparison of the boundary concentrations at the clay/solution interface between the L- and H-experiments. It is rather obvious that the loading of both strong and weak sites (L-samples) leads to low R_d values compared with the samples in which only the strong sites are masked with Mn^{2+} (H-samples). The quantitative evaluation of the experimental data could be done also in this case by numerical single-species diffusion modelling. The best-fit parameter values are given in Tab. 4-9. Linear sorption was assumed in all cases.

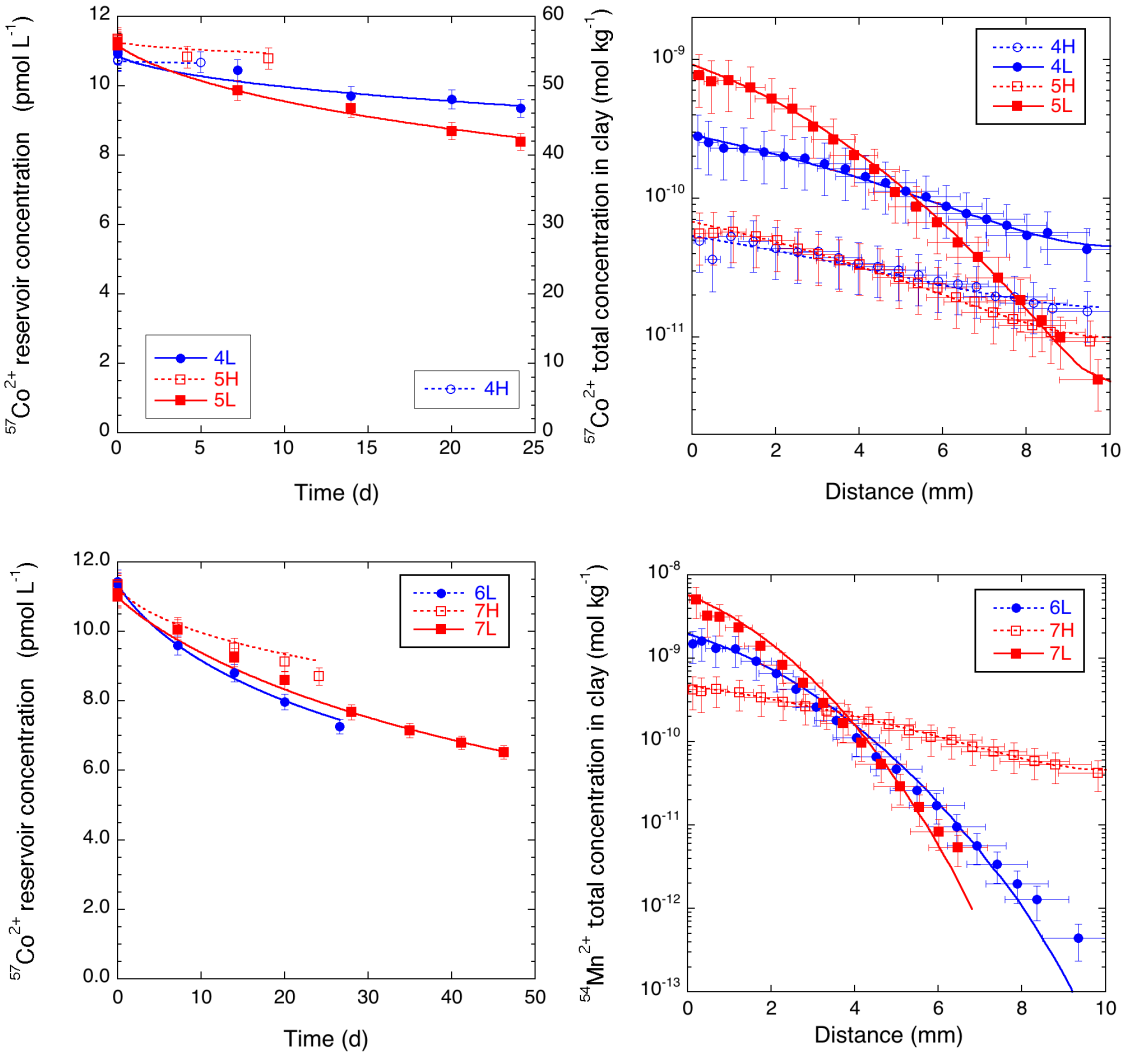

Fig. 4-17: Evolution of the upstream reservoir solution concentration of $^{57}Co^{2+}$ (left-hand plots) and total $^{57}Co^{2+}$ concentration (per dry clay) in the clay segments (right-hand plots) in the experimental series 21003.TON

The first number in the legend indicates the pH, the the extent of loading of the clay with Mn^{2+} (H for strong and weak sites loaded, L for strong sites loaded). The secondary y-axis in the upper left plot refers to the concentrations of 4H.

Tab. 4-9: Summary of experimental conditions and the best-fit parameter values and their uncertainties on a 95% confidence level as obtained from single-species diffusion simulations in Comsol Multiphysics® for the experimental series 21003.TON

Exp.	ρ_{bd} [a] [kg m^{-3}]	pH [a]	Saturation with Mn^{2+} [b] [%]		$D_{e,c}$ [m^2 s^{-1}]	R_d [c] [m^3 kg^{-1}]	$D_{e,f}$ [m^2 s^{-1}]
			Strong sites	Weak sites			
4H	1'707	4.0	100	77	$(1.05^{+0.09}_{-0.08}) \times 10^{-10}$	$(7.9^{+1.0}_{-0.8}) \times 10^{-4}$	2.8×10^{-10}
5H	1'704	5.0	100	89	$(2.4^{+0.17}_{-0.16}) \times 10^{-10}$	$(6.2^{+0.6}_{-0.5}) \times 10^{-3}$	2.8×10^{-10}
7H	1'707	7.0	100	93	$(6.5^{+0.9}_{-0.5}) \times 10^{-10}$	$(5.8^{+1.2}_{-0.8}) \times 10^{-2}$	2.8×10^{-10}
4L	1'705	4.0	84	6	$(4.7^{+0.43}_{-0.38}) \times 10^{-10}$	$(3.3^{+0.3}_{-0.3}) \times 10^{-2}$	2.8×10^{-10}
5L	1'702	5.0	91	10	$(6.2^{+0.7}_{-0.6}) \times 10^{-10}$	$0.13^{+0.014}_{-0.013}$	2.8×10^{-10}
6L	1'706	6.0	94	13	$(7.2^{+1.6}_{-1.3}) \times 10^{-10}$	$0.34^{+0.07}_{-0.06}$	2.8×10^{-10}
7L	1'700	7.0	95	15	$(1.04^{+0.33}_{-0.27}) \times 10^{-9}$	$1.4^{+0.4}_{-0.3}$	2.8×10^{-10}

[a] Measured in the initial solutions; it can safely be assumed that no significant shifts of pH occurred during the relatively short phase of in- diffusion.

[b] Speciation of Mn^{2+} at the edge surfaces calculated based on the thermodynamic data given in Tab. A-1 and Tab. A-2.

[c] Assumption of linear sorption which was applicable for all measurements.

4.4.3 Interpretation of the results in terms of an EDL sorption and diffusion model

For a speciation-based discussion of the results shown in Section 4.4.2, it is useful to provide a representation of the site occupancy by Mn^{2+} of the edge sites as a function of the solution concentration of Mn^{2+}. This can be done by classical sorption modelling via the 2SPNE SC/CE model or by the 2SPNE SC/EDL model. The latter model has been applied here using the parameters provided in Section 4.2.3. Owing to the equivalence of both model approaches regarding the behaviour of the edge sites, no significant differences between the two approaches can be expected. Fig. 4-18 shows the modelled surface speciation for Mn^{2+} for the strong- and the weak sites. The strong sites are saturated to almost 100% in the case of the H-series and to > 80% in the L-series. The weak sites are saturated to < 40% in the H-series and to < 5% in the L-series. This shows that a distinct occupation of the different sites could not be attained successfully under the conditions of the various experiments. The reason is that a different set of thermodynamic data was used in the planning phase of the experiments which overemphasised the importance of the weak sites. After correcting this constant, the saturation of the weak sites turned out to be lower than originally assumed. However, this in no way diminished the significance of the experiments.

Fig. 4-19 shows the best-fit parameter values for $D_{e,c}$ from the experiments and the model curves as a function of solution concentration of Mn^{2+}. The agreement between the measurements and the model is only fairly good. A significant discrepancy can be noted for the highest concentration of Mn^{2+}.

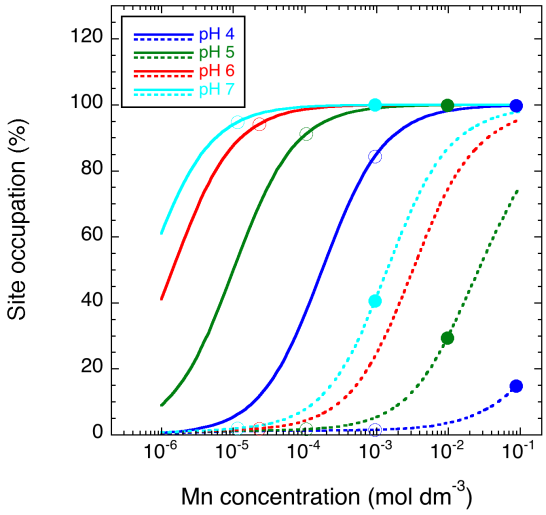

Fig. 4-18: Site occupation of Mn^{2+} at the edge surface sites calculated as a function of the solution concentration of Mn^{2+} for the various conditions applicable for the experiments 4L to 7L and 4H to 7H

The solid lines refer to the behaviour of the strong sites, the dotted to the one of the weak sites. The experimental conditions are represented by open and closed symbols, where the open symbols denote the conditions of the L-series and the closed symbols those of the H-series.

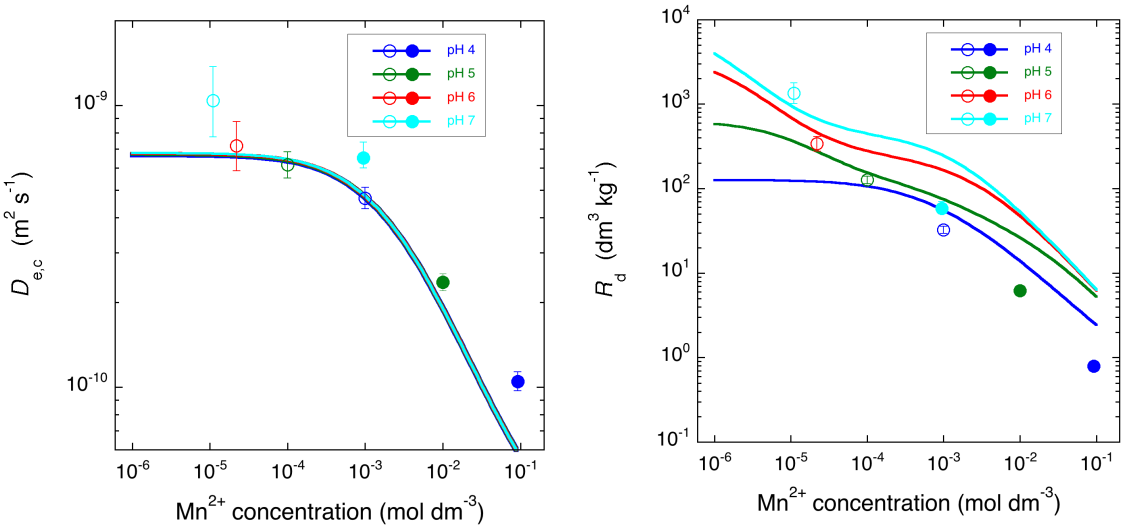

Fig. 4-19: Dependence of $D_{e,c}$ (left-hand plot) and R_d of $^{57}Co^{2+}$ tracer (right-hand plot) on the concentration of Mn^{2+} in the contacting electrolyte

Empty symbols represent the data for the L-series and full symbols those of the H-series.

Under these conditions, the dominance of Na^+ among the electrolyte cations is no longer obvious and the ionic strength deviates from 0.1 M. For these reasons, the representativity of these experimental data for the conditions applied in the modelling is not fully given. Further the robustness of the thermodynamic constant for the formation of Co^{2+} complexes with the weak sites is not beyond reasonable doubt. Lowering this constant by a factor of ~ 5 would significantly improve the agreement between the model curves and the experimental data. Despite these uncertainties, it may be noted that the data are fully compatible with the model trends from a qualitative point of view. With increasing Mn^{2+} concentration, $D_{e,c}$ values decrease at Mn^{2+} concentrations larger than ~ 1 mM. This can be explained by the competition between Mn^{2+} and Co^{2+} in the diffuse layer.

5 Effects of the presence of organic ligands on diffusion in compacted illite

5.1 Impact of oxalate on the diffusion properties of Eu(III)

5.1.1 Overview of experimental conditions

A dedicated series of in-diffusion experiments was carried out in the presence of 1 mM of oxalate. In these experiments, pH was varied between 4 and 8, while the background concentration of NaCl was kept at 0.03 M. All experiments were carried out in the absence of stable Eu(III) except for the amount present in the tracer solution. The results of these experiments were not published in Glaus et al. (2020), but only reported in a technical report (Glaus 2018). The main results are reiterated in the following section to ensure completeness.

5.1.2 Results and single-species modelling and interpretation of the results in terms of an EDL sorption and diffusion model

Oxalate forms strong complexes with the divalent and trivalent metal cations present in the experiments (Sekine 1964). Owing to the particularly strong complexation constants for Eu(III) complexes, it is expected that oxalate will have a strong influence on both the diffusion and sorption properties of Eu(III). The expectation was confirmed by the results shown in Fig. 5-1. In this plot, the results ($D_{e,c}$ and R_d) obtained as best-fit parameter values from the single-species transport model in Comsol Multiphysics®, are compared with the $D_{e,c}$ and R_d values calculated from the 2SPNE SC/EDL model. For simplicity, the presence of oxalate complexes of Al(III) was ignored in the latter model to avoid issues with dissolution of gibbsite. A further assumption for the Phreeqc model calculations was that the solution concentration of oxalate decreased by a factor of 10 owing to uptake of oxalate by illite. In view of the situation that no such sorption data exist, a couple of batch sorption tests were carried out at low solid:liquid ratios in the pertinent range of pH and background electrolyte concentration. These measurements confirmed that the model assumption is of the correct order of magnitude.

As can be seen from the results in Fig. 5-1, $D_{e,c}$ values decreased by ~ 2 orders of magnitude, which can be explained by a strong impact of oxalate on the distribution of Eu(III) between the diffuse layer and the free aqueous phase. Although the model curves are not exactly matching the experimental data, the observed trends are correctly predicted from a qualitative point. In view of the many competitors for oxalate present in the experimental system (such as Ca^{2+}, Mg^{2+} and Al^{3+}), the model predictions have a relatively high level of uncertainty.

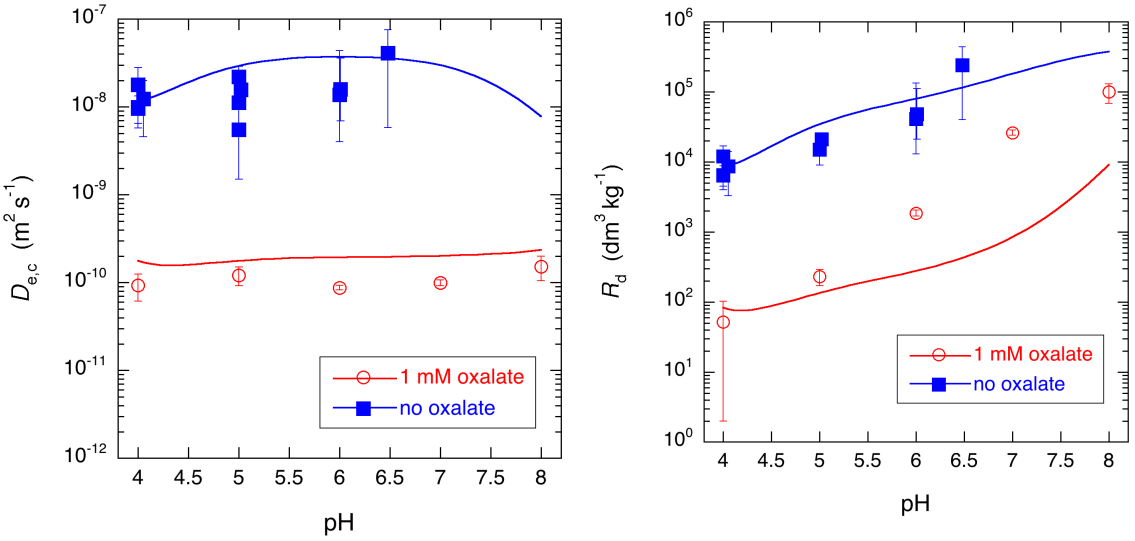

Fig. 5-1: Dependence of $D_{e,c}$ (left-hand plot) and R_d (right-hand plot) on pH and the concentration of oxalate in the contacting electrolyte solution

Model curves were obtained using the 2SPNE SC/EDL model using the data published in (Glaus et al. 2020) and complex formation data from (Glaus et al. 1997).

6 Effects of the clay compaction on surface diffusivity

6.1 Diffusion of Co(II) tracer at very high compaction of illite

6.1.1 Overview of scope and experimental conditions

The scope of this experiment was rather narrow: To measure the diffusion of a strongly sorbing tracer, $^{57}Co^{2+}$, at the highest achievable bulk-dry density for illite. For this purpose, the static-filter diffusion cells normally used for diffusion experiments with strongly swelling clays (Glaus et al. 2007), such as smectites, were applied for the present purpose. Under such conditions, the membrane in the membrane-confined diffusion cells would rupture. The bulk dry density obtained thereby was 2090 kg m^{-3}. The purpose of this experiment was to observe the effects of surface diffusion under conditions which are closer to those encountered in a consolidated clay rock. Note that an exact value for the clay density in clay rock cannot be specified. It depends on the clay content, the content of other minerals, the solid densities of those minerals and the assumptions made for the porosity of those other minerals. For a typical Opalinus Clay sample with a bulk dry density of ~ 2'400 kg m^{-3} and assumed fractional weight contents of 50% of clay, 40% of quartz and 10% of calcite, the bulk-clay dry density would be of the order of 2200 kg m^{-3} for the assumption that the clay is the only mineral component bearing porosity (Van Loon et al. 2021). Such a value is rather close to the illite bulk dry density obtained in the present experiment. For this reason, the results obtained here can be regarded as rather relevant for the situation in an intact clay rock.

Diffusion experiments were carried out at pH 5 in 0.1 M $NaClO_4$. In a first step, HTO through-diffusion was measured to determine the relevant *G*-factor for the diffusion of $^{57}Co^{2+}$. The $D_{e,c}$ value measured for HTO was $(5.6 \pm 0.9) \times 10^{-11}$ $m^2 s^{-1}$. The *G*-factor derived therefrom was 10.1 ± 1.9. The through-diffusion of HTO was then followed by in-diffusion of $^{57}Co^{2+}$ on the same clay sample, combined with profile analysis. Stable-isotope $CoCl_2$ was added to the tracer solution to obtain an excess of the stable isotope of factor ~ 3'400. The normal profiling technique which involves a stepwise extrusion of the clay sample in sub-millimetre steps from the sample holder could not be applied in the present case. Due to the high bulk-dry density and resulting strong swelling properties, the clay sample had to be forcibly removed as a single piece. The resulting spatial resolution obtained after cutting the extruded piece of clay was much less than normally achieved. The results of in-diffusion were evaluated using a $D_{e,f}$ of $\sim 2 \times 10^{-11}$ $m^2 s^{-1}$. Note that such a reference value could not be taken from literature. It has to be assumed that the clay sample exerted a very strong swelling force, by which the stainless-steel filters undergo deformation leading to a decreased porosity and potentially also to clogging of the filter pore space. All these effects produce lower $D_{e,f}$ value than normally experienced at lower bulk dry densities of the clay sample. The value used here was derived from the tracer depletion curve in the reservoir solution. The almost linear initial phase of tracer depletion is characteristic of a strong predominance of the filter diffusion properties on the time evolution of tracer depletion (Glaus et al. 2015b). It can therefore readily be used to derive those filter properties.

6.1.2 Results and EDL diffusion modelling for $^{57}Co^{2+}$ in-diffusion

The in-diffusion results of $^{57}Co^{2+}$ are shown in Fig. 6-1. Instead of the ordinary procedure of deriving best-fit parameter values for diffusion and sorption, a blind prediction of the diffusion data was applied for the present experiment. The blind prediction is based on eq. (2), using the *G*-factor derived from the effective diffusion coefficient measured for HTO and the speciation of $^{57}Co^{2+}$ in the EDL and bulk water according to the thermodynamic data published in Glaus et al. (2015a). The parameter values obtained thereby were a $D_{e,c}$ of 6.2×10^{-10} $m^2 s^{-1}$ and R_d of 0.58 m^{-3} kg. In view of the assumptions taken, such predictions are inherently associated with uncertainty. Important sources of uncertainty in the present case are (i) the concentration of Al^{3+} in solution and the choice for the multiplier of the Debye length (n_{DL}). The assumption used for the present experiment was that the concentration of Al^{3+} follows the measurements published in the Supporting Information of Glaus et al. (2015a). Fig. 6-2 shows simulations of $D_{e,c}$ and R_d as a function of the ionic strength for different assumptions regarding the critical influencing parameters. As can be seen from this plot, the impact of the uncertainties on $D_{e,c}$ is moderate, while it is almost negligible on R_d at the target ionic strength of 0.1 M.

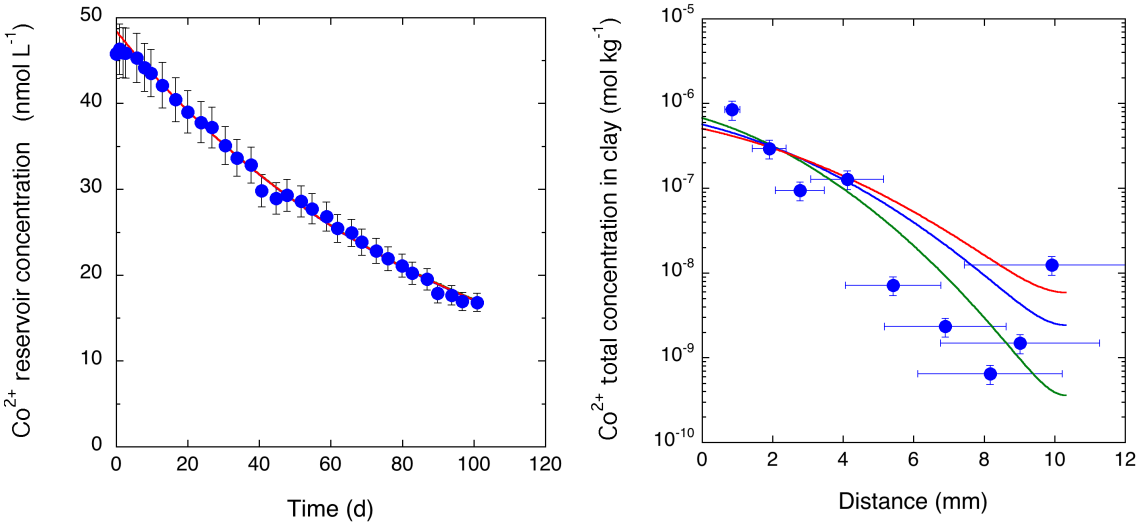

Fig. 6-1: Evolution of the upstream reservoir solution concentration of $^{57}Co^{2+}$ (left-hand plot) and the total $^{57}Co^{2+}$ concentration (per dry clay) in the clay segments (right-hand plot) at a bulk dry density of 2'090 kg m^{-3}, pH 5 and an ionic strength of 0.1 M

The green curve represents a blind prediction involving the G factor measured for HTO and the distribution of $^{57}Co^{2+}$ in the EDL calculated from the default model settings (cf. the text). The blue and red curve are sensitivity calculations (cf. Fig. 36) for assessing an estimate of the uncertainty of the blind prediction. They involve the impacts on $D_{e,c}$ and R_d both for reservoir concentration depletion and the profile. For this reason, the distribution does not follow a symmetric distribution in the profile.

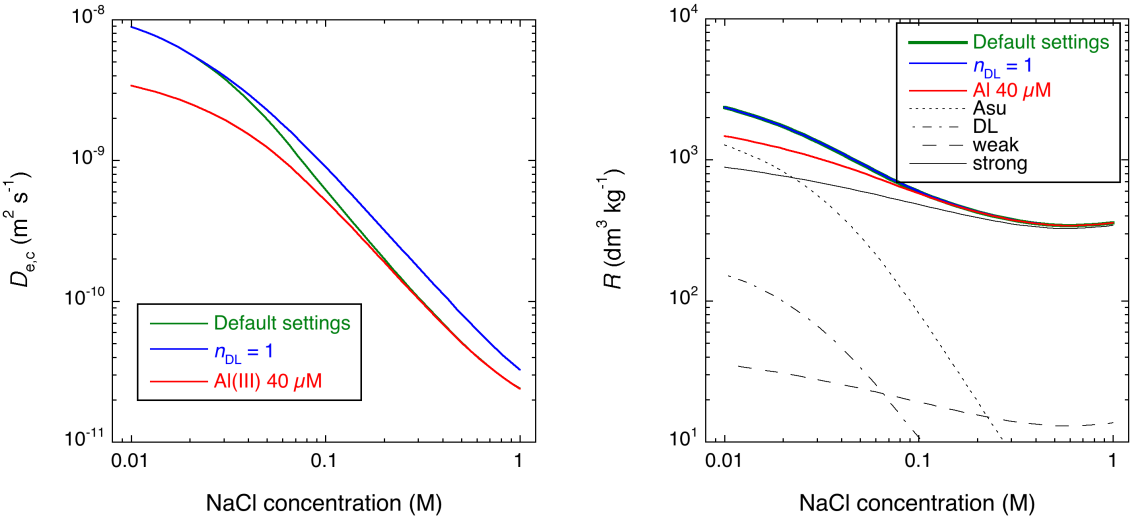

Fig. 6-2: Simulation of the $D_{e,c}$ and R_d values using speciation calculations in Phreeqc for pH 5

The default settings for n_{DL} are 2.0 and for the Al(III) concentration 4 µM. The right-hand plot shows additionally the contributions (black lines) of the different surface species to the overall R_d obtained for the default settings. Asu refers to the surface complexes in the Stern layer of the planar surfaces and DL to the species in the diffuse layer.

Fig. 6-1 shows that an excellent agreement exists between the experimental data and the modelling curve for the default assumptions. No impact of the parameter variation is noticeable in the reservoir concentration data in general. The reason lies in the fact that the diffusion properties of the confining membrane govern the time evolution of the reservoir concentration. The strongest deviation on the profile data is observed for the assumption of a 10-fold raised concentration of Al(III). Even for this unlikely assumption, the simulation curve is rather within the data uncertainty. This means that the set of thermodynamic data derived mostly from experiments carried out at clay bulk-dry densities of ~ 1'700 kg m^{-3} is also applicable at bulk-dry densities relevant for consolidated clay rock. This is important evidence which supports the validity of the application of diffusion and sorption data obtained from compacted illite for the prediction of the tracer diffusion behaviour in Opalinus Clay.

7 Conclusions

The present experimental material for compacted illite provides a broad basis for demonstrating the robustness of the predictive calculation of effective diffusion coefficients of moderately and strongly sorbing radiotracers adequate for given pore water and clay surface properties. Such parameter values are most appropriate for application in compilations of diffusion and retention parameters for various safety assessment scenarios. It demonstrates that an acceptable agreement between experimental data and blind model predictions could be attained.

Effective diffusion coefficients for sorbing species can thus be reliably predicted based on their calculated speciation in the aqueous phase and at the surface of illite, provided that the relevant geometry factors are known either from pertinent tracer measurements with non-sorbing species, or from empiric relationships with geomorphic basis data, such as porosity or mineral composition. The involvement of a law of mass action solver for calculating such a speciation represents thus a manageable effort in the compilation of element specific and pore water and clay surface dependent effective diffusion coefficients. It can safely be assumed that the Donnan concentration equilibrium distribution approach used here can similarly be applied for the calculation of the diffusion coefficients of anionic species.

Despite all the positive aspects regarding the applicability of these data, the intrinsic uncertainties should not be neglected. Normally, the evaluation of experimental data with a single-species diffusion model for strongly sorbing species contains uncertainties between a factor of 2 and 5. Added to this are the model uncertainties when extrapolating to unknown parameter combinations. Therefore, the model predictions for diffusion and sorption properties of unknown elements at unknown pore water conditions may have a range of at least one order of magnitude.

8 References

Aertsens, M., Van Laer, L., Maes, N. & Govaerts, J. (2017): An improved model for through-diffusion experiments: application to strontium and tritiated water (HTO) diffusion in Boom Clay and compacted illite, in: Norris, S., Bruno, J., VanGeet, M., Verhoef, E. (Eds.), Radioactive Waste Confinement: Clays in Natural and Engineered Barriers, pp. 205-210

Appelo, C.A.J. (2013): Analytical solutions for calculating the anion porosity and effective diffusion coefficients in illite. Catclay Deliverable (D-N°: 1-7)

Appelo, C.A.J. & Wersin, P. (2007): Multicomponent diffusion modeling in clay systems with application to the diffusion of tritium, iodide, and sodium in Opalinus Clay. Environ. Sci. Technol. 41, 5002-5007

Appelo, C.A.J., Van Loon, L.R. & Wersin, P. (2010): Multicomponent diffusion of a suite of tracers (HTO, Cl, Br, I, Na, Sr, Cs) in a single sample of Opalinus Clay. Geochim. Cosmochim. Acta 74, 1201-1219

Baes, C.F.J. & Mesmer, R.E. (1976): The hydrolysis of cations. John Wiley & Sons, Inc., New York, USA

Baeyens, B. & Fernandes, M.M. (2018): Adsorption of heavy metals including radionuclides, in: Schoonheydt, R., Johnston, C.T., Bergaya, F. (Eds.), Surface and Interface Chemistry of Clay Minerals, Vol 9, pp. 125-172

Bestel, M., Glaus, M.A., Frick, S., Gimmi, T., Juranyi, F., Van Loon, L.R. & Diamond, L.W. (2018): Combined tracer through-diffusion of HTO and ^{22}Na through Na-montmorillonite with different bulk dry densities. Appl. Geochem. 93, 158-166

Birgersson, M. & Karnland, O. (2009): Ion equilibrium between montmorillonite interlayer space and an external solution – consequences for diffusional transport. Geochim. Cosmochim. Acta 73, 1908-1923

Bradbury, M.H. & Baeyens, B. (1997): A mechanistic description of Ni and Zn sorption on Na-montmorillonite. 2. Modelling. J. Contam. Hydrol. 27, 223-248

Bradbury, M.H. & Baeyens, B. (2009a): Sorption modelling on illite Part I: Titration measurements and the sorption of Ni, Co, Eu and Sn. Geochim. Cosmochim. Acta 73, 990-1003

Bradbury, M.H. & Baeyens, B. (2009b): Sorption modelling on illite. Part II: Actinide sorption and linear free energy relationships. Geochim. Cosmochim. Acta 73, 1004-1013

Chagneau, A., Tournassat, C., Steefel, C.I., Bourg, I.C., Gaboreau, S., Esteve, I., Kupcik, T., Claret, F. & Schaefer, T. (2015): Complete Restriction of Cl-36(-) Diffusion by Celestite Precipitation in Densely Compacted Illite. Environmental Science & Technology Letters 2, 139-143

Davies, C.W. (1962): Ion association. Butterworths, London

Fukatsu, Y., Van Loon, L.R., Shafizadeh, A., Grolimund, D., Ikeda, Y. & Tsukahara, T. (2016): Effect of Celestite Precipitation in Compacted Illite on the Diffusion of HTO, Cl-36(-), and Na-22(+), 5th International Symposium on Innovative Nuclear Energy Systems (INES), Tokyo Inst Technol, Ookayama Campus, Tokyo, JAPAN, pp. 133-139

Gimmi, T. & Alt-Epping, P. (2018): Simulating Donnan equilibria based on the Nernst-Planck equation. Geochim. Cosmochim. Acta 232, 1-13

Glaus, M.A. (2018): Diffusion and sorption measurements of Eu(III) in compacted illite. PSI Internal Technical Report TM-44-18-15, Paul Scherrer Institut, Villigen, Switzerland

Glaus, M.A., Aertsens, M., Appelo, C.A.J., Kupcik, T., Maes, N., Van Laer, L. & Van Loon, L.R. (2015a): Cation diffusion in the electrical double layer enhances the mass transfer rates for Sr^{2+}, Co^{2+} and Zn^{2+} in compacted illite. Geochim. Cosmochim. Acta 165, 376-388

Glaus, M.A., Aertsens, M., Maes, N., Van Laer, L. & Van Loon, L.R. (2015b): Treatment of boundary conditions in through-diffusion: A case study of $^{85}Sr^{2+}$ diffusion in compacted illite. J. Contam. Hydrol. 177-178, 239-248

Glaus, M.A., Baeyens, B., Bradbury, M.H., Jakob, A., Van Loon, L.R. & Yaroshchuk, A. (2007): Diffusion of ^{22}Na and ^{85}Sr in montmorillonite: Evidence of interlayer diffusion being the dominant pathway at high compaction. Environ. Sci. Technol. 41, 478-485

Glaus, M.A., Frick, S. & Van Loon, L.R. (2020): A coherent approach for cation surface diffusion in clay minerals and cation sorption models: Diffusion of Cs^{+} and Eu^{3+} in compacted illite as case examples. Geochim. Cosmochim. Acta 274, 79-96

Glaus, M.A., Frick, S. & Van Loon, L.R. (2021): Competitive effects of cations on the diffusion properties of strongly sorbing trace cations in compacted illite and Opalinus Clay. ACS Earth and Space Chemistry 5, 2621-2625

Glaus, M.A., Frick, S., Rossé, R. & Van Loon, L.R. (2010): Comparative study of tracer diffusion of HTO, $^{22}Na^{+}$ and $^{36}Cl^{-}$ in compacted kaolinite, illite and montmorillonite. Geochim. Cosmochim. Acta 74, 1999-2010

Glaus, M.A., Hummel, W. & Van Loon, L.R.V. (1997): Experimental determination and modelling of trace metal - humate interactions: a pragmatic approach for applications in groundwater. PSI Bericht 97-13, Paul Scherrer Institut, Villigen, Switzerland. Also published as Nagra Technical Report NTB 97-03

Hax Damiani, L., Kosakowski, G., Glaus, M.A. & Churakov, S.V. (2020): A framework for reactive transport modeling using FEniCS–Reaktoro: governing equations and benchmarking results. Computational Geosciences 24, 1071-1085

Ishidera, T., Kurosawa, S., Hayashi, M., Uchikoshi, K. & Beppu, H. (2016): Diffusion and retention behaviour of Cs in illite-added compacted montmorillonite. Clay Minerals 51, 161-172

Krejci, P., Gimmi, T. & Van Loon, L.R. (2021): On the concentration-dependent diffusion of sorbed cesium in Opalinus Clay. Geochim. Cosmochim. Acta 298, 149-166

Lehikoinen, J., Muurinen, A. & Valkiainen, M. (1999): A consistent model for anion exclusion and surface diffusion. Mater. Res. Soc. Symp. Proc. 556, 663-670

Leroy, P., Revil, A. & Coelho, D. (2006): Diffusion of ionic species in bentonite. J. Colloid Interface Sci. 296, 248-255

Li, Y.H. & Gregory, S. (1974): Diffusion of ions in sea water and in deep-sea sediments. Geochim. Cosmochim. Acta 38, 703-714

Maes, N., Glaus, M.A., Baeyens, B., Marques Fernandes, M., Churakov, S.V., Dähn, R., Grangeon, S., Tournassat, C., Geckeis, H., Charlet, L., Brandt, F., Poonoosamy, J., Hoving, A., Havlova, V., Fischer, C., Scheinost, A.C., Noseck, U., Britz, S., Siitari-Kauppi, M. & Missana, T. (2021): State-of-the-Art-report on the understanding of radionuclide retention and transport in clay and crystalline rocks. Final version as of 30.04.2021 of deliverable D5.1 of the HORIZON 2020 project EURAD. EC Grant agreement no: 847593

Marques Fernandes, M. & Baeyens, B. (2020): Competitive adsorption on illite and montmorillonite: Experimental and modelling investigations. Nagra Technical Report NTB 19-05

Marques Fernandes, M., Vér, N. & Baeyens, B. (2015): Predicting the uptake of Cs, Co, Ni, Eu, Th and U on argillaceous rocks using sorption models for illite. Appl. Geochem. 59, 189-199

Montoya, V., Baeyens, B., Glaus, M.A., Kupcik, T., Marques Fernandes, M., Van Laer, L., Bruggeman, C., Maes, N. & Schäfer, T. (2018): Sorption of Sr, Co and Zn on illite: Batch experiments and modelling including Co in-diffusion measurements on compacted samples. Geochim. Cosmochim. Acta 223, 1-20

Nardi, A., Idiart, A., Trinchero, P., de Vries, L.M. & Molinero, J. (2014): Interface COMSOL-PHREEQC (iCP), an efficient numerical framework for the solution of coupled multiphysics and geochemistry. Computers & Geosciences 69, 10-21

Parkhurst, D.L. & Appelo, C.A.J. (1999): User's guide to PHREEQC (version 2), USGS Water Resources Inv. Report 99-4259. U.S. Geological Survey, Washington, DC

Parkhurst, D.L. & Appelo, C.A.J. (2013): Description of input and examples for PHREEQC version 3 - A computer program for speciation, batch-reaction, one-dimensional transport, and inverse geochemical calculations. U.S. Geological Survey Techniques and Methods, book 6, chap. A43, 497 p.

Rabung, T., Pierret, M.C., Bauer, A., Geckeis, H., Bradbury, M.H. & Baeyens, B. (2005): Sorption of Eu(III)/Cm(III) on Ca-montmorillonite and Na-illite. Part 1: Batch sorption and time-resolved laser fluorescence spectroscopy experiments. Geochim. Cosmochim. Acta 69, 5393-5402

Rolle, M., Sprocati, R., Masi, M., Jin, B.A. & Muniruzzaman, M. (2018): Nernst-Planck-based description of transport, coulombic interactions, and geochemical reactions in porous media: Modeling approach and benchmark experiments. Water Resour. Res. 54, 3176-3195

Sekine, T. (1964): Complex formation of La(III), Eu(III), Lu(III) and Am(III) with oxalate, sulphate, chloride and thiocyanate ions. Journal of Inorganic & Nuclear Chemistry 26, 1463-1465

Tournassat, C., Chapron, Y., Leroy, P., Bizi, M. & Boulahya, F. (2009): Comparison of molecular dynamics simulations with triple layer and modified Gouy-Chapman models in a 0.1 M NaCl-montmorillonite system. J. Colloid Interface Sci. 339, 533-541

Van Loon, L.R., Glaus, M.A., Bunic, P. & Frick, S. (2021): Summary of diffusion results for HTO, $^{36}Cl^-$ and $^{22}Na^+$ measured in TBO samples of Trüllikon1-1. PSI Internal Technical Report TM-44-21-01, Paul Scherrer Institut, Villigen PSI, Switzerland.

Wigger, C., Kennell-Morrison, L., Jensen, M., Glaus, M.A. & Van Loon, L. (2018): A comparative anion diffusion study on different argillaceous, low permeability sedimentary rocks with various pore waters. Appl. Geochem. 92, 157-165

Wissmeier, L. & Barry, D.A. (2011): Simulation tool for variably saturated flow with comprehensive geochemical reactions in two- and three-dimensional domains. Environ. Model. Software 26, 210-218

Appendix A

A.1 Set of thermodynamic auxiliary data

Tab. A-1 provides the equilibrium constants for the formation of complexes with inorganic anions (denoted as *I,* such as chloride and sulfate) and the hydrolysis constants for the various cations relevant for the reported work. The former reactions constants are based on the stepwise (n = 1, 2, etc.) stoichiometrical overall reactions, where Me^{z+} denotes the aquaion of a metal Me with charge number z:

$$Me^{z+} + nI^{y-} = MeI_n^{z-ny} \quad (A1)$$

The hydrolysis constants are defined based on

$$Me^{z+} = Me(OH)_n^{z-n} + nH^+ \quad (A2)$$

Tab. A-1: Thermodynamic data (logarithmic values, overall complex formation constants) for the formation of inorganic aqueous complexes

The values for the incremental increase of the stoichiometric number of ligands (n) are given in a row, separated by a slash sign.

Cation	Cl^-	SO_4^{2-}	HSO_4^-	OH^-
Na^+		0.7		-10
K^+		0.85		
Mg^{2+}		2.37		-11.44 / -10.1 / -16.9 / -22.7
Ca^{2+}		2.25	1.08	-12.78
Al^{3+}		3.5 / 5.0	0.46	-5.0
Co^{2+}	0.15	0.044		-9.3 / -18.6 / -31.7
Mn^{2+}	0.61 / 0.25 / -0.31	2.25		-10.6 / n.d. / -34.8
Fe^{2+}	0.14	2.25	1.08	-9.1 / -20.6 / -31.0
Eu^{3+}	0.24 / -0.74	3.3 / 3.7		-7.2 / -15.1 / -26.2

Tab. A-2 provides the equilibrium constants for the formation of the surface species at the surfaces of illite (basal and edge surfaces). The data are related to the following reactions (where j represents the stepwise increase of stoichiometrical number):

$$Me^{z+} + jAsu^- = MeAsu_j^{z-j} \quad (A3)$$

Asu^- is a formal site for surface complexation at the basal surfaces via the fixed lattice charges (denoted to as Stern layer site). The site capacity of Asu^- sites is given by the cation exchange capacity. Note that by convention, the stoichiometry coefficient *j* equals the charge number of the metal cation *z*. The $MeAsu_j^{z-j}$ complexes have thus a rather formal character as an alternative description of cation exchange taking into account electrostatic effects via the combined effect of surface complexation plus cationic species in the diffuse layer (see Section 1.2).

$$\equiv S^sOH + Me^{z+} = \equiv S^sOMe(OH)_{j-1}^{2-j} + jH^+ \quad (A4)$$

Where $\equiv S^sOH$ is the mono-protonated strong surface site

$$\equiv S^wOH + Me^{z+} = \equiv S^wOMe(OH)_{j-1}^{2-j} + jH^+ \quad (A5)$$

where $\equiv S^wOH$ is the mono-protonated weak surface site

Tab. A-2 also comprises the selectivity coefficients for cation exchange against Na^+ according to the Gaines-Thomas convention. These reaction constants were not directly used in the present report for speciation calculations but used to estimate the equilibrium constants of the $MeAsu^{z-1}$ surface complexes. For this reason, they are also tabulated here.

Tab. A-2: Thermodynamic data (logarithmic values) for the formation of surface species at the surfaces of illite. The values for the incremental increase of the stoichiometric number of protons involved in the reaction stoichiometry (j) are given in a row, separated by a slash sign.

Site types	**Strong sites**	**Weak sites**	**Stern layer sites**	**Cation exchange sites**
Site capacities (mol kg^{-1})	2×10^{-3}	4.0×10^{-2}	1.9×10^{-1}	1.9×10^{-1}
Formation constants [a] for the addition of	$^s\beta$	$^w\beta$	^{Su}K	^cK [b]
H^+	6.2 / 4.0	6.2 / 4.0	-0.8	0
Na^+	–	–	-0.7	0
K^+	–	–	-1.0	0.1
Mg^{2+}	–	–	0.107	1.0
Ca^{2+}	–	–	0.104	1.0
Al^{3+}	–	–	0.3	1.0
Co^{2+}	0.9 / -7.0 / -16.5	-1.8	0.65	1.3
Mn^{2+}	0.55	-1.5 [c]	0.30	1.5
Fe^{2+}	2.1 / -6.4 / -15	-1.4 / -7.7	0.76	0.6
Eu^{3+}	1.9 / -4.7 / -12.7 / -24	0.0 / -7.0	1.20	1.9

[a] Logarithmic values
[b] Selectivity coefficients for cation exchange against Na+ according to the Gaines-Thomas convention
[c] An improved agreement with experimental data was obtained by the introduction of additional surface complexes (see Section 3.3).

A.2 Phreeqc template input file for isotherm calculation

```
# Sorption isotherm Mn / IdP, status January 2021, fixed to 0.1 M and pH 7.3
# Site selection and parametrisation of surface complexation constants based on Exp. 18008.TON and 20001.TON
# All sites (strong, weak-1, auxiliary(wx), EDL) are necessary for a comprehensive description of sorption and diffusion results
# Calculations done for rhob 1.703 kg/L using a loop for the solution concentration of Mn2+
# Competing cations according to pH dependent empirical functions (Catclay)
#
# Output Graph 1: Isotherm
# OutputGraph 2: formally calculated Kc values (sum of Stern layer + Diffuse layer species)


INCLUDE$ z:\phreeqc\database\NagraA7_MiG.dat # Referring to the data shown in Tab. A-1and Tab. A-2
KNOBS; -iter 1000; -diagonal_scale true; -tolerance 1e-19; -step_size 10; -pe_step_size 5 # aids convergence
PHASES
# adjust the solubility of Gibbsite according to the empirical functionality
Gibbsite
Al(OH)3 + 3 H+ = Al+3 + 3 H2O
# -log_k 8.11 #original
-log_k  9 #adjusted
-delta_h -22.800 kcal


PRINT; -reset false; -user_print true;# -echo_input true
SOLUTION 1
SELECTED_OUTPUT; selected_out true; -reset false; -file isocomp.prn
USER_PUNCH
1 sc$ = chr$(59)
2 nl$ = eol$

3 ion_str = 0.1 # ionic strength, needs to be set for the calculation of appak
5 Mnsol = 2.5e-3 # Solution concentration of Mn, mmol/kg
8 peha = 7.3 # pH

# Fundamental input data for geometry, according to 'param.xlsx'
10 rhob = 1.703 : rhos = 2.8 : por_clay = 1- rhob/rhos: esel = rhob / por_clay : liquid = 1# kg L scale, param.xlsx
20 Su = 0.19 : SC_s = 2e-3 : SC_wa = 4e-2 : SC_wx = 5e-4 # site densities mol/kg
30 Asp = 100 : Asp_l = Asp * esel * 1000 : Asp_v = Asp_l / 1000# specific surface m^2/g, or m^2/L
45 Su_l = Su * esel : SC_wa_l = SC_wa * esel : SC_wx_l = SC_wx * esel : SC_s_l = SC_s * esel # eq/L

50 pore_r = 2e-3 / Asp_l # pore radius / m
55 r_lim = 0.01 # smallest radius fraction of 'free' porewater
60 Far = 96493.5 : R = 8.3147 : ee = 8.854e-12 * eps_r

85 r_lim = 0.01 # smallest radius fraction of 'free' porewater
90 d_closest = 0e-10 # the closest an ion can come to the surface, m

# Setting the range and scaling the variation of Mn concentration logarithmically
100 c1 = 1e-8 # mol/kgw
110 cf = 1e-2
120 nsol = 100
130 c_incr = (log(cf) - log(c1)) / (nsol - 1)
140 dim c(nsol)
150 c(1) = c1
160 for i = 2 to nsol
170 c(i) = exp(log(c(i - 1)) + (c_incr))
180 next i
# Writing down fixed values to memory
185 put(esel, 4)
187 put(liquid, 5)
189 put(muehs_Mn, 7)
191 put(tort_n, 8)
```

```
193 put(por_clay, 9)
195 put(Dw_Mn, 10)

# Looping the punch of Solution and Surface Blocks in the prn file, incrementing number is Mn concentration
200 for i = 1 to nsol

201 appak = sqrt(ee * R * TK / (2 * ion_str * 1e3)) / Far # Debye length / m
202 n_DB = 2 # Number of Debye lengths
203 d_DL = n_DB * appak

 # define pore geometry
210 pore_geom$ = 'circ' # 'circ' for circular, 'plan' for planar
215 if pore_geom$ = 'circ' then goto 255
220 # for planar pore
225 f_void = 2 * d_closest / pore_r
230 if (1 - 2 * (d_DL + d_closest) / pore_r) <= r_lim^2 then f_free = r_lim^2 : d_DL = (pore_r * (1 - r_lim) - 2*d_closest) / 2 \
235 else f_free = 1 - 2 * (d_DL + d_closest) / pore_r
240 f_DL = 1 - f_free - f_void
245 goto 275
250 # for circular pore
255 f_void = (2 * pore_r * d_closest - d_closest^2) / pore_r^2 # goto 255
260 if d_DL + d_closest > pore_r * (1 - r_lim) then f_free = r_lim^2 else f_free = (pore_r - d_DL - d_closest)^2 / pore_r^2
265 d_DL = 1e-3 * (1 - f_free - f_void) / Asp_l
270 f_DL = 1 - f_free - f_void

275 print 'por_clay =', por_clay, 'rho_b /(g/ml) =', rhob, 'ISt /M =', ion_str, 'esel=',esel # goto 275
277 if pore_geom$ = 'circ' then print 'pore geometry = circular' else print 'pore geometry = planar'
279 print 'A_ext /(m2/g) =', Asp, 'A_por /(m2/L pore water) =', Asp_l
281 print 'f_DL =', f_DL, 'f_free =', f_free, 'f_tot =' f_DL + f_free, 'd_DL =', d_DL
283 print 'pore_r /nm =', pore_r * 1e9, 'appak =', appak


# Looping the punch of Solution and Surface Blocks in the prn file, incrementing number is the concentration of Mn2+
300 for i = 1 to nsol

# Polynomial factors for correction functions Mg, Ca, Al
# Al factors
310 emm0 = -814.773225 : emm1 = 731.452268 : emm2 = -196.073738 : emm3 = -21.4593108 : emm4 = 25.2256912 :
emm5 = -6.68670029 : emm6 = 0.927341704 : emm7 = -7.34493659e-2 : emm8 = 3.15170049e-3 : emm9 = -5.70399562e-5
# Mg factors
315 emm0Mg = 0.023591 : emm1Mg = -0.0021351
# Ca factors
320 emm0Ca = 0.081546 : emm1Ca = -0.0068249

330 n$ = TRIM(STR$(c(i) * 1000)) # goto 310
335 sol$ = nl$ + 'SOLUTION 1' + sc$ + '-water ' + TRIM(STR$(liquid*f_free)) + nl$
340 sol$ = sol$ + ' Na ' + TRIM(STR$(ion_str*1000)) + sc$ + ' Cl ' + TRIM(STR$(ion_str*1000)) + ' charge' + nl$
345 sol$ = sol$ + ' Ca ' + str$(emm0Ca + emm1Ca * peha) + nl$
350 sol$ = sol$ + ' Mg ' + str$(emm0Mg + emm1Mg * peha) + nl$
355 sol$ = sol$ + ' K 0.2 ' + nl$
360 sol$ = sol$ + ' Al 1e-5 Gibbsite ' + str$(emm0 + emm1*peha + emm2*peha^2 + emm3*peha^3 + emm4*peha^4 + emm5*peha^5
+ emm6*peha^6 + emm7*peha^7 + emm8*peha^8 + emm9*peha^9) + nl$
365 sol$ = sol$ + 'Mn ' + n$ + nl$
370 sol$ = sol$ + ' pH 7.3 ' + nl$

400 surf$ = 'SURFACE 1' + sc$ + ' -equil 1' + nl$
405 surf$ = surf$ + 'Asu_ ' + TRIM(STR$(Su_l * liquid)) + ' ' + TRIM(STR$(Asp_l)) + ' ' + TRIM(STR$(liquid)) + nl$
410 surf$ = surf$ + 'Sill_waOH ' + TRIM(STR$(SC_wa_l * liquid)) + ' ' + TRIM(STR$(Asp_v)) + ' ' + TRIM(STR$(liquid)) + nl$
415 surf$ = surf$ + 'Sill_wxOH ' + TRIM(STR$(SC_wx_l * liquid)) + ' ' + TRIM(STR$(Asp_v)) + ' ' + TRIM(STR$(liquid)) + nl$
420 surf$ = surf$ + 'Sill_sOH ' + TRIM(STR$(SC_s_l * liquid)) + ' ' + TRIM(STR$(Asp_v)) + ' ' + TRIM(STR$(liquid)) + nl$
425 surf$ = surf$ + ' -Donnan ' + TRIM(STR$(d_DL)) + nl$

430 punch sol$
435 punch nl$ + surf$
```

```
450 punch 'USE solution none ' + nl$
455 punch 'END ' + nl$

700 put(c(i), 1, i)
705 put(f_free, 2, i)
710 put(f_DL, 3, i)
715 put(d_DL, 4, i)
720 put(Su_l, 5, i)
750 next i
 END

PRINT; -selected_out false # PRINT

# User graph calculates total Mn-sorbed using two routes: (i) via 'sys' and (ii) via summation of all surfacspecies (sum_surf)
# This procedure is used as an internal consistency check
USER_graph 1 : Mn isotherm on IdP pH7.3
 -headings tot_sys Sum_EDL Sum_s Sum_wa Sum_wx sum_surf
 -chart_title "Mn isotherm on Illite (pH 7.3, I=0.1M)"
 -axis_titles "log Mn-solution/ (mol/kgw)" "log Mn-sorbed / (mol/kg)" #"Kd / (L/kg)"
 -axis_scale x_axis -8 -2 auto auto
 -axis_scale y_axis -5 -1 auto auto
 -initial_solutions true
1 if tot("Asu_") = 0 then goto 200
10 esel = get(4)
15 f_free = get(2, sim_no - 1)
20 f_DL = get(3, sim_no -1)
25 d_DL = get(4, sim_no - 1)
30 liquid = get(5) : free = liquid * f_free
35 sum_s = mol("Sill_sOMnCl") * free # mol
40 sum_wa = mol("Sill_waOMnCl") * free # mol
45 sum_EDL = mol("MnAsu_2") * free + edl("Mn", "Asu") # mol
50 sum_wx = mol("Sill_wxOMnCl") * free # mol
 # watch out for units! 'mol'= molality, edl: substance amount
70 sum_surf = sum_s + sum_wa + +sum_wx + sum_EDL

# print a few things...
# 90 if sim_no = 2 then print " Mn ",' ', "f_free ",' ', "f_DL ",' ', "d_DL ",' ', "n(mol) of Mn in EDL "
# 91 if sim_no = 2 then print "=============",' ',"=============" ' ',"=============" ' ',"============="
# 92 print tot("Mn"), ' ', f_free, ' ', f_DL , ' ', d_DL, ' ', edl("Mn", "Asu")

100 plot_xy log10(tot("Mn")), log10 ( ( sys("Mn")/(tot("Mn") * liquid) -1) / esel * tot("Mn") )
105 plot_xy log10(tot("Mn")), log10 ((sum_EDL /(esel*liquid))), symbol_size = None
110 plot_xy log10(tot("Mn")), log10 (sum_s / (esel*liquid)), symbol_size = None
115 plot_xy log10(tot("Mn")), log10 (sum_wa / (esel*liquid)), symbol_size = None
120 plot_xy log10(tot("Mn")), log10 (sum_wx / (esel*liquid)), symbol_size = None
125 plot_xy log10(tot("Mn")), log10 (sum_surf / (esel*liquid)) , symbol_size = 2, color = Black, line_width = 3

190 put(sim_no , 99)
200 end

USER_GRAPH 2
-headings Kc_KNa Kc_CaNa Kc_MgNa Kc_MnNa
# -plot_tsv_file De_afo_sal.txt
 -initial_solutions true
 -chart_title " 'Kc Werte', EDL model"
 -axis_titles "log Mn-solution/ (mol/kgw)" " 'Kc' " #"Kd / (L/kg)"
 -axis_scale x_axis -8 -2 auto auto
 -axis_scale y_axis 0 auto auto auto

1 if tot("Asu_") = 0 then goto 200
10 esel = get(4)
15 f_free = get(2, sim_no - 1)
20 f_DL = get(3, sim_no -1)
25 d_DL = get(4, sim_no - 1)
35 liquid = get(5) : V_free = liquid * f_free
```

```
40 Su_l = get(5, sim_no - 1)
50 n_pl = liquid * Su_l
55 ch_Ca = 2: ch_Mg = 2: ch_Mn = 2: ch_Na = 1: ch_K = 1
60 n_Ca = edl("Ca","Asu") + mol("CaAsu_2") * V_free
65 n_Mg = edl("Mg","Asu") + mol("MgAsu_2") * V_free
70 n_Mn = edl("Mn","Asu") + mol("MnAsu_2") * V_free
75 n_Na = edl("Na","Asu") + mol("NaAsu_") * V_free
80 n_K = edl("K","Asu") + mol("KAsu_") * V_free
85 N_Ca = ch_Ca * n_Ca / n_pl
90 N_Mg = ch_Mg * n_Mg / n_pl
95 N_Mn = ch_Mn * n_Mn / n_pl
100 N_Na = ch_Na * n_Na / n_pl
105 N_K = ch_K * n_K / n_pl
110
115 kaze_KNa = N_K / (N_Na) * act("Na+") / act("K+")
120 kaze_CaNa = N_Ca / (N_Na)^2 * act("Na+")^2 / act("Ca+2")
125 kaze_MgNa = N_Mg / (N_Na)^2 * act("Na+")^2 / act("Mg+2")
130 kaze_MnNa = N_Mn / (N_Na)^2 * act("Na+")^2 / act("Mn+2")

# print a few things...
# 135 if sim_no = 2 then print " V_free "
# 136 if sim_no = 2 then print "=============="
# 137 print tot("Ca")

# graph...
140 plot_xy log10(tot("Mn")), (kaze_KNa), symbol = None , color = Red , line_width = 2
145 plot_xy log10(tot("Mn")), (kaze_CaNa), symbol = None , color = Blue , line_width = 1
150 plot_xy log10(tot("Mn")), (kaze_MgNa), symbol = None , color = Green , line_width = 3
155 plot_xy log10(tot("Mn")), (kaze_MnNa), symbol = None , color = Magenta , line_width = 2

190 put(sim_no , 99)
200 end

INCLUDE$ isocomp.prn
END
```

A.3 Phreeqc template input file for in-diffusion calculation

It would go beyond the scope of the present report to explain in detail the structure of the following sample. More explanations can be found in Parkhurst & Appelo (2013). The command structure should reveal how the geometric structure of cells containing a solution and a surface is composed. The cell structure was originally derived for the purpose of simulating advective mass transport in a column of cells with diffusion occurring in a series of so-called stagnant cells contacting the advection cells. Cells 0–2 are only dummy cells representing advective cells. The cell discretisation scheme shown here comprises 5 clay cells sandwiched by each a single membrane or filter cell, with the following numbering of cells 3 to *n* (n = 11 in the present case):

- *n* = 3: The upstream reservoir containing the radiotracer
- *n* = 4: The membrane at the upstream side, represented as a single cell
- *n* = 5–9: The clay specimen, subdivided into 5 cells
- *n* = 10: The filter at the downstream side, represented as a single cell
- *n* = 11: The downstream reservoir devoid of the radiotracer

In the present sample, the number of cells per domain is thus fixed and produces an approximate solution, only. The solution produced in Fig. 3-12 was obtained using a discretisation involving 3 cells per membrane (or filter) and 15 cells per clay domain. However, much more calculation

time is required for such a setup. Also note that all solution volumes and molar amounts of sites need to be adapted when further refining the cell structure. The parameter values shown here are only appliable for the present discretisation scheme. Similarly, the mixing factors and the time stepping depends on the subdivision of the cells.

```
# Mn in-Diffusion, Exp 17A2
# solution can be taxed only as approximate, in view of the 1-D structure of cells
# reality is rather characterised by a 2-D structure


INCLUDE$ z:\phreeqc\database\NagraA7_MiG.dat
KNOBS; -iter 1000; -diagonal_scale true; -tolerance 1e-19; -step_size 10; -pe_step_size 5 # aids convergence
PHASES
# adjust the solubility of Gibbsite according to the empirical functionality
Gibbsite
Al(OH)3 + 3 H+ = Al+3 + 3 H2O
# -log_k 8.11 #original
-log_k 9 #adjusted
-delta h -22.800 kcal

SOLUTION_SPECIES
Mn+2 = Mn+2 ; -erm_ddl 0.6

SOLUTION 0-2 dummy column with 1 cell, calc`s are done with stagnant cells 3 to ...
 Na 1; Cl 1
END

SOLUTION 3
-water 0.0605 # source reservoir volume / L
Na 100 charge; Cl 100; Mn 0.099 ; K 0.1; Mg 0.02; ; Ca 0.03#; Al 1e-3 Gibbsite 1;
pH 7.3

USER_GRAPH 1 Source reservoir
# -plot_csv_file Cusb_17A2.txt
-headings EDL_model
-axis_titles "Time / days" "Mn-conc / (mol/m^3)"
-chart_title "Source reservoir, Mn_stable"
-plot_concentration_vs time
1 if cell_no > 3 then end
10 days = total_time / (3600 * 24)
30 plot_xy days, tot("Mn") *1000, color = Red, symbol = None
# 40 plot_xy days, tot("Na") * 1e3, y_axis = 2, color = Black , symbol = None, line_width = 2
50 end
-end

PRINT ; -reset false; -echo_input true; -user_print true

# tracer-in filter cells...
SOLUTION 4; -water 7.1499e-05
 Na 100 charge ; Cl 100 ; Mg 0.02 ; Ca 0.03 ; pH 5.0
 K 0.1

# cells in clay sample...
SOLUTION 5; -water 5.4628e-06
 Na 100 charge ; Cl 100 ; Mg 0.02 ; Ca 0.03 ; pH 5.0
 K 0.1
SURFACE 5; -equil 5;
 Asu_ 1.3284e-05 4.3447e+05 1.6092e-05
 Sill_wa 2.7965e-06 4.3447e+03 1.6092e-05
 Sill_wx 3.4957e-08 4.3447e+03 1.6092e-05
 Sill_s 1.3983e-07 4.3447e+03 1.6092e-05
 -Donnan 1.5203e-09
```

```
SOLUTION 6; -water 5.4628e-06
 Na 100 charge ; Cl 100 ; Mg 0.02 ; Ca 0.03 ; pH 5.0
 K 0.1
SURFACE 6; -equil 6;
 Asu_ 1.3284e-05 4.3447e+05 1.6092e-05
 Sill_wa 2.7965e-06 4.3447e+03 1.6092e-05
 Sill_wx 3.4957e-08 4.3447e+03 1.6092e-05
 Sill_s 1.3983e-07 4.3447e+03 1.6092e-05
 -Donnan 1.5203e-09

SOLUTION 7; -water 5.4628e-06
 Na 100 charge ; Cl 100 ; Mg 0.02 ; Ca 0.03 ; pH 5.0
 K 0.1
SURFACE 7; -equil 7;
 Asu_ 1.3284e-05 4.3447e+05 1.6092e-05
 Sill_wa 2.7965e-06 4.3447e+03 1.6092e-05
 Sill_wx 3.4957e-08 4.3447e+03 1.6092e-05
 Sill_s 1.3983e-07 4.3447e+03 1.6092e-05
 -Donnan 1.5203e-09

SOLUTION 8; -water 5.4628e-06
 Na 100 charge ; Cl 100 ; Mg 0.02 ; Ca 0.03 ; pH 5.0
 K 0.1
SURFACE 8; -equil 8;
 Asu_ 1.3284e-05 4.3447e+05 1.6092e-05
 Sill_wa 2.7965e-06 4.3447e+03 1.6092e-05
 Sill_wx 3.4957e-08 4.3447e+03 1.6092e-05
 Sill_s 1.3983e-07 4.3447e+03 1.6092e-05
 -Donnan 1.5203e-09

SOLUTION 9; -water 5.4628e-06
 Na 100 charge ; Cl 100 ; Mg 0.02 ; Ca 0.03 ; pH 5.0
 K 0.1
SURFACE 9; -equil 9;
 Asu_ 1.3284e-05 4.3447e+05 1.6092e-05
 Sill_wa 2.7965e-06 4.3447e+03 1.6092e-05
 Sill_wx 3.4957e-08 4.3447e+03 1.6092e-05
 Sill_s 1.3983e-07 4.3447e+03 1.6092e-05
 -Donnan 1.5203e-09


# tracer-out filter cells...
SOLUTION 10; -water 7.1499e-05
 Na 100 charge ; Cl 100 ; Mg 0.02 ; Ca 0.03 ; pH 5.0
 K 0.1

#downstream solution...
SOLUTION 11; -water 1
 Na 100 charge ; Cl 100 ; Mg 0.02 ; Ca 0.03 ; pH 5.0
 K 0.1
END

# mixing factors...
MIX 3; 4 2.7337e-05
MIX 4; 5 6.5172e-07
MIX 5; 6 3.3382e-07
MIX 6; 7 3.3382e-07
MIX 7; 8 3.3382e-07
MIX 8; 9 3.3382e-07
MIX 9; 10 6.5172e-07
MIX 10; 11 2.7337e-05
END
```

```
TRANSPORT
 -warnings false
 -shifts 2393
 -flow diff; -cells 1; -bcon 1 2; -stag 9
 -time 720 10
 -multi_D true 6.8000e-10 3.9190e-01 0.0 1.8842e+00
 -punch_fr 3; -punch_c 3 11
 -print_fr 2393
END

USER_GRAPH 1; -detach

TRANSPORT
-shifts 1; -punch_frequency 1; -punch_cells 5-9

USER_GRAPH 2 Clay profile
 -headings EDL_model
 -axis_titles "Distance / mm" "Mn-stable / (mol/m^3)"
 -chart_title "Clay profile (per volume)"
 # -plot_csv_file Cclay_17A2.txt
 -axis_scale y_axis a a a a log
 10 clay_cells = 5 : start_cell = 5 : thickn_clay = 10.05 : por_clay = 0.3919
 20 x = (cell_no - start_cell ) * thickn_clay / clay_cells + thickn_clay / clay_cells / 2
 30 plot_xy x, sys("Mn") / (thickn_clay/1000/clay_cells * 3.1416 * (0.51e-2/2)^2),\
  y_axis = 1, color = Red, symbol = None
-end

  USER_GRAPH 3 Rd profile
 -headings erde_Mn tot(Mn)
 -axis_titles "Distance / mm" "log Rd / (dm^3/kg)" "log Mn-Lösungsphase / (mol/kg)"
 -chart_title "Clay profile (per volume)"
# -plot_csv_file Cclay_I5c.txt
-axis_scale y_axis a a a a
 1 por_clay = 0.3919
 2 rho_b_eps = 2.80 * (1 - por_clay) / por_clay
 3 rho_b = 2.80 * (1 - por_clay)
 5 Vpor = tot("water") + edl("water")
 10 clay_cells = 5 : start_cell = 5 : thickn_clay = 10.05 : por_clay = 0.3919
 20 x = (cell_no - start_cell ) * thickn_clay / clay_cells + thickn_clay / clay_cells / 2
 25 erde_Mn = (sys("Mn") / tot("Mn") / Vpor - 1) / rho_b_eps
 26 plot_xy x, log10(erde_Mn), y_axis = 1, color = Red
 # 27 erde2_Mn = (sys("Mn") / (thickn_clay/100/clay_cells * 3.1416 * (5.1e-2/2)^2)) / rho_b / tot("Mn")
 # 30 plot_xy x, log10(erde2_Mn), y_axis = 1, color = Blue, symbol = None , line_width = 3
 35 plot_xy x, log10(tot("Mn")), y_axis = 2, color = Black
 -end
END
```

A.4 Diffusion experiments with Fe(II)

A rather extensive series of experimental investigations was undertaken to measure the diffusion and sorption properties of ferrous iron (Fe(II)) in compacted illite. These experiments were not successful in all respects because of unwanted oxidation of ferrous to ferric iron (Fe(III)). For this reason, and because no comprehensive sorption and diffusion model could be derived from the experimental data, the results are not described in the main text. However, some valuable conclusions for diffusion and retardation properties can be drawn though, and therefore these results are reported in short form in the present Appendix. The experiments can be subdivided into three main groups:

- Experiments addressing the chemical stability of Fe(II) in homogeneous electrolyte solutions or suspensions of IdP in the appropriate electrolytes under defined (buffered) pH conditions. All these experiments were carried out under oxygen-free conditions in a N_2-glove box using analytical grade $Fe(II)SO_4 \cdot 7H_2O$ as the parent compound. The electrolytes were covering typically NaCl electrolytes buffered to pH 4 to 8. Analysis of the redox state of Fe was performed by ion chromatography in which the Fe(II) and Fe(III) oxidation states were separated on the separation column and detected using colorimetry after post-column reaction with a chelating agent (cf. Section A.4.1). A series of test measurements to evaluate this method and to assess potential artefacts in the results caused by unwanted oxidation of Fe(II) were carried out. Note that the chromatographic measurements had to be carried out under laboratory atmosphere at a pH of ~ 4.2. The presence of oxygen had to be cautiously avoided, but without the addition of reducing agents because their presence would lead to a bias in the ratio of the two redox forms of Fe in the eluting solution compared to the initial ratio in the injected sample.

  The results of these experiments are not described in detail. Summarising it may be stated that it was possible to prepare homogeneous solutions containing Fe(II) which were chemically stable at different concentration levels in a pH range between 4 and 7. Monitoring the oxygen concentration levels in the solutions using a fibre optic instrument (Fibox 4 trace instrument combined with a POF-L2.5-1SMA polymer optical fibre and using PSt6 oxygen sensor spots, obtained from PreSens Precision Sensing GmbH, Regensburg, Germany) turned out to be helpful. Note that the box atmosphere contains < 0.1 ppm of oxygen. Aqueous solutions in equilibrium with such an atmosphere are expected to contain of the order of magnitude $<10^{-10}$ mol/L of oxygen. Such concentration levels cannot be detected using the fibre optic system because the detection limits are a factor of ~ 100 higher. However, for example, oxygen concentration levels of 2.5×10^{-8} mol/L – which is above the limit of detection – are not expected to significantly alter the oxidation states of closed Fe(II) solutions > 1µM simply because of reasons of stoichiometric limitation. In the course of the method testing, it turned out that in all cases in which undesired oxidation of Fe(II) occurred, this could be explained by unnoticed carry-over of oxygen in solutions or in chemicals freshly transferred into the glove box. For this reason, the only valuable practice was to store chemicals and the ultrapure water for at least 1 day in the glove box before use. The ultrapure water was boiled and cooled down under a stream of nitrogen before transfer to the glove box. Fe(II) solutions prepared under these precautions were stable.

- In-diffusion experiments of Fe(II) in compacted IdP in the pH range 4 to 8 and covering ionic strengths between 0.01 and 0.6 M. The parent form of the tracer was ^{55}Fe in the ferric iron form, which had to be converted to the ferrous form before the start of the experiments. Several approaches were chosen for this step, including (i) electrochemical reduction of Fe(III) and (ii) isotopic exchange between $^{55}Fe(III)$ and stable isotope Fe(II). After various tests, it turned out that electrochemically reduced $^{55}Fe(III)$ could only be stabilised in the ferrous form by the addition of rather large concentrations of stable Fe(II). Alternatively, it was also possible to produce a long-term stable $^{55}Fe(II)$ form at pH values between 5 and 7

simply by mixing $^{55}Fe(III)$ and stable isotope Fe(II). The concentration ranges of stable-isotope Fe(II) required to obtain a sufficient chemical stability of the ^{55}Fe tracer are at millimolar concentrations. For this reason, it proved impracticable to conduct diffusion experiments at trace conditions.

- Competition experiments in which the illite was previously converted to mixed Na^+/Fe(II) forms using various ratios of the two cations in order to mask the edge sorption sites with Fe(II) at different levels of saturation. These clay preparations were subsequently used for in-diffusion measurements of $^{57}Co^{2+}$ tracer.

A.4.1 Ion chromatography measurement of Fe(II) and Fe(III)

The chromatographic separations are performed on an ICS-5000$^+$ instrument from ThermoFisher Scientific (Reinach, Switzerland, abbreviated to TFS) at a controlled temperature of 20 °C. The separation system consists mainly of a 50 × 2 mm CG5A pre-column and 250 × 2 mm CS5A separation column, followed by an post-column derivatisation (PCD) system. The derivatisation reagent is fed by means of a single-piston AXP Auxiliary Pump (TFS). The PCD reagent is kept under a helium atmosphere to minimise oxidation of 4-(2-pyridylazo)resorcinol (PAR). To avoid pulsations as much as possible, a 0.003" PEEK restrictor capillary with back pressure of approx. 1000 psi is interposed between the pump and the Mixing-T piece. Between the Mixing-T and the UV-VIS detector is a 375 µl "knitted reaction coil" in which the reaction of the analytes to the detectable colour complex takes place. The samples are injected from an AS-AP autosampler via a 10 µl sample loop. Detection is performed using a VWD-3100 detector at a wavelength of 530 nm. For a standard separation, the flow of the eluent is 0.30 ml/min and the flow of the NSD system is 0.15 ml/min.

The separation system is made oxygen free by flushing with 0.1 M Na_2SO_3 for 2 hours before switching to the eluent. The eluent MetPac PDCA (P/N046088) is prepared from a pre-prepared solution available from TFS. The mixture is degassed for 15-30 min and then purged with helium for another 5 min. The PCD reagent from TFS is also purchased ready-made (so-called 'diluent'), only the PAR salt is added and mixed well by ultrasonic bath to allow a complete dissolution of this compound. The concentration of PAR is 0.56 mM for analyte concentrations > 10 µM and 0.28 mM for analyte concentrations < 10 µM. Solutions of PAR are sensitive to oxidation and, according to the manufacturer, have a typical lifetime of 10 days at most. For this reason, it is recommended that PAR solutions are always prepared fresh and stored in an inert gas atmosphere.

Eluent composition, pH calculated is 4.2:

- 7 mM pyridine-2,6-dicarboxylic acid (PDCA)
- 5.6 mM K_2SO_4
- 74 mM formic acid
- 66 mM KOH

Diluent composition:

- 1 M dimethylaminoethanol
- 0.5 M NH_4OH
- 0.3 M Na_2CO_3

Calibration solutions were prepared from $Fe(II)SO_4 \cdot 7H_2O$ dissolved in 1 mM HNO_3. These solutions and the reagents used for preparation were stored several days in the glove box in order to maintain the target concentrations of ferrous iron. Ferric iron calibration solutions were prepared from $Fe(III)Cl_3$ in 1 mM HNO_3. Injection of pure $Fe(II)SO_4$ solutions produced a peak

of Fe(III) which exhibited ~ 6% of the peak signal of Fe(II). It was unequivocally demonstrated (independent colorimetric measurements of the samples by the phenanthroline method) that this amount of Fe(III) was not an impurity of $Fe(II)SO_4 \cdot 7H_2O$. It is noteworthy that this ratio of Fe(II) to Fe(III) in the chromatograms was found irrespective of the injected concentration of Fe(II). For this reason, all measurements in which Fe(II) and Fe(III) were quantified, the peak results were accordingly corrected by an appropriate correction function. It was further tested by repeat measurements that the ratio of Fe(II) to Fe(III) in the samples was not altered during the delay time of the samples in the autosampler. These repeat measurements also revealed a slight instability of the peak signals over the entire duration of the measurements. These changes were attributed to chemical changes occurring in the PCD reagent and were also corrected using appropriate verification standards.

Note that quantitative analysis of Fe(II) and Fe(III) can also be performed with spectrophotometric methods (such as the phenanthroline or the ferrozine methods, just to mention a few), which may also include the risk of erroneous results, but may be simpler to handle. The reason for application of the ion chromatography method in the present work lies mainly in the application of the method for ^{55}Fe containing samples in which the concentration of stable isotope Fe(II) is below the background of spectrophotometric methods. The ion chromatography can be applied for such samples in a semi-preparative way, leaving out the detection system, but collecting samples at elution times characteristic for the elution of Fe(II) and Fe(III). The activity in those fractions was measured off-line using β-counting. This allows for a quantification of the Fe(II) to Fe(III) ratio in tracered solutions from diffusion experiments or from acidic solutions used to desorb Fe from illite samples.

A.4.2 Diffusion measurements of $^{55}Fe(II)$ tracer (series 19001.FER)

The in-diffusion experiments followed by tracer profile analysis were carried out in analogy to those of ^{54}Mn described in section 3. Quantification of the activity of ^{55}Fe was performed by liquid scintillation counting. This method was not only applied to homogeneous solutions, but also to suspensions of illite in dilute acids as obtained after profiling of the clay for the measurement of the tracer profiles. Counting efficiency was only moderately affected by the presence of illite particles provided that the amount of illite in such samples did not substantially exceed a critical mass of ~ 5 mg. Calibration samples containing representative amounts of illite were used for the calculation of the activities in the profile samples present as disperse slurries.

Fig. A-1 shows the raw data of the experiments carried out at ionic strength of 0.1 M and pH values between 4 and 7. The experiments were carried out as duplicates, denoted to as A and B. Fit curves were simply obtained by fitting by eye using the assumption of linear sorption. The initial concentration of stable isotope Fe(II) in the reservoir solutions was 1 µM. This was obviously too low to prevent oxidation to Fe(III). Analysis of the tracer reservoir solutions at the end of the in-diffusion phase revealed that the $^{55}Fe(II)$ tracer was oxidised to $^{55}Fe(III)$ in almost all cases. The result of this oxidation is reflected in a rather stochastic behaviour of the reservoir concentration depletion curves which are not reproducible in all cases for the replicate experiments (cf. compare the results of experiments 4A and 4B). Further the mass balance between the tracer depletion in the reservoir and the recovery from the clay profiles was getting worse with increasing pH. In fact, only a very low amount of tracer could be recovered in the profiles from the samples at pH 7 and 8. For these reasons it was abstained to perform a quantitative parameter analysis from these results. Only a few cases were selected in order to get a rough idea of possible parameter values. The results are shown in Tab. A-3. Their credibility is, however, not outside of all doubt.

Tab. A-3: Summary of experimental conditions and the best-fit parameter values as obtained from single-species diffusion simulations in Comsol Multiphysics® for the experimental series 19001.FER

Exp	ρ_{bd} [kg m^{-3}]	**pH** [a]	$D_{e,c}$ [m^2 s^{-1}]	R_d [m^3 kg^{-1}]	$D_{e,f}$ [m^2 s^{-1}]
4A	1'700	4.0	5×10^{-11}	0.4	3.4×10^{-10}
5A	1'710	5.0	5×10^{-11}	1	3.4×10^{-10}
6A	1'707	6.0	1×10^{-10}	30	3.4×10^{-10}
6B	1'705	6.0	5×10^{-11}	30	3.4×10^{-10}

[a] Measured in the initial solutions and at the end of in-diffusion.

The large values for R_d obtained at pH 6 are another indication that oxidation of ferrous to ferric iron has occurred.

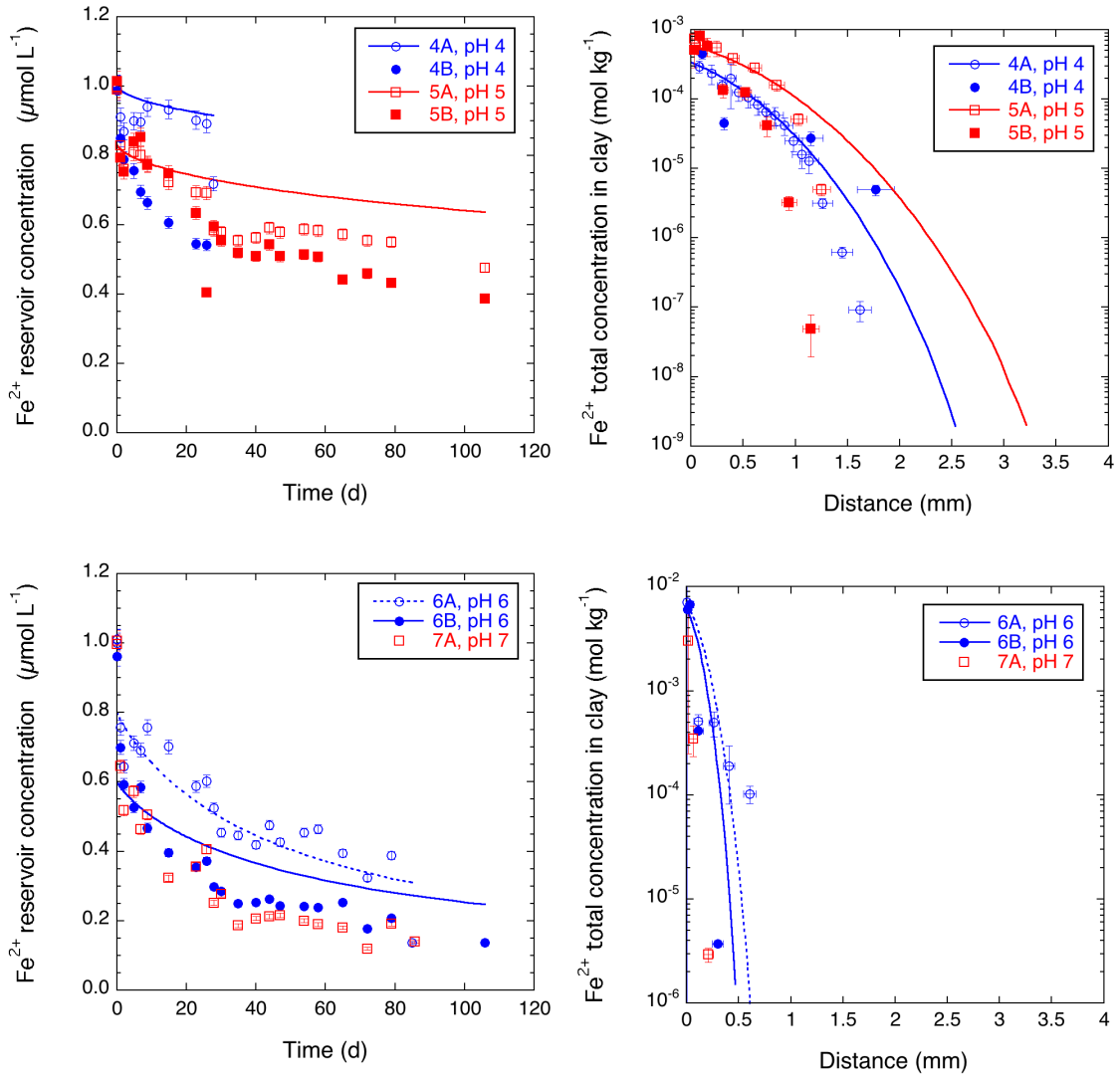

Fig. A-1: Evolution of the upstream reservoir solution concentration of Fe^{2+} (left-hand plots) and the total Fe^{2+} concentration (per dry clay) in the clay segments (right-hand plots) in the experimental series 19001.TON at ionic strength of 0.1 M; pH values as speciefied in the legend

Fit curves were produced by fit-by-eye for selected cases (cf. the legend).

A.4.3 Diffusion measurements of $^{55}Fe(II)$ tracer (series 19004.FER)

These experiments were carried out at two different ionic strengths in the same way as those of the 19001.FER series, however using a background concentration of 0.1 mM Fe(II) and at pH = 6, only. The results are shown in Fig. A-2. The model curves were obtained from fitting by-eye using again the assumption of linear sorption, which is not fulfilled at the conditions of elevated concentrations of stable Fe(II). The non-linear sorption behaviour is obvious from the signature of the tracer profiles which exhibit a strong decrease near the tracer front. This behaviour is not captured in the shape of the modelling curves. The fit parameters shown in Tab. A-4 are thus applicable only for the Fe(II) solution concentrations in the early phase of in-diffusion. In contrast to the parameter values derived from experimental series 19001.FER, the present parameter values appear much more reliable.

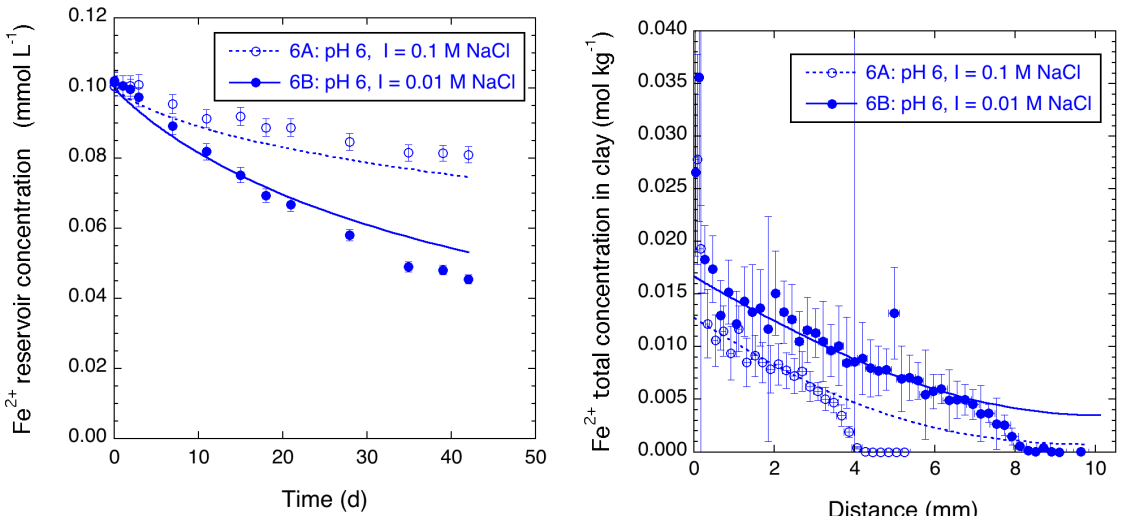

Fig. A-2: Evolution of the upstream reservoir solution concentration of Fe^{2+} (left-hand plots) and total Fe^{2+} concentration (per dry clay) in the clay segments (right-hand plots) in the experimental series 19001.TON at ionic strength of 0.1 M; pH values as speciefied in the legend

Fit curves were produced by fit-by-eye for selected cases (cf. the legend).

They exhibit the typical behaviour of transition metals undergoing EDL diffusion: Both $D_{e,c}$ and R_d values increase with decreasing salinity of the liquid phase.

The quantitative parameter dependencies involved may be assessed from thermodynamic equilibrium modelling as already applied in the case of the diffusion of Mn^{2+} (cf. section 3.3.3). This requires that an appropriate sorption model for the uptake of Fe^{2+} is available. For the present purpose for a very approximate and tentative evaluation, the sorption data of Zn^{2+} were used to mimic the sorption behaviour of Fe^{2+}. Fig. A-3 shows the sorption isotherms calculated for the conditions of the diffusion experiments. It is obvious that the auxiliary sites are not contributing substantially to overall sorption and that these can be ignored for the diffusion simulations.

Tab. A-4: Summary of experimental conditions and the best-fit parameter values as obtained from single-species diffusion simulations in Comsol Multiphysics® for the experimental series 19004.FER

Exp.	ρ_{bd} [kg m^{-3}]	pH [a]	Ionic strength [M]	$D_{e,c}$ [m^2 s^{-1}]	R_d [m^3 kg^{-1}]	$D_{e,f}$ [m^2 s^{-1}]
6A	1'702	6.0	0.1	1×10^{-9}	0.2	3.4×10^{-10}
6B	1'703	6.0	0.01	5×10^{-9}	0.5	3.4×10^{-10}

[a] Measured in the initial solutions and at the end of in-diffusion.

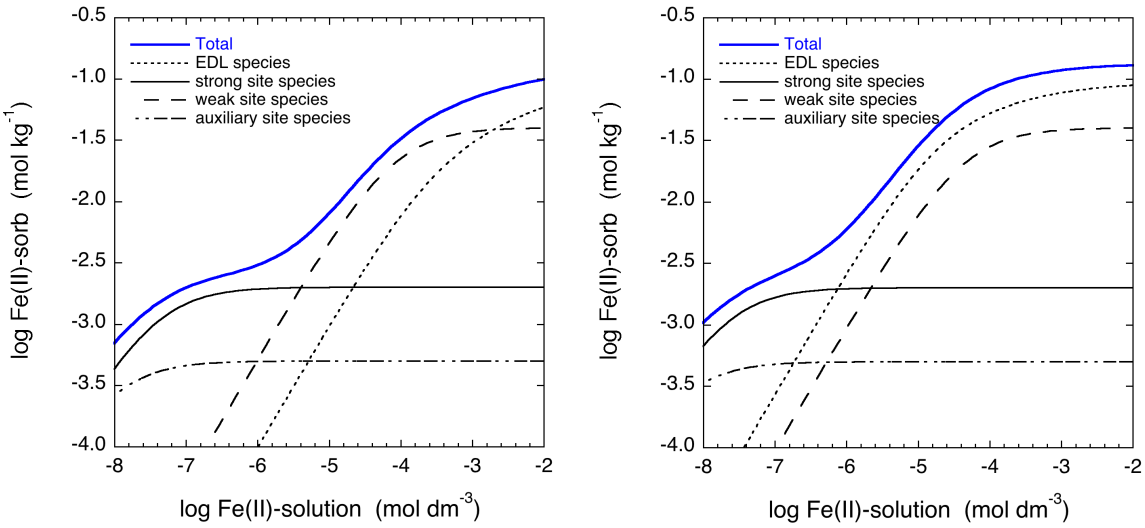

Fig. A-3: Sorption isotherm of Fe(II) on IdP for pH 6 and ionic strengths of 0.01 M (left-hand plot) and 0.1 M (right-hand plot) using the thermodynamic data for Zn (Montoya et al. 2018) and adding auxiliary sites with the same binding properties as those for the sorption of Mn^{2+} (cf. Section 3)

Fig. A-4 shows the blind predictions for the diffusion data measured at an ionic strength of 0.1 M NaCl in experiment 6A and Fig. A-5 the respective plot for experiment 6B (0.01 M NaCl). The underlying thermodynamic data used for these calculations are given in Tab. A-5. Note that diffusion calculations using the existing models in Comsol are not purposeful because the concentration ranges of Fe(II) involved across the duration of in-diffusion cover non-linear ranges of sorption in both cases. For this reason it may be expected that $D_{e,c}$ values may not be treated as constants. In analogy to the diffusion calculations shown for the diffusion of Mn^{2+} in Section 3, the Phreeqc simulations use the simplifying assumption of a 1-dimensional diffusion geometry which is not fully applicable with respect to the construction of the membrane-confined diffusion cell. As previously outlined, the errors introduced by this simplification are rather insignificant. In view of these restrictions and the fact that the simulation curves shown in Fig. A-4 and Fig. A-5 are near-blind predictions (a q_η of 0.4 was assumed and d_{DL} was chosen to be 0.7 for better numerical performance of the code), the agreement between the data and the simulation is

satisfying. In such respects, it can be stated that the 2SPNE-SC/EDL model may well be applicable to Fe^{2+}. No further attempts were taken to further optimise the parametrisation of the current model.

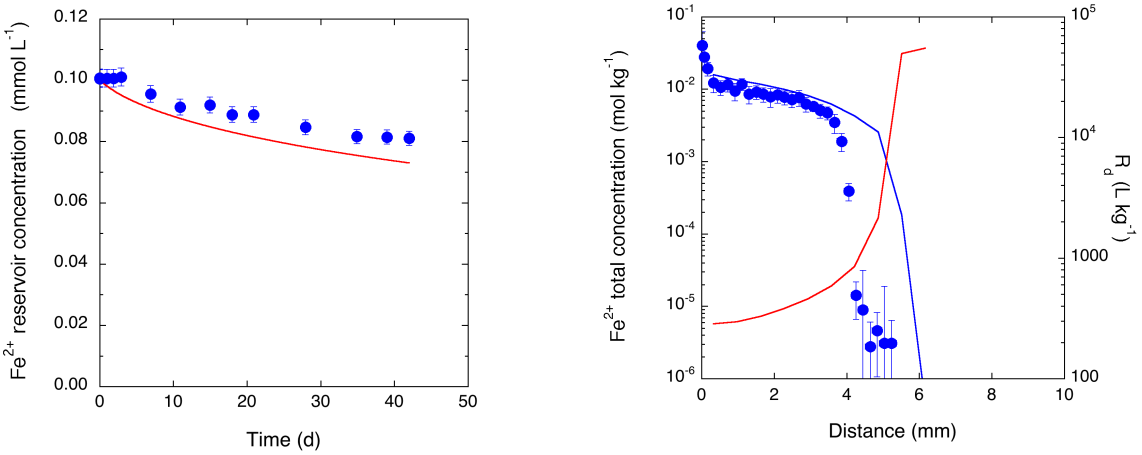

Fig. A-4: Evolution of upstream reservoir solution concentration of Fe^{2+} (left-hand plot) and total Fe^{2+} concentration (blue, per dry clay) and R_d (red) in the clay segments (right-hand plot) in experiment 6A (ionic strength 0.1 M NaCl)

Best-fit curves obtained from a Phreeqc simulation involving thermodynamic data used for isotherm calculations in Fig. A-3.

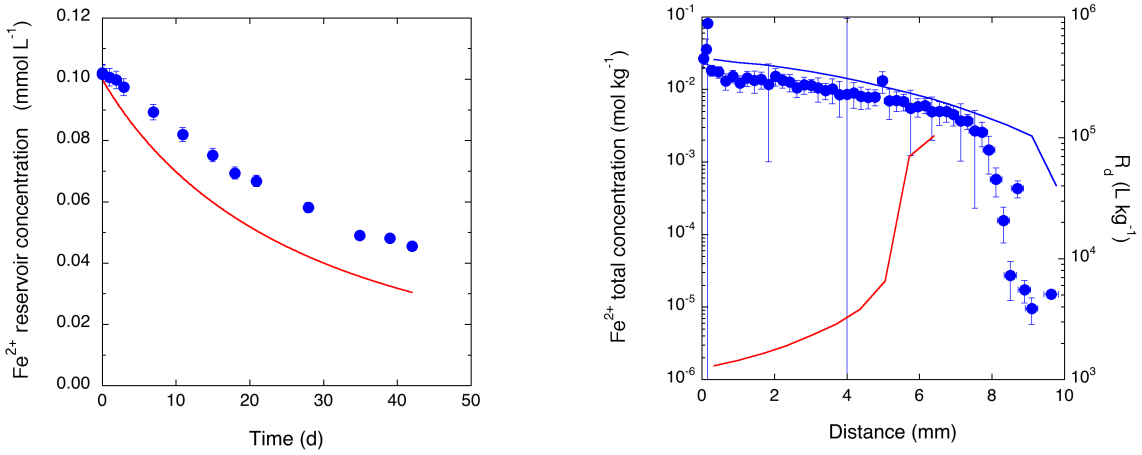

Fig. A-5: Evolution of upstream reservoir solution concentration of Fe^{2+} (left-hand plot) and total Fe^{2+} concentration (blue, per dry clay) and R_d (red) in the clay segments (right-hand plot) in experiment 6A (ionic strength 0.01 M NaCl)

Best-fit curves obtained from a Phreeqc simulation involving thermodynamic data used for isotherm calculations in Fig. A-3.

Tab. A-5: Thermodynamic data proposed for modelling the in-diffusion data of Fe(II) in illite compacted to bulk-dry density of 1'700 kg m^{-3}

The data for Fe(II) are used in analogy to the sorption of Zn^{2+} (Montoya et al. 2018). All other constants are literature values (Appelo & Wersin, 2007, Bradbury & Baeyens 2009a, Glaus et al. 2015a, Marques Fernandes et al. 2015, Montoya et al. 2018).

Site types	**Strong sites**	**Weak sites (#1)**	**Auxiliary sites**	**Stern layer sites**
Site capacities (mol kg^{-1})	2×10^{-3}	4×10^{-2}	5×10^{-4}	1.9×10^{-1}
Formation constants [a] *for the addition of*	${}^{s}\beta$	${}^{w\#1}\beta$	${}^{wx}\beta$	${}^{Su}K$
H^+	6.2 / 4.0 [b]	6.2 / 4.0 [b]	4.2 / (3.5) [b]	-0.8
Na^+	-	-	-	-0.7
K^+	-	-	-	0.654
Mg^{2+}	-	-	-	0.107
Ca^{2+}	-	-	-	0.104
Al^{3+}	-	-	-	0.3
Co^{2+}	0.9 / -7.0 / -16.5 [c]	-1.8 [d]	2.3 [d]	0.7
Fe^{2+}	2.1 / -6.4 / -15.0 [c]	-1.4 / -7.7 [d]	4.3 / -7.7 [d]	0.7

[a] ^{10}log values

[b] Stepwise protonation of strong and weak sites ($\equiv SO^-$), viz. $\equiv SO^- + H^+ = \equiv SOH$ and $\equiv SOH + H^+ = \equiv SOH_2^+$

[c] $\equiv S^SOH + Me^{2+} = \equiv S^SOMe(OH)_{j-1}^{2-j} + jH^+$; j = 1,2,3, where $\equiv S^SOH$ is the mono-protonated strong surface site and Me a divalent metal cation.

[d] $\equiv S^WOH + Me^{2+} = \equiv S^WOMe(OH)_{j-1}^{2-j} + jH^+$; j = 1,2, where $\equiv S^WOH$ is the mono-protonated weak surface sites (w#1 and wx)

A.4.4 Competition experiments with ^{57}Co tracer in mixed Na^+/Fe^{2+}-IdP

These experiments were carried out in analogy to those described in section 4.4, in which the competitive effect of Mn^{2+} on the diffusion of Co^{2+} tracer was investigated at an ionic strength of 0.1 M and in a pH range between 4 and 7. For the present experiments, a mixed Na^+/Fe^{2+} cation loaded IdP was used, with amounts of Fe^{2+} saturation either both strong and weak sorption sites ("H-series") or only the strong sites ("L-series"). Owing to the compaction of the IdP samples in the N_2-glove box, and the lack of an appropriate balance for exactly weighting the amounts of clay, the resulting bulk-dry densities were somewhat lower than usual. The bulk-dry densities were determined post-mortem by weighing the samples holders containing the clay samples.

Furthermore, cation exchange experiments carried out in which targeted amounts of Fe^{2+} and Co^{2+} were added to suspensions of systems containing Na-IdP equilibrated with NaCl and $^{22}Na^+$ tracer. The resulting cation exchange selectivity (K_c) values ranged between ~ 5 and 12 for both Co^{2+} and Fe^{2+}. These selectivities are in fair agreement with the Stern layer surface complex constants given in Tab. A-5.

The experimental conditions of the diffusion experiments and the results of the single-species modelling in Comsol Multiphysics are given in Tab. A-6. Simulations of the results given in Tab. A-6 are performed by the 2SPNE-SC/EDL model using the thermodynamic data given in Tab. A-5.

Tab. A-6: Summary of best-fit parameter values for the diffusion of Co^{2+} in mixed Na/Fe(II)-IdP obtained from single-species diffusion simulations by Comsol Multi-physics®

All experiments were carried out using 0.1 M $NaClO_4$ background electrolyte, 2 mM of buffer.

Label	ρ_{bd} [kg m^{-3}]	pH	Fe(II) [a] [M]	Fe(II) [b] [M]	Fe(II) [c] [M]	$D_{e,c}$ [m^2 s^{-1}]	R_d [dm^3 kg^{-1}]	$D_{e,f}$ [m^2 s^{-1}]
L4	1'522	4.0	2.5×10^{-5}	1.5×10^{-5}	3.8×10^{-5}	$(5.4 \pm 0.3) \times 10^{-10}$	$(1.4 \pm 0.07) \times 10^{2}$	$(2.8 \pm 0.5) \times 10^{-10}$
L5	1'544	5.0	< det.lim.	< det.lim.	2.2×10^{-6}	$(7.0 \pm 1.0) \times 10^{-10}$	$(4.5 \pm 0.56) \times 10^{2}$	$(2.8 \pm 0.5) \times 10^{-10}$
L6	1'503	6.0	< det.lim.	< det.lim.	3.1×10^{-7}	$(8.5 \pm 2.4) \times 10^{-10}$	$(2.3 \pm 0.60) \times 10^{3}$	$(2.8 \pm 0.5) \times 10^{-10}$
L7	1'606	7.0	< det.lim.	< det.lim.	1.4×10^{-7}	$(1.3 \pm 0.59) \times 10^{-9}$	$(6.8 \pm 3.0) \times 10^{3}$	$(2.6 \pm 0.5) \times 10^{-10}$
H4	1'601	4.0	2.1×10^{-1}	1.8×10^{-1}	1.9×10^{-1}	$(8.6 \pm 0.5) \times 10^{-11}$	$(5.4 \pm 1.4) \times 10^{-1}$	$(2.8 \pm 0.5) \times 10^{-10}$
H5	1'545	5.0	7.0×10^{-3}	6.2×10^{-3}	6.1×10^{-3}	$(3.6 \pm 0.06) \times 10^{-10}$	$(6.0 \pm 0.02) \times 10^{0}$	$(2.8 \pm 0.5) \times 10^{-10}$
H6	1'545	6.0	7.6×10^{-4}	7.6×10^{-4}	5.8×10^{-4}	$(8.8 \pm 0.39) \times 10^{-10}$	$(2.8 \pm 0.04) \times 10^{1}$	$(2.8 \pm 0.5) \times 10^{-10}$
H7	1'565	7.0	3.0×10^{-5}	7.0×10^{-5}	6.5×10^{-5}	$(1.0 \pm 0.11) \times 10^{-9}$	$(1.7 \pm 0.14) \times 10^{2}$	$(2.8 \pm 0.5) \times 10^{-10}$

[a] Measured after saturation of the compacted illite samples with Fe(II)-containing electrolyte
[b] Measured after diffusion
[c] Value expected according to sorption modelling

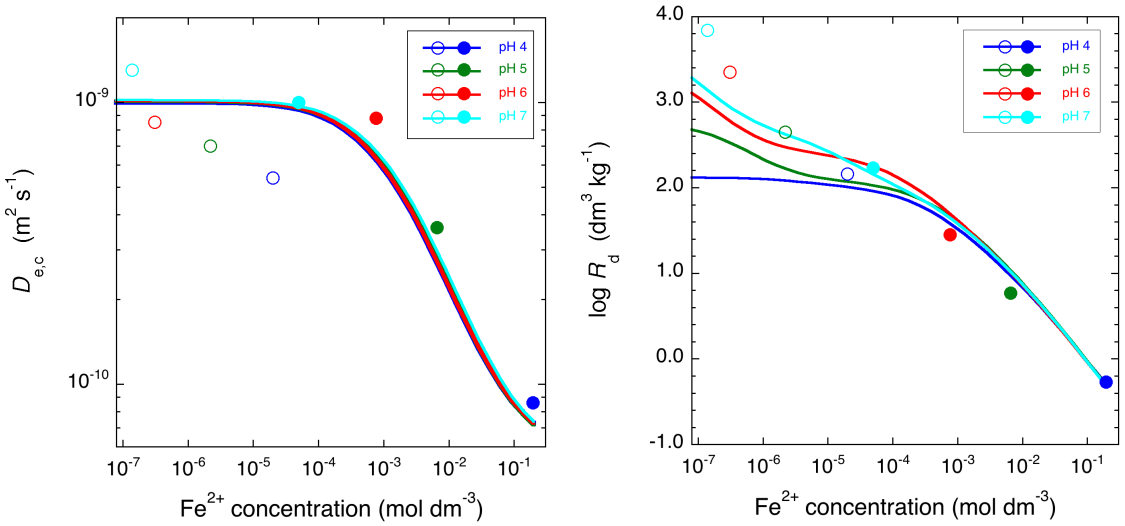

Fig. A-6: Dependence of $D_{e,c}$ (left-hand plot) and R_d (right-hand plot) of $^{57}Co^{2+}$ tracer on the concentration of Fe^{2+} in the contacting electrolyte

Empty symbols represent the data for the L-series and full symbols those of the H-series.